# DEVELOPMENT OF SUPERCONDUCTING CONTACTS TO GE/SIGE QUANTUM WELLS

by

**Hao Li**

**A Dissertation**

*Submitted to the Faculty of Purdue University*

*In Partial Fulfillment of the Requirements for the degree of*

**Doctor of Philosophy**

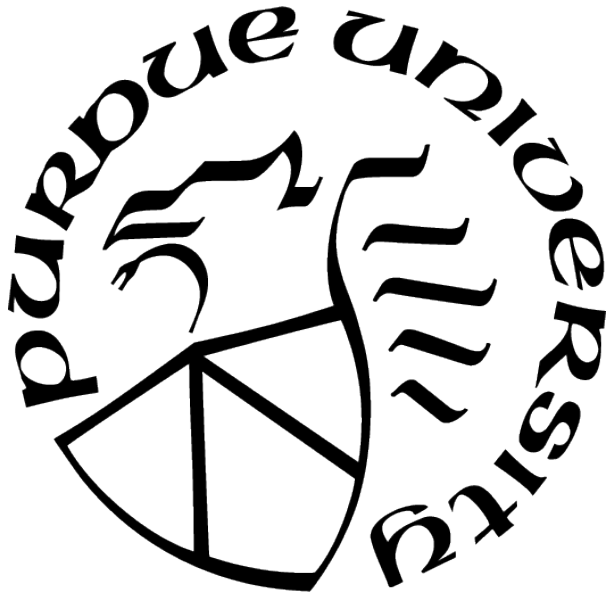


Department of Physics and Astronomy

West Lafayette, Indiana

May 2026

# THE PURDUE UNIVERSITY GRADUATE SCHOOL
# STATEMENT OF COMMITTEE APPROVAL

**Dr. Leonid P. Rokhinson, Chair**

Dept. of Physics and Astronomy

**Dr. Gábor A. Csáthy**

Dept. of Physics and Astronomy

**Dr. Chen-Lung Hung**

Dept. of Physics and Astronomy

**Dr. Jukka I. Vayrynen**

Dept. of Physics and Astronomy

**Approved by:**

Dr. Gábor A. Csáthy

*To my beloved family.*

# ACKNOWLEDGMENTS

First and foremost, I would like to extend my sincere thanks to my advisor, Professor Rokhinson. Your guidance, expertise, and unwavering support have been invaluable throughout this research journey. Your dedication to mentoring and your commitment to excellence have shaped me into the researcher I am today.

To my dedicated labmates, Ananthesh Sanderesh, Mingi Kim, Nemanja Ninkovic, Iakov Kogan, Aidan Maxwell Jacobsen, Andress Allcca, and Karim Dakroury, I am grateful for the collaborative environment we shared. Your unwavering support, intellectual discussions, and willingness to lend a helping hand have significantly enriched my research experience. I am indebted to the valuable insights, constructive feedback, and camaraderie we developed over the years.

I would like to acknowledge the contributions of the postdoctoral researchers in our lab, Jian Liao, Tai-Lung Wu, and Maxim Savchenko. Your expertise, technical assistance, and insightful discussions have been crucial to the progress of my research. Your mentorship and willingness to share your knowledge have been immensely valuable.

My heartfelt thanks go to the members of my thesis committee for their invaluable feedback and guidance. Your expertise and constructive criticism have significantly improved the quality of this work.

I extend my heartfelt appreciation to the entire BNC and cleanroom staff for their unwavering support and assistance throughout my research. Their commitment to maintaining state-of-the-art facilities has been indispensable in achieving the outcomes of my thesis.

No words can adequately express my gratitude to my parents. Their unwavering love, endless encouragement, and belief in my abilities have been the foundation upon which my academic pursuits were built. I am eternally grateful for their sacrifices, patience, and unwavering support during the challenging moments of this journey.

To all those mentioned above and anyone else who has contributed in any way, however small, I offer my heartfelt appreciation. Your support, guidance, and collaboration have played a significant role in the successful completion of this thesis. Thank you for being an integral part of this journey.

This material is based upon work supported by the U.S. National Science Foundation under Award No. 2005092. Any opinions, findings, and conclusions or recommendations expressed in this material are those of the author and do not necessarily reflect the views of the National Science Foundation.

The author also acknowledges the Engineering and Physical Sciences Research Council (EPSRC) for support under project EP/X039757 to Prof. Maksym Myronov at the University of Warwick, which funded the growth of the germanium heterostructures used in this work. This work was performed, in part, at the Center for Integrated Nanotechnologies (CINT), an Office of Science User Facility operated for the U.S. Department of Energy (DOE) Office of Science. Sandia National Laboratories is a multimission laboratory managed and operated by National Technology and Engineering Solutions of Sandia, LLC, a wholly owned subsidiary of Honeywell International, Inc., for the U.S. DOE's National Nuclear Security Administration under contract DE-NA-0003525. The views expressed in the article do not necessarily represent the views of the U.S. DOE or the United States Government.

The author specially thanks Dr. Michael Lilly for his contribution to the Ir deposition under the CINT User Proposal No. 2023BU0040 awarded to Prof. Leonid Rokhinson.

Finally, portions of this thesis have been adapted and expanded from previously published work by the author. Specifically, Chapter 3 is based on the author's work in [1], which is licensed under CC-BY 4.0.

# TABLE OF CONTENTS

# LIST OF TABLES

# LIST OF FIGURES

# ABSTRACT

The CMOS-compatible fabrication of strained-Ge superconducting electronics offers a scalable platform for superconducting quantum processors and the study of non-Abelian excitations. Specifically, the integration of superconducting contacts with one-dimensional helical channels around the quantum Hall ferromagnetic transition in Ge/SiGe quantum wells provides a candidate architecture for the realization of Majorana fermions. This requires the development of superconducting contacts that maintain high out-of-plane critical magnetic fields while remaining within the strict thermal budget of strained Ge heterostructures.

This thesis presents a comparative study of Pt, Pd, Rh, and Ir germanide films, focusing on the characterization of Ir-based films formed via solid-phase epitaxy. IrGe and IrSiGe films, fabricated under optimized conditions, exhibit superconducting critical temperatures of 3.4 K and 2.6 K, respectively—a four-fold increase in superconducting gap size compared to PtSiGe. These films preserve robust superconductivity in out-of-plane magnetic fields exceeding 1 T. High-resolution scanning transmission electron microscopy and energy-dispersive x-ray spectroscopy confirm the formation of polycrystalline IrGe with a sharp, high-quality interface at the Ge(001) surface.

Finally, we evaluate the performance of these contacts in Ge-based mesoscopic structures. We observe signatures of induced superconductivity in IrSiGe/Ge quantum well heterostructures via three-terminal contact resistance measurements under DC bias. The demonstration of this CMOS-compatible solid-phase epitaxy process establishes a viable pathway for advanced superconducting electronics, including high-performance Ge-based Josephson field-effect transistors.

# 1. INTRODUCTION

## 1.1 Background

Since the prediction of Majorana fermions in topological superconductors (TSCs) [2], the experimental realization of topological superconductivity has attracted significant interest. A primary motivation is that Majorana fermions provide a platform for inherently fault-tolerant quantum computation via topological protection [3]–[6]. However, external noise remains the greatest challenge toward the realization of the full potential of superconducting quantum computers [7], [8].

Numerous physical systems have been predicted to host Majorana fermions, including many hybrid superconductor–semiconductor (S–Sm) systems, e.g., one-dimensional (1D) semiconducting nanowires proximitized by conventional $s$-wave superconductors [9]–[11], proximitized topological insulators (TIs) [12]–[15], and proximitized two-dimensional (2D) heterostructures [16]–[18], among which 2D hole gas (2DHG) in Ge is a leading candidate [19]. The development of superconductor–semiconductor hybrid technology based on group IV semiconductors [20]–[30] is facilitated by advances in the growth of compressively strained Ge on Si (cs-GoS) heterostructures via relaxed SiGe buffer, where the mobility of two-dimensional hole gases in Ge quantum wells (QWs) can exceed $10^6\,\mathrm{cm}^2/(\mathrm{V}\cdot\mathrm{s})$ [31]–[35]. Ge possesses several advantageous physical properties, including strong spin-orbit coupling (SOC), low hyperfine interaction, gate-tunable $g$-factor due to inter-carrier interactions [36], and high mobility [37]. Combined with its compatibility with mature CMOS technology [38], these attributes make Ge a promising material platform for fault-tolerant quantum computing.

Non-Abelian excitations have also been predicted in different systems, where $s$-wave superconductors are coupled to 1D helical edge channels [39]–[43]. The discovery of quantum Hall ferromagnetic (QHFM) transition in Ge/SiGe 2DHG at low density [36] provides a route towards realizing Majorana fermions by coupling superconductors to the ends of a 1D helical channel, created at the edge of two quantum Hall (QH) states with opposite spins. Highly transparent superconducting contacts to these helical channels that can remain superconducting at high out-of-plane magnetic fields are therefore critical for this realization. Aluminum forms low-resistance contacts with strained Ge due to Fermi-level pinning near

the valence band edge [20], [21]. Superconductivity can be induced in Ge QWs via the proximity effect, either in direct Al/Ge contacts [22]–[24], [29] or Al separated from Ge by a thin, semitransparent SiGe barrier [26], [27]. However, because the diffusion of Al into (Si)Ge is not self-limiting, the transparency of annealed Al contacts is a strong function of post-deposition processing. The sensitivity of Al contacts to thermal treatment, their low superconducting critical temperature ($T_c < 1.5\,\mathrm{K}$), and their limited out-of-plane critical field ($B_{c,\perp} \sim 10\,\mathrm{mT}$) have stimulated the development of alternative contacts. Similarly, the critical fields of the superconducting states induced in Ge/SiGe quantum wells (QWs) by PtSiGe [25], [28], [30], [44] are below the field requirement to induce QHFM transition in Ge QWs. Although Majorana fermions are the simplest representatives of non-Abelian bound states that can be used for topological quantum computation, braiding of $\mathbb{Z}_2$ Majorana fermions cannot generate all the gate operations needed for universal topological quantum computing [6], [45], [46]. This limitation motivates the pursuit of more complex anyonic states associated with the $\mathbb{Z}_n$ permutation group.

This thesis focuses on the development of transparent superconducting contacts to Ge QWs that exhibit high critical magnetic fields. Chapter 1 introduces some fundamental concepts of superconductivity and the QH effect, alongside the physical properties of Ge QWs, the physics of hybrid superconductor–semiconductor (S–Sm) systems, and induction of superconducting correlations in QH edge states. Chapter 2 presents the characterizations of high-mobility 2DHG in strained Ge QWs, as well as the nanofabrication techniques employed in this study. Chapter 3 details the systematic characterization of superconducting germanide and germanosilicide films of Pd, Pt, Rh, and Ir formed by solid-phase epitaxy. Chapter 4 summarizes some preliminary results on the development of superconducting contacts to Ge QWs. Chapter 5 addresses the remaining challenges and discusses future perspectives toward fabricating high-$B_c$ superconductong contacts and the realization of non-Abelian excitations in Ge/SiGe systems.

## 1.2 Concepts

### 1.2.1 Superconductivity

Superconductivity—the vanishing electrical resistance—was first discovered in mercury at 4.2 K by H. K. Onnes in 1911 [47], shortly after his successful liquefaction of helium in 1908. While numerous other superconductors were discovered in the following decades, a robust theoretical understanding of superconductivity remained elusive until the phenomenological approach proposed by F. London and H. London [48], which successfully describes the Meissner effect [49]—complete expulsion of magnetic field below superconducting critical temperature $T_c$. This phenomenon is often captured by the London equation:

$$\nabla^2 \mathbf{B} = \frac{1}{\lambda^2}\mathbf{B} = \frac{\mu_0 n e^2}{m_e}\mathbf{B}, \tag{1.1}$$

where $\mathbf{B}$ is the magnetic field, $\lambda$ is the London penetration depth, $\mu_0$ is the vacuum magnetic permeability, $n$ is the superconducting electron density, and e and $m_e$ are the charge and mass of the electron, respectively. This equation predicts that an external magnetic field decays exponentially as it penetrates the surface of a superconductor. The other two constitutive equations by London:

$$\begin{aligned} \frac{\partial \mathbf{j}}{\partial t} &= \frac{n e^2}{m_e}\mathbf{E}, \\ \nabla \times \mathbf{j} &= -\frac{n e^2}{m_e}\mathbf{B} \end{aligned} \tag{1.2}$$

further demonstrate that the expulsion of the magnetic field arises from the screening currents at the surface. The Meissner effect implies that superconductivity cannot be simply understood as "perfect conductivity" and serves as a defining characteristic of the superconducting state.

In 1950, V. L. Ginzburg and L. D. Landau established an alternative phenomenological theory of superconductivity based on Landau's previous theory of second-order phase transition

[50]. By expressing the free energy of a superconductor in terms of a complex order parameter, $\psi(\mathbf{r}) = |\psi(\mathbf{r})|e^{i\phi(\mathbf{r})}$, one arrives at the Ginzburg-Landau equations:

$$\begin{aligned} \frac{1}{2m^*}\left(-i\hbar\nabla - \frac{e^*}{c}\mathbf{A}\right) + \alpha\psi + \beta|\psi|^2\psi = 0, \\ \nabla \times \mathbf{B} = \frac{4\pi}{c}\mathbf{J}, \\ \mathbf{J} = \frac{e^*}{m^*}\,\mathrm{Re}\left[\psi^*\left(-i\hbar\nabla - \frac{e^*}{c}\mathbf{A}\right)\psi\right]. \end{aligned} \tag{1.3}$$

Here $\mathbf{J}$ is the superconducting current density, $\alpha(T) = \alpha_0(T - T_c)$ (when $T < T_c$), and $\beta$ are phenomenological parameters, $m^*$ is the effective mass, and $e^*$ is the effective charge (usually $2e$). $n_s = |\psi|^2$ measures the local density of superconducting electrons. Thus, in a homogeneous superconductor with $\mathbf{J} = 0$, we have:

$$n_s = |\psi|^2 = -\frac{\alpha_0(T - T_c)}{\beta}. \tag{1.4}$$

In this interpretation, $n_s = |\psi|^2$ indicates the density of electrons that have condensed into superfluid.

The penetration depth $\lambda$ expressed in Ginzburg-Landau theory is:

$$\lambda = \sqrt{\frac{m^*}{\mu_0 e^{*2}\psi_0^2}} = \sqrt{\frac{m^*\beta}{\mu_0 e^{*2}|\alpha|}}, \tag{1.5}$$

where $\psi_0$ is the equilibrium order parameter in zero external field. And a new characteristic length, coherence length:

$$\xi = \sqrt{\frac{\hbar^2}{4m^*|\alpha|}} \tag{1.6}$$

is predicted, describing the length scale where the small perturbation of $n_s$ recovers to equilibrium in exponential law. Superconductors can be sorted into two types according to the Ginzburg-Landau parameter $\kappa = \lambda/\xi$. Type-I are superconductors with $0 < \kappa < 1/\sqrt{2}$. For $\kappa > 1/\sqrt{2}$, type-II superconductors exhibit an intermediate phase of superconducting and normal mixture through magnetic vortices that penetrate through the material.

However, these theories could not explain the microscopic origin of superconductivity. In 1950, E. Maxwell [51] and C. A. Reynolds *et al.* [52] found that $T_c$ depends on the isotopic mass of the element, suggesting the role of phonon interaction in superconductivity. Combining the fact that single electrons cannot condense into a superfluid due to the Pauli exclusion principle, a mean field theory of superconductivity was proposed by J. Bardeen, L. N. Cooper and J. R. Schrieffer in 1957 [53], [54], which was later reinforced with the microscopic description by N. N. Bogoliubov [55] and L. P. Gor'kov [56].

The Bardeen-Cooper-Schrieffer (BCS) theory explains the superconducting current as a superfluid of pairs of electrons interacting through phonon interactions, called Cooper pairs. The lattice deformation of one electron produces an attractive potential for a following electron without feeling strong Coulomb repulsion from the first electron. According to BCS theory, any sufficiently small attractive potential can create an energy gap in the single-electron spectrum, which is the energy required to break a Cooper pair. BCS theory also expresses how the gap evolves with temperature, with the following relation to the critical temperature:

$$\Delta_{\mathrm{BCS}}(T=0) = 1.764 k_{\mathrm{B}} T\mathrm{c}, \tag{1.7}$$

which is true for weakly-coupled superconductors.

From BCS theory, superconductors can traditionally be classified by the relative angular momentum of Cooper pairs, as $s$-wave, $p$-wave, $d$-wave, $f$-wave, and so forth [57]. For conventional weakly-coupled $s$-wave superconductors, electrons with opposite spin $s$ and momentum $k$ near the Fermi level $\epsilon_{\mathrm{F}}$ form Cooper pairs with zero angular momentum. In these cases, the BCS coherence length can be expressed by:

$$\xi_{\mathrm{BCS}} = \frac{\hbar v_{\mathrm{F}}}{\pi \Delta}, \tag{1.8}$$

where $v_{\mathrm{F}}$ is the Fermi velocity and $\Delta$ is the superconducting energy gap. This value provides a measure of the size of Cooper pairs. Regarding high-$T_c$ superconductors [58], [59] that exceed the McMillan limit [60], conventional BCS theory is insufficient to explain their properties.

### 1.2.2 Hall Effect

When applying an out-of-plane magnetic field $\mathbf{B}$ and an in-plane electric field $\mathbf{E}$ to free carriers confined to a material in the $x$–$y$ plane, considering the friction that carriers experience during drifting, the equation of motion in the simplest Drude model is:

$$m^*\dot{\mathbf{v}}_\mathrm{d} = q(\mathbf{E} + \mathbf{v}_\mathrm{d} \times \mathbf{B}) - \frac{m^*\mathbf{v}_\mathrm{d}}{\langle\tau_m\rangle}, \tag{1.9}$$

where $m^*$ and $q$ are the effective mass and charge of the carrier, $\mathbf{v}_\mathrm{d}$ is its drift velocity, and $\langle\tau_m\rangle$ is the average momentum relaxation time to return to equilibrium.

In the static case, $\langle\dot{\mathbf{v}}_\mathrm{d}\rangle = 0$, we get $|\mathbf{v}_\mathrm{d}| = \mu|\mathbf{E}|$ at $\mathbf{B} = 0$, where the drift mobility $\mu$ is:

$$\mu = \left|\frac{q\langle\tau_m\rangle}{m^*}\right|, \tag{1.10}$$

so the current density $\mathbf{J} = nq\mathbf{v}_\mathrm{d} = \sigma\mathbf{E}$, where the (longitudinal) conductivity is obtained as

$$\sigma = ne\mu = \frac{ne^2\langle\tau_m\rangle}{m^*} = 1/\rho. \tag{1.11}$$

Here $n$ is the carrier density, and $\rho$ is the longitudinal resistivity. In a transverse magnetic field, from a solution of the Boltzmann equation in the relaxation time approximation, we get the Hall/transverse resistivity $\rho_{xy}$:

$$\rho_{xy} = \frac{E_y}{J_x} = R_\mathrm{H}B = \frac{r_\mathrm{H}B}{nq}, \tag{1.12}$$

where $R_\mathrm{H} = r_\mathrm{H}B/nq$ is called the Hall coefficient and the Hall factor $r_\mathrm{H} = \langle\tau_m^2\rangle/\langle\tau_m\rangle^2$ [61]. For a weak magnetic field, $r_\mathrm{H} \sim 1$–$2$ depends on the scattering mechanism. For a strong magnetic field ($(\mu_\mathrm{H}B)^2 \gg 1$), $r_\mathrm{H} \approx 1$. The carrier type and concentration can be determined by $r_\mathrm{H}/R_\mathrm{H}e$. The Hall mobility is defined as:

$$\mu_\mathrm{H} = \sigma\,|R_\mathrm{H}| = r_\mathrm{H}\mu = \frac{1}{\rho}\left|\frac{\mathrm{d}\rho_{xy}}{\mathrm{d}B}\right|, \tag{1.13}$$

which is measured in experiment rather than the drift mobility.

### 1.2.3 Integer Quantum Hall Effect

When a 2DEG/2DHG is subjected to a perpendicular magnetic field $B$, the Schrödinger equation, in the Landau gauge $\hat{\mathbf{A}} = (-B\hat{y}, 0, 0)$, $\phi = 0$, is given by [62]:

$$\left[\frac{1}{2m^*}(\hat{\mathbf{p}} - q\hat{\mathbf{A}})^2 + V(x,y,z)\right]\psi(x,y,z) = \varepsilon\psi(x,y,z). \tag{1.14}$$

For simplicity, we consider $V(x,y,z) = V_{xy}(x,y) + V_z(z)$ in a finite sample. Exploiting the symmetry, we use the ansatz: $\psi(x,y,z) = \varphi(x,y)Z(z)$, $\varepsilon = \varepsilon_{xy} + \varepsilon_z$.

Along the $z$-axis, within the device region, we have:

$$\left[-\frac{\hbar^2}{2m^*}\frac{\partial^2}{\partial z^2} + V_z(z)\right]Z(z) = \varepsilon_z Z(z). \tag{1.15}$$

The solution depends on the QW potential $V_z(z)$ but can normally be solved numerically.

For the rest of the equation,

$$\left[\frac{1}{2m^*}\left(-\mathrm{i}\hbar\frac{\partial}{\partial x} + qBy\right)^2 - \frac{\hbar^2}{2m^*}\frac{\partial^2}{\partial y^2} + V_{xy}(x,y)\right]\varphi(x,y) = \varepsilon_{xy}\varphi(x,y), \tag{1.16}$$

still for simplicity, we start with $V_{xy}(x,y) = V_x(x) + V_y(y)$. Since $[\hat{p}_x, \hat{H}] = 0$, $\varphi(x,y)$ are eigenstates of $\hat{p}_x$, we use ansatz $\varphi(x,y) = X(x)Y(y) = \mathrm{e}^{\mathrm{i}k_x x}Y(y)$, and replace $\hat{p}_x$ with the eigenvalue $\hbar k_x$. This yields:

$$\left[\frac{1}{2m^*}(\hbar k_x + qBy)^2 - \frac{\hbar^2}{2m^*}\frac{\partial^2}{\partial y^2} + V_{xy}(x,y)\right]\mathrm{e}^{\mathrm{i}k_x x}Y(y) = \varepsilon_{xy}\mathrm{e}^{\mathrm{i}k_x x}Y(y). \tag{1.17}$$

Assume $V_x(x) = 0$ ($|x| \leqslant L_x/2$) and apply periodic boundary conditions in consideration of closed current loops around the sample, we have $k_x = \pm\frac{2n_x\pi}{L_x}$ ($n_x = 1, 2, 3, ...$). By defining the cyclotron frequency $\omega_\mathrm{c} = \frac{qB}{m^*}$ and the magnetic length (the smallest radius of a circular orbit in a magnetic field along which electrons gain a $2\pi$ phase) $l_B = \sqrt{\frac{\hbar}{|qB|}}$ and assuming $V_y(y) = 0$ ($|y| \leqslant L_y/2$), we have:

$$\left[-\frac{\hbar^2}{2m^*}\frac{\mathrm{d}^2}{\mathrm{d}y^2} + \frac{1}{2}m^*\omega_\mathrm{c}^2\left(y + l_B^2 k_x\right)^2 + V_y(y)\right]Y(y) = \varepsilon_{xy}Y(y). \tag{1.18}$$

This is a harmonic oscillator (HO) asymmetrically confined to a box. When $L_y \to \infty$, $Y_n(y, k_x) = |n, k_x\rangle$ are HO eigenstates centered at the guiding center positions $y_{k_x} = -l_B^2 k_x = -\frac{\hbar k_x}{qB}$ with eigenenergies:

$$\varepsilon_{xy} = \varepsilon_n = \hbar\omega_{\rm c}\left(n + \frac{1}{2}\right), \quad (n = 0, 1, 2, ...), \tag{1.19}$$

called Landau levels (LLs). We know from $y_{k_x} = -l_B^2 k_x = -\frac{\hbar k_x}{qB}$ that these states are chiral: the coordinates of the guiding centers $y(k_x)$ are opposite for electrons (or holes) traveling in opposite directions $k_x$ and $-k_x$,.

To model current transport, similar to the classical Hall effect, we can consider a uniform electric field $E_y$ applied to the sample. This induces a transverse voltage $V_y = E_y L_y$ across the sample, with scalar potential $\phi = -E_y y$ and additional potential:

$$\Delta V_{xy}(x, y) = q\phi = -qE_y y. \tag{1.20}$$

So, the new Hamiltonian is:

$$\begin{aligned} H_{k_x} &= -\frac{\hbar^2}{2m^*}\frac{{\rm d}^2}{{\rm d}y^2} + \frac{1}{2}m^*\omega_{\rm c}^2\left(y + l_B^2 k_x\right)^2 - qE_y y \\ &= -\frac{\hbar^2}{2m^*}\frac{{\rm d}^2}{{\rm d}y^2} + \frac{1}{2}m^*\omega_{\rm c}^2\left(y + l_B^2 k_x - \frac{qE_y}{m^*\omega_{\rm c}^2}\right)^2 - qE_y\left(-l_B k_y + \frac{qE_y}{m^*\omega_{\rm c}^2}\right) + \frac{1}{2}m^*\frac{E_y^2}{B^2} \\ &= \left(a_{y'}^\dagger a_{y'} + \frac{1}{2}\right)\hbar\omega_{\rm c} - qE_y y' + \frac{1}{2}m^* v_{\rm d}^2, \end{aligned} \tag{1.21}$$

where $v_{\rm d} = \frac{E_y}{B}$ is the drift velocity, $y' = -l_B^2 k_x + \frac{qE_y}{m^*\omega_{\rm c}^2} = -l_B^2 k_x + \frac{v_{\rm d}}{\omega_{\rm c}}$ are the new guiding centers shifted towards lower potential, and the last term is the additional gauge invariant kinetic energy. The new group velocity is:

$$v_{\rm g} = \frac{1}{\hbar}\frac{\partial\varepsilon_{n,k_x}}{\partial k_x} = \frac{qE_y l_B^2}{\hbar} = \frac{E_y}{B} = v_{\rm d}, \tag{1.22}$$

and the net current each state carries is:

$$\langle I_x\rangle = \int_{-\infty}^{\infty}\langle j_x\rangle{\rm d}y = \int_{-\infty}^{\infty}\frac{q}{m^*}\langle n, k_x|\hat{P}_x|n, k_x\rangle{\rm d}y = \frac{qE_y}{L_x B} = \frac{qv_{\rm d}}{L_x}. \tag{1.23}$$

Here $\hat{P}_x = -\mathrm{i}\hbar\frac{\partial}{\partial x} + A_x$ is the kinetic momentum. Therefore, one fully occupied LL carries the total current of:

$$I_x = \langle I_x \rangle \frac{L_y}{\Delta y} = \langle I_x \rangle \frac{L_y}{l_B^2 \Delta k_x} = \frac{qE_y}{L_x B}\frac{L_y q B L_x}{h} = \frac{q^2}{h} E_y L_y = \frac{q^2}{h} V_y, \tag{1.24}$$

which gives rise to a quantized conductance:

$$\sigma_{xy} = \frac{q^2}{h}. \tag{1.25}$$

The role of disorder, which is crucial to observing conductance quantization in experiment, will be discussed later in this section. Since for single carrier type, small current and transverse voltage, states with opposite momenta are largely spatially separated. If all the lower LLs are also occupied, due to a gap to the upper LLs, all backscatterings are blocked, leading to a longitudinal conductance:

$$\sigma_{xx} = 0. \tag{1.26}$$

Similarly, if we apply current in the $y$ direction, we have $\sigma_{yx} = -\sigma_{xy} = -\frac{q^2}{h}$ and $\sigma_{yy} = 0$. Therefore, unlike $\rho = 1/\sigma$ in 1D, the 2D conductivity and resistivity matrices are:

$$\overleftrightarrow{\sigma} = \begin{pmatrix} \sigma_{xx} & \sigma_{xy} \\ \sigma_{yx} & \sigma_{yy} \end{pmatrix} = \frac{q^2}{h}\begin{pmatrix} 0 & 1 \\ -1 & 0 \end{pmatrix}, \quad \overleftrightarrow{\rho} = \begin{pmatrix} \rho_{xx} & \rho_{xy} \\ \rho_{yx} & \rho_{yy} \end{pmatrix} = \overleftrightarrow{\sigma}^{-1} = \frac{h}{q^2}.\begin{pmatrix} 0 & -1 \\ 1 & 0 \end{pmatrix} \tag{1.27}$$

The transverse conductance in this 2D system seems analogous to the Landauer picture of transport in ballistic 1D wires [63]. Each full ballistic LL contributes to half of a conductance quanta $\frac{1}{2}G_0 = \frac{e^2}{h} = \frac{1}{R_\mathrm{K}}$, where the von Klitzing constant $R_\mathrm{K} = 25812.80745\,\Omega$ [64].

For an ideal finite 2D sample confined by an edge confinement potential $\Delta V_{xy}$ (originated in edge structure), we still start with the simplest case $\Delta V_{xy} = V(y)$. To keep the single-particle HO approximation valid, we assume that $V(y)$ is smooth within the width of an

eigenstate $\sqrt{n}l_B$ of any position $y_{k_x}$, so that if we expand $V(y)$ in series, the anharmonic terms higher than the second order are negligible, i.e.

$$\left.\frac{\partial^m V}{\partial y^m}\right|_{y_{k_x}} \ll \left(\frac{1}{\sqrt{n}l_B}\right)^{m-2} \left.\frac{\partial^2 V}{\partial y^2}\right|_{y_{k_x}}. \tag{1.28}$$

The anharmonic terms are treated as perturbations. The new Hamiltonian near the new guiding center $y'$ expanded in terms of $y - y_{k_x} = y + l_B^2 k_x$ up to the second order is:

$$\begin{aligned} H_{k_x} =& -\frac{\hbar^2}{2m^*}\frac{\mathrm{d}^2}{\mathrm{d}y^2} + \frac{1}{2}m^*\omega_\mathrm{c}^2\left(y - y_{k_x}\right)^2 + \frac{1}{2}\left.\frac{\partial^2 V}{\partial y^2}\right|_{y'}(y-y')^2 + \left.\frac{\partial V}{\partial y}\right|_{y'}(y-y') + V(y') \\ =& -\frac{\hbar^2}{2m^*}\frac{\mathrm{d}^2}{\mathrm{d}y^2} + \frac{1}{2}\left(m^*\omega_\mathrm{c}^2 + \frac{\partial^2 V}{\partial y^2}\right)\left[y - y_{k_x} + \left.\frac{\frac{\partial^2 V}{\partial y^2}(y_{k_x}-y') + \frac{\partial V}{\partial y}}{m^*\omega_\mathrm{c}^2 + \frac{\partial^2 V}{\partial y^2}}\right|_{y'}\right]^2 + V(y') \\ & - \left.\frac{\left[\frac{\partial^2 V}{\partial y^2}(y_{k_x}-y') + \frac{\partial V}{\partial y}\right]^2}{2\left(m^*\omega_\mathrm{c}^2 + \frac{\partial^2 V}{\partial y^2}\right)}\right|_{y'} + \frac{1}{2}\left.\frac{\partial^2 V}{\partial y^2}\right|_{y'}(y_{k_x}-y')^2 + \left.\frac{\partial V}{\partial y}\right|_{y'}(y_{k_x}-y'). \end{aligned} \tag{1.29}$$

As we notice:

$$y' = y_{k_x} - \left.\frac{\frac{\partial^2 V}{\partial y^2}(y_{k_x}-y') + \frac{\partial V}{\partial y}}{m^*\omega_\mathrm{c}^2 + \frac{\partial^2 V}{\partial y^2}}\right|_{y'}, \tag{1.30}$$

we can calculate the new guiding center by:

$$y' + \frac{1}{m^*\omega_\mathrm{c}^2}\left.\frac{\partial V}{\partial y}\right|_{y'} = y_{k_x} = -l_B^2 k_x. \tag{1.31}$$

So Eq. (1.29) can be simplified as:

$$H_{k_x} = \left(a_{y'}^\dagger a_{y'} + \frac{1}{2}\right)\hbar\omega_\mathrm{c}' + V(y') + \frac{1}{2}m^* v_\mathrm{d}'^2, \tag{1.32}$$

where the new cyclotron frequency and drift velocity are:

$$\omega_\mathrm{c}'^2 = \omega_\mathrm{c}^2 + \frac{1}{m^*}\left.\frac{\partial^2 V}{\partial y^2}\right|_{y'}, \quad v_\mathrm{d}' = -\frac{1}{m^*\omega_\mathrm{c}}\left.\frac{\partial V}{\partial y}\right|_{y'}. \tag{1.33}$$

Thus, $\frac{\partial^2 V}{\partial y^2}$ shifts the LL spacing $\hbar\omega_{\rm c}'$, acting as an effective magnetic field. When Eq. (1.29) is valid for $y_{k_x}$, i.e. $\left.\frac{\partial^2 V}{\partial y^2}\right|_{y_{k_x}} \approx \left.\frac{\partial^2 V}{\partial y^2}\right|_{y'}$, expand $\frac{\partial V}{\partial y}$ in Eq. (1.31) and Eq. (1.33), and we have:

$$v_{\rm d}' = -\frac{\omega_{\rm c}}{m^*\omega_{\rm c}'^2}\left.\frac{\partial V}{\partial y}\right|_{y_{k_x}}, \quad y' = y_{k_x} - \frac{1}{m^*\omega_{\rm c}'^2}\left.\frac{\partial V}{\partial y}\right|_{y_{k_x}} = y_{k_x} + \frac{v_{\rm d}'}{\omega_{\rm c}}. \tag{1.34}$$

Following Eq. (1.23), Eq. (1.34), and plugging in the new $|n, k_x, y'\rangle$ for Eq. (1.32), we get:

$$\langle I_x'\rangle = \int_{-\infty}^{\infty}\frac{q}{m^*}\langle n, k_x, y'|\hat{P}_x|n, k_x, y'\rangle {\rm d}y = \frac{q\omega_{\rm c}}{L_x}(y' - y_{k_x}) = -\frac{q\omega_{\rm c}}{L_x}\frac{1}{m^*\omega_{\rm c}'^2}\left.\frac{\partial V}{\partial y}\right|_{y_{k_x}}. \tag{1.35}$$

The current density contribution for every state is:

$$j_x'(y', y_{k_x}) = \frac{\langle I_x'\rangle}{\Delta y'} = \frac{q}{L_x m^*\omega_{\rm c}}\frac{1}{l_B^2\Delta k_x}\left.\frac{\partial V}{\partial y}\right|_{y_{k_x}} = \frac{q}{h}\left.\frac{\partial V}{\partial y}\right|_{y_{k_x}}. \tag{1.36}$$

Therefore, the total current through the sample is:

$$I_x' = \int_{-L_y/2}^{L_y/2} j_x' {\rm d}y = \frac{q}{h}\int_{-L_y/2}^{L_y/2}\left.\frac{\partial V}{\partial y}\right|_{y_{k_x}} {\rm d}y_{k_x} = \frac{q}{h}V\Big|_{-L_y/2}^{L_y/2} = \frac{q^2}{h}V_y', \tag{1.37}$$

which gives the same quantized conductance for a full LL as the linear potential case.

As we know, the guiding centers are near $y_{k_x} = -l_B^2 k_x = \pm\frac{n_y}{L_x}\frac{h}{qB}$, regardless of $2J+1$ spin degeneracy, the total number of states in a full LL is:

$$\frac{L_y}{\Delta y} = \frac{L_x L_y q B}{h}, \tag{1.38}$$

and the density of states (DOS) per unit area is:

$$n_B = \frac{eB}{h} = D(E)\hbar\omega_{\rm c}. \tag{1.39}$$

The LL filling factor $\nu$ is then defined as the number of filled LLs:

$$\nu = \frac{n_{\rm s}}{n_B} = \frac{n_{\rm s} h}{eB}. \tag{1.40}$$

Here $n_{\rm s}$ is the total carrier DOS.

From the discussions above, all allowed states can transport through the whole ideal sample. However, disorder always exists in real samples. According to Anderson [65] or Lifshitz [66], wavefunctions are localized within random disorder potentials in the band tails broadened from the ideal bands in the absence of magnetic fields. Localization in the LLs has also been studied [67], implying that the exponential localization length $\xi$, defined in $|\psi(\mathbf{r})|^2 \sim \mathrm{e}^{-\frac{|\mathbf{r}|}{\xi}}$ for localized states, diverges as the Fermi level approaches LL centers $\varepsilon_n$, $\xi(\varepsilon) \propto |\varepsilon - \varepsilon_n|^{-\gamma_n}$. For a finite sample, when $\xi$ exceeds a cutoff length of the sample size $L_{\rm s}$, e.g., the length of a Hall bar, localized states will be delocalized and able to carry current.

When adding disorder to the system, it is shown that the LL will be broadened by random disorder potentials $V_{\rm r}(\mathbf{r})$ [68]. Assume symmetric potential distribution $\langle V_{\rm r}(\mathbf{r})\rangle = V_0$ with spacial correlations:

$$\langle V_{\rm r}(\mathbf{r}) V_{\rm r}(\mathbf{r}')\rangle = W^2 f(\mathbf{r}-\mathbf{r}'), \tag{1.41}$$

where correlator $f(\Delta\mathbf{r})$ reflects the nature and range of the potential. Some typical potential distributions are white noise, Poisson, and Lorentzian distributions, etc. Take white noise [68] as an example, $f(\Delta\mathbf{r}) = \delta(\Delta\mathbf{r})$, with uncorrelated Gaussian distributions all over the space, in the limit of strong magnetic fields when different LLs decouple, the DOS for a single band can be analytically obtained, e.g., $D(\varepsilon)$ of $\mathrm{LL}_0$ [69]:

$$\begin{aligned} D(\varepsilon) &= \frac{2\sqrt{2}}{\pi W}\frac{eB}{h}\frac{\mathrm{e}^{\alpha^2}}{1+\left(\frac{2}{\sqrt{\pi}}\int_0^\alpha \mathrm{e}^{x^2}\mathrm{d}x\right)^2} = \frac{2\sqrt{2}}{\pi W}\frac{\mathrm{e}^{\alpha^2}}{1+\mathrm{erfi}(\alpha)^2} n_B, \\ \alpha &= \frac{1}{W}\sqrt{\frac{h}{eB}}\,(\varepsilon-\varepsilon_0) = \frac{1}{W\sqrt{n_B}}\left(\varepsilon - \frac{1}{2}\hbar\omega_{\rm c}\right), \end{aligned} \tag{1.42}$$

where $\mathrm{erfi}(\alpha)$ is the imaginary error function. It can be verified that $\int_{-\infty}^{+\infty} D(\varepsilon)\mathrm{d}\varepsilon = \frac{eB}{h}$ is the non-degenerate areal DOS. The full bandwidth of half density, corresponding to $\alpha = 1.390356 \approx \sqrt{2}$, is $\Gamma = 2\alpha W\sqrt{\frac{eB}{h}} \approx 2W\sqrt{2n_B} \propto W$. The maximum density $D(\varepsilon_0) =$

$\frac{2\sqrt{2}}{\pi W} n_B \propto \frac{1}{W}$. So we can control the bandwidth $\Gamma$ by the width and density of disorder potentials (e.g. impurities). Far from the $\mathrm{LL}_0$ center, $D(\varepsilon)$ has a Gaussian-like tail:

$$D(\varepsilon) \approx \sqrt{\frac{2}{W}} \frac{eB}{\pi^2 \hbar} \pi \alpha^2 \mathrm{e}^{-\alpha^2} \left[ 1 + \mathcal{O}\left( \frac{1}{\alpha^2} \right) \right], \quad (\alpha \to \infty), \tag{1.43}$$

and is flatter than a Gaussian near the center of $\mathrm{LL}_0$, as shown in the schematic Fig. 1.1:

$$D(\varepsilon) \approx \sqrt{\frac{2}{W}} \frac{eB}{\pi^2 \hbar} \left[ 1 + \alpha^2 \left( 1 - \frac{4}{\pi} \right) + \mathcal{O}(\alpha^4) \right], \quad (\alpha \to 0). \tag{1.44}$$

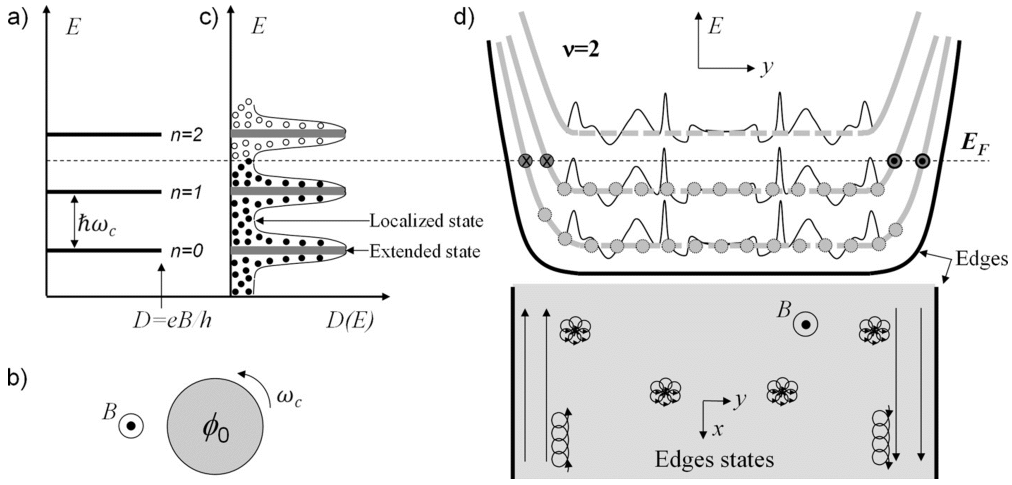


**Figure 1.1.** (a) Landau levels (LLs) in a ballistic 2D conductor. (b) Quantization of the cyclotron motion. (c) Density of states and (d) LLs, chiral extended edge states, and localized bulk states in a disordered 2D conductor. Reproduced from [70] under CC-BY 4.0.

The integer quantum Hall effect (IQHE) was discovered by K. von Klitzing *et al.* [64] in 1980, showing quantized Hall resistance and zero longitudinal resistance that exist at the same time, in agreement with Eq. (1.27). It was proposed by R. B. Laughlin that the disorder-broadened LLs can explain IQHE [71].

In the ideal case, assuming large $L_x$, $L_y$ and absence of edge potential $V_{xy}$, $Y_n(y, k_x)$ are HO eigenstates at guiding centers $y_{k_x} = -l_B^2 k_x$ with wavefunction width on the order of $\sqrt{n} l_B$. Comparing the area $2\pi n l_B^2$ each $\mathrm{LL}_n$ state occupies with the average area $2\pi l_B^2$ for each state in $\mathrm{LL}_n$, we can see that wavefunctions overlap more for higher LLs. When $\nu$ takes

exactly an integer value, all the $\nu$ lowest LLs are fully occupied, while all higher LLs are empty. Thus there is a gap for bulk excitations, and this incompressible 2DEG will turn out to be an insulator. The group velocity of the single particle $\varphi_{xy}$ is:

$$v_{\mathrm{g}} = \frac{1}{\hbar}\frac{\partial \varepsilon_{n,k_x}}{\partial k_x} = 0, \tag{1.45}$$

which means there is no current, either net or local, in the absence of edge potentials.

In finite-sized samples with confining potentials, electrons do not have to jump across the band gap $\Delta\varepsilon = \hbar\omega_{\mathrm{c}}$ in (de)excitation when $\nu$ is an integer, since the edges of the LLs are bent up to cover the gaps. When all the states carry non-zero current Eq. (1.23), $\sigma_{xy}$ will be proportional to $n_{\mathrm{s}}$ and change continuously with $B$. Thus, $\rho_{xy}$ will grow continuously and linearly with $B$ and reach $\frac{h}{\nu \mathrm{e}^2}$ only at a few certain points. The absence of a band gap in this case also causes scattering of states nearby. This could not explain the long quantized plateaus of $\rho_{xy} = \frac{h}{\nu \mathrm{e}^2}$ and the corresponding $\rho_{xx} = 0$ [64], which was demonstrated by Laughlin [71] and Halperin [72] to be due to the existence of disorder-induced localized states.

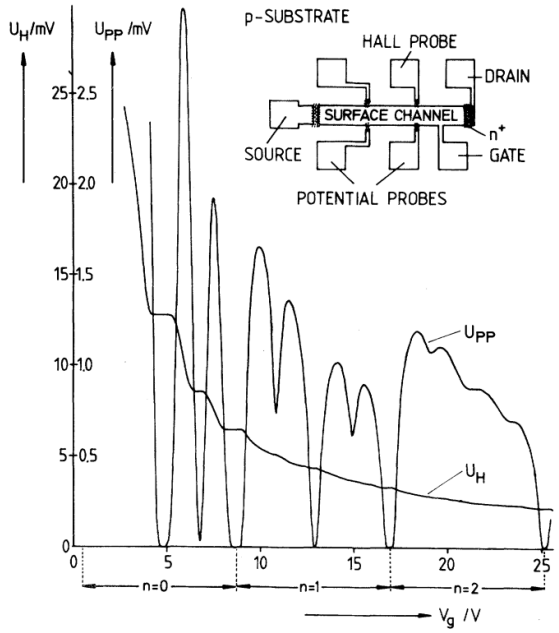


**Figure 1.2.** The integer quantum Hall effect (reproduced from [64], with the permission of the American Physical Society).

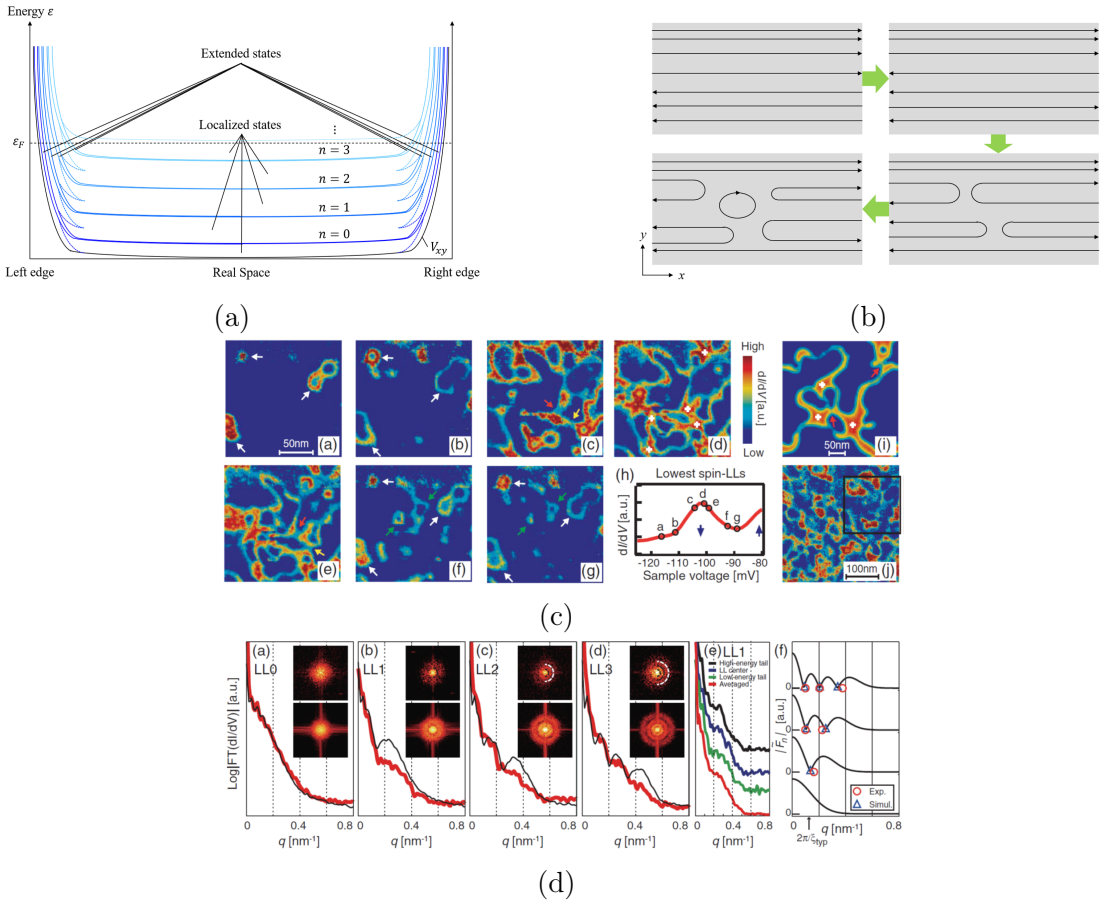


**Figure 1.3.** Schematic of transportation of (de)localized states. (a) Breadth of (de)localized states in real space. Areas between solid lines correspond to extended states. (b) Local current of drift states in a series of topological changes of potentials. (c) Local densities of states (LDOS) of the lowest Landau level (LL) in the bulk represented by differential conductivity d$I$/d$V$ at different source/drain voltages, using scanning tunneling spectroscopy. a-g/i are measured/calculated in 12 T, and j in 6 T close to the $LL_0$ center. White/green arrows mark drift states encircling potential minima/maxima; red/yellow arrows mark tunneling connections at saddle points; and white crosses mark extended areas. (Adapted from [73].) (d) Angular-averaged Fourier transformation of LDOS in the tail of some LLs obtained in experiments (red) and simulations (black), showing the ringlike structure of the LDOS in momentum space, and thus the randomly distributed ringlike LDOS in real space. The numbers and positions of nodes for the Fourier transform match in experiments and simulations. (Adapted from [74].) Reprinted with the permission of the American Physical Society.

Consider disorder-broadened LLs with localized states, Fig. 1.3(a). In this case, only extended states within a small vicinity $\Delta E$ from the center of LLs, whose localization lengths

exceed the sample size $\xi > L_{\rm s}$, contribute to net charge transportation through the sample. Before adding disorder, we first study the motion of guiding centers in a smooth (on the scale of $l_B$) 2D potential $V_{xy}$ where the HO approximation is valid. The time evolution of guiding center coordinates $(X, Y)$ in the Heisenberg picture is:

$$\begin{aligned} \mathrm{i}\hbar v_x' &= \mathrm{i}\hbar \frac{\mathrm{d}}{\mathrm{d}t}\langle X\rangle = [X, H] = [X, H_0 + V_{xy}] = [X, V_{xy}] = [X, Y]\,\frac{\partial V_{xy}}{\partial y} = \mathrm{i}l_B'^2 \frac{\partial V_{xy}}{\partial y} \\ \mathrm{i}\hbar v_y' &= \mathrm{i}\hbar \frac{\mathrm{d}}{\mathrm{d}t}\langle Y\rangle = [Y, H] = [Y, H_0 + V_{xy}] = [Y, V_{xy}] = [Y, X]\,\frac{\partial V_{xy}}{\partial x} = -\mathrm{i}l_B'^2 \frac{\partial V_{xy}}{\partial x}, \end{aligned} \tag{1.46}$$

where $H_0$ is the Hamiltonian for free carriers. The group velocity is therefore:

$$\mathbf{v}_{\rm g}' = \frac{l_B'^2}{\hbar}\left(\frac{\partial V_{xy}}{\partial y}, -\frac{\partial V_{xy}}{\partial x}\right) = \frac{\omega_{\rm c}^2}{\omega_{\rm c}'^2}\frac{1}{B^2}\left(\frac{\nabla V_{xy}}{q}\right) \times \mathbf{B} = \mathbf{v}_{\rm d}', \tag{1.47}$$

and:

$$\mathbf{v}_{\rm g} \cdot \nabla V_{xy} = \frac{\omega_{\rm c}^2}{\omega_{\rm c}'^2}\frac{1}{qB^2}\nabla V_{xy} \cdot (\nabla V_{xy} \times \mathbf{B}) = 0, \tag{1.48}$$

so the guiding centers always move along equipotential (generally $(n-1)$D regions for $n$D materials, like the diffusion transport of the surface states for 3D TIs).

We consider smooth and weak (negligible compared with edge potential) disorder potentials $V_{\rm r}$. We think of $V_{\rm r}$ as the composition of some random local disorder potentials randomly distributed across the sample. The distribution of $V_{\rm r}$ is not necessarily symmetric around the average. In the bulk, where the confining potential $V_{xy} \to 0$, as the example Eq. (1.42) shows, for symmetric $\langle V_{\rm r}\rangle = 0$, as the consecutive $V_{\rm r}$ must go across 0, only at the center of the band $V_{\rm r} = 0$ can the equipotential lines always extend to infinity, corresponding to the divergence of localization length at the center of the band. Away from the center to the maxima or minima of $V_{\rm r}$, the larger $|V_{\rm r}|$ becomes, the more the equipotential loops shrink; thus, $\xi$ decreases. For asymmetric $\langle V_{\rm r}\rangle$, $\xi$ still diverges at $V_{\rm r} = 0$ and converges to 0 as $V_{\rm r} \to V_{\rm r,max/min}$, while $\xi(\varepsilon)$ and $D(\varepsilon)$ are not symmetric about the band center.

As shown in Fig. 1.3(a), there are narrow intervals of extended states around LL centers in the bulk, whose widths decay as a power law with the sample size. If $|V_{\rm r}| \gtrsim \hbar\omega_{\rm c}$, the disorder bands of different LLs may overlap. In experiments, localized bulk states in 2D systems at the surface can be imaged using scanning tunneling spectroscopy (STS) [73], [74].

In Fig. 1.3(c), we can see that for $\varepsilon_{\rm a}$ and $\varepsilon_{\rm b}$ below the center of $\mathrm{LL}_0$, only states localized by negative $V_{\rm r}$ exist. At the same energy, a larger ring generally marks a stronger (deeper) $V_{\rm r}$. For instance, at $\varepsilon_{\rm a}$, the image shows the intercept of $V_{\rm r}(\mathbf{r})$ with $\varepsilon = \varepsilon_{\rm a} - \varepsilon_0$. The two coupled ring-like LDOS indicate deeper local disorder potentials than the two point-like ones. As energy increases to $\varepsilon_{\rm b}$, the structures that show up at $\varepsilon_{\rm a}$ expand to larger rings, and more localized states emerge, arising as new points. At $\varepsilon_{\rm c}$ and $\varepsilon_{\rm e}$, when reaching the center of an LL, much more localized states appear and start to connect (at saddle points marked by red/yellow arrows), leading to larger $\xi$. It is clear that shallower disorder potentials are more common than deeper ones. Within a narrow vicinity of an LL center, when some localization lengths exceed the sample size, the connected localized states turn into extended states (localization/delocalization transition [75]), marked by white crosses in the plot.

Recalling our discussion of the quantized conductance in a confining potential, we have noted that smooth 2D potentials do not affect the drift velocities of states and the current density contribution of each state. As the first three images in Fig. 1.3(b) show, when the total current $I$ stays the same, for any intercept between the source and drain, the current through should always be the net current $I$. We integrate the current density $\vec{j} = \frac{q}{h}\nabla V \times \hat{B}$ (here $\hat{B} = \frac{\vec{B}}{|B|}$, $\vec{j} \perp \nabla V$) along the path of intercept $\vec{r}' : \vec{r}'_1 \to \vec{r}'_2$ to get the net current:

$$\begin{aligned} I &= \int_{\vec{r}'_1}^{\vec{r}'_2} \vec{j} \cdot \mathrm{d}\vec{r}'_{\perp} = \int_{\vec{r}'_1}^{\vec{r}'_2} \vec{j} \cdot \left(\mathrm{d}\vec{r}' \times \hat{B}\right) = \int_{\vec{r}'_1}^{\vec{r}'_2} \frac{q}{h}\nabla V(\vec{r}') \times \hat{B} \cdot \left(\mathrm{d}\vec{r}' \times \hat{B}\right) \\ &= \int_{\vec{r}'_1}^{\vec{r}'_2} \frac{q}{h}\nabla V(\vec{r}') \cdot \mathrm{d}\vec{r}' = \frac{q}{h}\left[\mu\left(\vec{r}'_2\right) - \mu\left(\vec{r}'_1\right)\right] = \frac{q^2}{h}V_{\rm H}, \end{aligned} \tag{1.49}$$

if $\vec{r}'$ goes across all the states of a full LL. However, if we keep $V_{\rm H}$ steady but delete or add states with zero total current, although the total number of states across the intercept changes, the net current and $I$–$V_{\rm H}$ relation stay the same. According to Fig. 1.3(b), we may consider topological variance of disorder potential. Any operations on localized states or couples of extended states carrying opposite currents (which can be regarded as localized states with infinite localization lengths), including addition, removal, or any exchange within these states, which lead to no net current variation, do not affect the Hall conductance of an LL. Therefore, LLs do not have to be precisely full to generate Hall plateaus.

In the bulk, where confinement potential is negligible compared to disorder potential, the percentage of extended states is small. At the edges, increasing $|\nabla V|$ causes localized states to vanish exponentially. Once $|\nabla V| > |V_{\mathrm{r}}|_{\max}$, the edge states completely become extended states and dominate the current at small Hall voltages. Thus, in Fig. 1.3(a), when $\varepsilon_{\mathrm{F}}$ is far from bulk LL centers, the ratio of localized states to extended states at $\varepsilon_{\mathrm{F}}$ depends on the disorder potential. Scattering at low finite temperature depends on the states at $\varepsilon_{\mathrm{F}}$. As localized states do not carry net current through the sample, scattering between localized states does not affect the electric transport properties. However, scattering of extended states, either backscattering between extended states or scattering between extended states and localized states, changes the current, like in normal metals.

When $\varepsilon_{\mathrm{F}}$ is far from LL centers, the density of extended states is extremely low in the bulk, performing as an insulator. With this large insulating region in the bulk, it is hard for extended edge states to scatter through the bulk. In total, backscattering is almost negligible between LL centers, exhibiting wide Hall conductance plateaus and nearly zero longitudinal conductance. Near LL centers, with increasing density of extended states, scattering becomes more serious until reaching maxima at the LL centers. For $\sigma_{xy}$, when applying current through the sample, the dynamic scattering, which fades the current, competes with Hall voltage, which keeps the current. The dynamic process may be complicated, while intuitively, it will end up with an average current less than that of the contribution of a full LL. In $I$–$V$ measurement, it corresponds to the steep slope that connects two $\rho_{xy}$ plateaus.

To conclude, the dirtier the sample is, the higher the percentage of localized state is, and the wider the quantized Hall plateaus are. On the other hand, the cleaner the sample is, the wider the extended states exist, and the wider the nonzero $\rho_{xx}$ exhibits at low $T$. All the derivations in the generalized case do not rely on the shape of the sample and the distribution of disorder. The Hall voltage measured between any two edge points of the sample at the plateaus is the quantized Hall resistance multiplied by the net current between the two points and satisfies the above principles, protected by the topological (de)excitation of localized states, which does not affect the features in the long range.

Like the vortices in the topological phase of magnetism [76], the topological excitations in IQHE are localized states encircling local maxima or minima. When $\hbar\omega_{\mathrm{c}} > |V_{\mathrm{r}}|$, there will

only be one ring surrounding a local minimum or maximum at any $\varepsilon$. However, for weak magnetic fields such that $\hbar\omega_c < |V_r|$, there may be multiple rings encircling a local extremum at one energy. Thus, when disorder potentials are high or deep enough, or the magnetic field is not strong, one might observe a maximum of $\nu$ rings at the tails of $LL_\nu$ between $LL_{\nu-1}$ and $LL_{\nu+1}$ centers. In the meantime, rings less than $\nu$ will also be observable. As higher/deeper potentials are less frequent, the component of multiple rings should drop exponentially with $\nu$. In Fig. 1.3(c), similar scans are done to several LL tails [77], and the STS images are 2D Fourier transformed to show the structures in momentum space. In Fig. 1.3(d), the ring-like structures of LDOS in momentum space in the tails of different LLs match in experiments and simulations on the positions of local maxima and nodes.

IQHE does not only appear in the presence of magnetic fields but can also exhibit in systems with nonzero Berry curvature and nonzero Chern number, namely the anomalous quantum Hall effect [78]. The Berry curvature acts as an effective magnetic field. In such systems,

$$\sigma_{xy} = -\frac{e^2}{h} C_1, \tag{1.50}$$

where $C_1$ is the first Chern number calculated using the Berry curvature. For IQHE, $|C_1| = 1$ for a single filled LL. The relationship between the Hall conductance and the Chern number is referred to as the TKNN invariant [79]. $C_1$ manifests the topological feature of the IQHE, with $C_1 = 1$ inside the system and $C_1 = 0$ outside (e.g., in the vacuum). To satisfy the boundary conditions, the gap between neighboring LLs has to close at the edges, giving rise to the non-trivial chiral edge states. From the point of view of topology, the IQHE is a TI with a broken time reversal symmetry.

### 1.2.4 Fractional Quantum Hall Effect

Soon after IQHE was discovered in the $Si/SiO_2$ system [64], in a high-purity GaAs/AlGaAs heterostructure, apart from the integer Hall resistance plateaus, a new plateau with fractional filling factor emerges at lower temperatures and higher magnetic fields [80], namely the fractional quantum Hall effect (FQHE). Most generally, plateaus appear at odd-denominator

filling factors $\nu = \frac{q}{2p+1}$, with some rare plateaus at even-denominator filling factors like $\frac{1}{4}$, $\frac{1}{2}$, $\frac{3}{2}$, $\frac{5}{2}$ [81], [82].

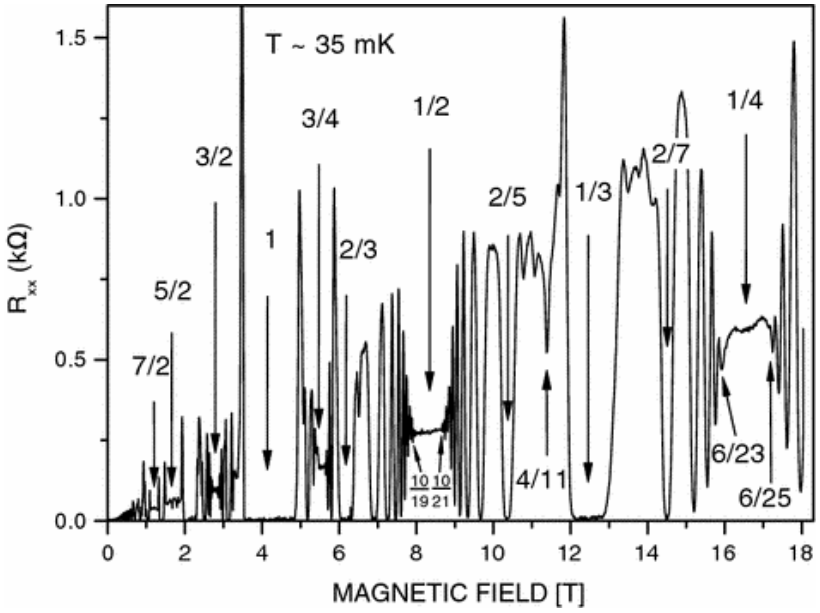


**Figure 1.4.** Longitudinal resistance of a high-mobility GaAs/AlGaAs quantum well. Some key fractional Landau level filling factors are marked. Reproduced from [83], with the permission of the American Physical Society.

In the single-particle Hartree-Fock approximation [84], [85] of weakly correlated many-body systems, for any external potentials or effective potentials in the mean field approximation, the behavior of a (dirty) system can always be described by LLs with integer filling factors. Therefore, in high-purity systems, the effect of strongly correlated many-body electron-electron ($e$–$e$) interactions has to be considered. The exact ground state depends on the many-body interaction potential. For a system with repulsive Coulomb pair potential in the limit that the range of interaction goes to zero,

$$V(|\mathbf{r} - \mathbf{r}'|) = V_0 \nabla^2_{\mathbf{r}} \delta(\mathbf{r} - \mathbf{r}'), \tag{1.51}$$

it is proved that the exact ground state is the Laughlin wavefunction [86], which is written in the ansatz of single-particle $LL_0$ wavefunctions as [87]:

$$\Psi_m = \prod_{i<j}(z_i - z_j)^m \mathrm{e}^{-\frac{1}{4l_B^2}\sum_k |z_k|^2}, \tag{1.52}$$

where $z_k = x_k + \mathrm{i}y_k$ are the complex coordinates of electrons/holes, $m = \frac{1}{\nu} = 2p \pm 1$ is an odd integer to guarantee an antisymmetric wavefunction.

Another example is for $\nu = \frac{1}{2p}$. For a system with three-body interactions of the form:

$$V(\mathbf{r}_1, \mathbf{r}_2, \mathbf{r}_3) = V_0 \nabla^2_{\mathbf{r}_1} \delta(\mathbf{r}_1 - \mathbf{r}_2)\delta(\mathbf{r}_1 - \mathbf{r}_3), \tag{1.53}$$

the exact ground state in the large magnetic field limit is the Moore-Read Pfaffian state [88]:

$$\Psi_{\mathrm{Pf},2p} = \mathrm{Pf}\left(\frac{1}{z_i - z_j}\right) \prod_{i<j}(z_i - z_j)^{2p} \mathrm{e}^{-\frac{1}{4l_B^2}\sum_k |z_k|^2}, \tag{1.54}$$

where $\mathrm{Pf}\left(\frac{1}{z_i - z_j}\right) = \mathcal{A}\left(\frac{1}{z_1 - z_2}\frac{1}{z_3 - z_4}\cdots\right)$ is the antisymmetric product over pairs of electrons and $\nu = \frac{1}{2p}$. There is a gap between all excited states, thus describing an incompressible state with quantized conductance. By particle-hole symmetry, there should be a conjugate anti-Pfaffian state with $\nu' = 1 - \nu = \frac{1}{2}$.

A more general Coulomb interaction potential may be $V(\mathbf{r} - \mathbf{r}') = \frac{e^2}{\epsilon|\mathbf{r} - \mathbf{r}'|}$, where $\epsilon$ is the background dielectric constant [89], while the exact functions can be even more complicated depending on the systems, which may lead to some new kinds of states.

The Laughlin wavefunction describes the FQHE at $\nu = \frac{1}{m}$ in the large magnetic field limit. For lower magnetic fields, the many-body wavefunction should contain some more complicated components of higher LL wavefunctions.

For partially filled LL, Laughlin states and Pfaffian states are two examples of antisymmetric many-body states that further lower the spatial density of states and the total energy. However, the Laughlin states could only explain $\nu = 1 - \frac{1}{2p \pm 1}$ plateaus. To explain some other

FQHE plateaus, composite fermion (CF) theory was introduced by Jain [90]. By attaching a Jastrow factor $\prod_{i<j}(z_i - z_j)^{2p}$ to non-interacting $\nu^*$ LLs:

$$\Psi_\nu = \mathcal{P}_{\mathrm{LL}_0} \prod_{i<j} (z_i - z_j)^{2p} \Phi_{\nu^*}, \tag{1.55}$$

we get the eigenfunctions of strongly interacting electrons at some new filling factors. The Jastrow factor attaches $2p$ flux quanta to each electron, which is interpreted as CFs. Inserting Eq. (1.55) into the many-body Schrödinger equation, we can change the Hamiltonian into a non-interacting Hamiltonian with an additional vector potential:

$$H = \frac{\hbar^2}{2m^*} \sum_i [\mathbf{p}_i + e\mathbf{A}(\mathbf{r})_i - e\mathbf{a}(\mathbf{r}_i)]^2 + V, \tag{1.56}$$

where $\mathbf{a}(\mathbf{r}_i) = 2p\phi_0 \frac{1}{2\pi} \sum_{j\neq i} \nabla_i \theta_{ij}$, and $\theta_{jk} = \mathrm{i} \ln(z_j - z_k)$. With external magnetic flux where a state sees $B/n_s$, the effective quantum flux for one state is $B/n_s - 2p\phi_0$. In other words, the effective magnetic field experienced by the CFs is:

$$B^* = B - 2pn_s\phi_0, \tag{1.57}$$

which can be in the same or opposite direction of $B$. The filling factors:

$$\nu^* = \frac{n_s}{n_{B^*}} = \frac{n_s\phi_0}{\pm(B - 2pn_s\phi_0)}, \quad \nu = \frac{n_s}{n_B} = \frac{\nu^*}{2p\nu^* \pm 1}. \tag{1.58}$$

The Fermi level will be at the highest effective LL ($\Lambda$-level):

$$\varepsilon_{\mathrm{F}} = (\nu^* + \frac{1}{2})\hbar|\omega_{\mathrm{c}}^*| = (\nu^* + \frac{1}{2})\hbar\omega_{\mathrm{c}} \frac{|B^*|}{B} = \left(\nu + \frac{|B^*|}{2B}\right) \hbar\omega_{\mathrm{c}}. \tag{1.59}$$

As $\nu^* \to \infty$, $\nu \to \frac{1}{2}$, and $B^* \to 0$, so $\varepsilon_{\mathrm{F}} \to \varepsilon_0$. That is, as $\nu : 0 \to \frac{1}{2}$, there will be a series of CF energy levels from 0 to $\varepsilon_0 = \frac{1}{2}\hbar\omega_{\mathrm{c}}$. The particle-hole conjugate of these states can be thought of as their reflection along $\varepsilon_0$ in a full LL, correlated with $\nu' = 1 - \nu$. From the discussion, we can see that the Laughlin states are just special cases of CF states with $\nu^* = 1$ and different $p$.

In multi-layer systems, when layers are close enough so that the interlayer Coulomb interactions are considerable, the QH states can be generalized [81]. For instance, the Laughlin wavefunctions for the two-component QH states in a (balanced) bilayer system can be of the form [91]:

$$\Psi^{\nu}_{mmk} \sim \prod_{i<j}(u_i - u_j)^m \prod_{i<j}(w_i - w_j)^m \prod_{i,j}(u_i - w_j)^k \mathrm{e}^{-\frac{1}{4l_B^2}\sum_i\left(|u_i|^2+|w_i|^2\right)}. \tag{1.60}$$

Here $m$, $k$ determine intralayer and interlayer correlations, while $u_i$, $w_j$ marks the complex coordinates of the electrons in the two layers. The total filling factor is $\nu = 2/(m+k)$.

Apart from these states, there could be many other many-body states that could lower the energy considering more complicated terms. And considering SOC, polarization is also possible in FQHE. As the sample becomes purer, more terms will be substantial so as for new fractional Hall plateaus to be observed.

### 1.3 Strained Ge/SiGe Quantum Well

Among common semiconductors, Ge/SiGe QW integrated on a Si substrate has the highest hole mobility and is compatible with the conventional Si-based semiconductor manufacturing process [19], [38], [44]. In Ge/SiGe heterostructures, robust type II band alignment can be produced in the band edge profile for strained $Si_{1-x}Ge_x$ alloys on $Si_{1-y}Ge_y$ relaxed substrate along the (100) direction [92], e.g., Ge/$Si_{1-y}Ge_y$ ($y \approx 0.8$) as shown in Fig. 1.5.

The strain at the interface between the strained layer and the substrate is given by the lattice mismatch:

$$\varepsilon_{||} = \frac{a_{\mathrm{SiGe}} - a_{\mathrm{Ge}}}{a_{\mathrm{Ge}}}, \tag{1.61}$$

where $a_{\mathrm{Ge}}$ and $a_{\mathrm{SiGe}}$ denote the unstrained in-plane lattice constants of Ge and underlying SiGe, respectively. To support strained Ge QW of reasonable thickness (10–30 nm), a high Ge concentration of $y \geqslant 0.6$ is required [19], [93] to avoid the introduction of dislocations into the strained layer. The compressive strain of the Ge QW induced by epitaxial growth produces a large splitting between heavy hole and light hole subbands, resulting in a 2DHG

of enhanced mobility due to reduced scattering and very light effective mass between $0.055m_e$ along the (110) direction and $0.035m_e$ along the (100) direction [19], [31], [44].

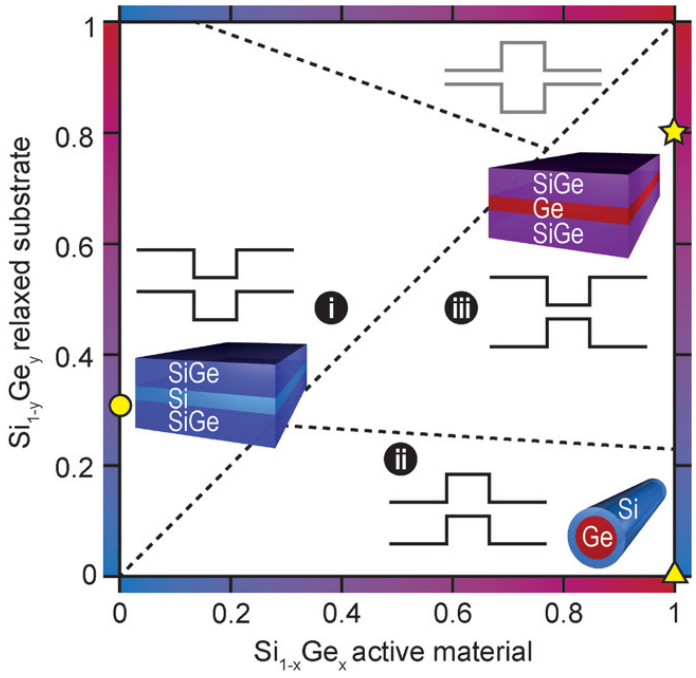


**Figure 1.5.** Schematic of SiGe heterostructure band edge profiles of strained $Si_{1-x}Ge_x$ alloy on $Si_{1-y}Ge_y$ relaxed substrate as a function of the Ge concentration $x$ in active material and $y$ in relaxed substrate. Reproduced from [44] under CC-BY-NC-ND, based on data from [92]. Reprinted with the permission of IOP Publishing.

On the fabrication of metal-oxide-semiconductor field-effect transistor (MOSFET) devices with Ge QW, due to the instability of Ge's native oxides and a high density of dangling bonds at the interface due to the several suboxides [38], the high hole mobility can be significantly degraded by carrier scattering related to these interface trap states. Growth of high-quality gate dielectric on Ge with low interface trap density has been a challenge in the semiconductor industry for over half a century. Although great effort has been put into it, the low growth temperature of Ge/SiGe QW to reduce interface roughness and retain compressive strain [31], [93] and, thus, the low thermal budget to prevent outdiffusion of Ge from the QW, make the search for proper gate dielectric more challenging.

### 1.3.1 Quantum Hall Ferromagnetic Transition

In the IQHE, each LL splits into two spin-polarized LLs due to the Zeeman effect: [94]

$$H_{\mathrm{Z}} = \frac{1}{2}\mu_{\mathrm{B}}\sigma\mathbf{g}\mathbf{B}, \tag{1.62}$$

where $\mu_{\mathrm{B}} = e\hbar/2m_{\mathrm{e}}$ is the Bohr magneton, $\sigma$ is the Pauli operator, $\mathbf{g}$ is the Landé $g$ tensor, and $\mathbf{B}$ is the magnetic field. For most semiconductors, $\mathbf{g}$ can be approximated by an in-plane $g_{||}$ and an out-of-plane $g_{\perp}$ component. Then Eq. (1.62) gives rise to a Zeeman splitting of:

$$E_{\mathrm{Z}} = \sqrt{(g_{\perp}\mu_{\mathrm{B}}B_z)^2 + (g_{||}\mu_{\mathrm{B}}B_{||})^2}, \tag{1.63}$$

or:

$$E_{\mathrm{Z}} = g_{\perp}\mu_{\mathrm{B}}B_z \tag{1.64}$$

for a strictly out-of-plane magnetic field.

We can label the spin-polarized LLs by their spin orientation $\uparrow$ or $\downarrow$ and their LL index $n$, with the lowest energy level having spin projection opposite to the field direction ($\downarrow$) for positive $g$ factor. As we have learned from Eq. (1.19), the cyclotron gap between neighboring LLs is $E_{\mathrm{c}} = \hbar\omega_{\mathrm{c}} = \hbar eB_z/m^*$, where $m^*$ is the in-plane effective mass. The ordering of the spin-polarized LLs depends on the ratio of the Zeeman splitting to the cyclotron energy $r \equiv E_{\mathrm{Z}}/E_{\mathrm{c}}$ [95]. When $r \approx 1$, $|n\uparrow\rangle$ and $|n+1\downarrow\rangle$ are nearly degenerate. In a purely out-of-plane magnetic field, $r = m^*g_{\perp}/2m_{\mathrm{e}}$. In most of the materials, $m^*$ and $g_{\perp}$ are set by the band structure. Enhancement of $r$ can be done by applying an in-plane magnetic field, which increases $E_{\mathrm{Z}}$ but leaves $E_{\mathrm{c}}$ constant. Another way to achieve large $r$ is to change $m^*g_{\perp}$ by many-body interactions, which can be controlled by carrier density [96]–[98]. We call the transition between spin-polarized LLs the quantum Hall ferromagnetic (QHFM) transition.

When $\varepsilon_{\mathrm{F}}$ lies between nearly degenerate $|n\uparrow\rangle$ and $|n+1\downarrow\rangle$ LLs, inter-carrier interactions play a dominant role and can lead to anomalous phase transitions not seen in single-particle pictures [36], [99], [100]. With the spin-polarized ground states, the system breaks into magnetic domains near the level crossing [99]. Transport at the domain walls results in

dissipation and can be characterized by a sharp resistance peak in $R_{xx}$ [100]. Such a resistance peak can be observed by applying an in-plane magnetic field [100].

For LL crossing coming from carrier interactions locally controlled by carrier density, such systems can have important applications in realizing non-Abelian excitations [36], [101]–[103].

The 1D helical edge channel—featuring counter-propagating holes (or analogously, electrons) with opposite spin polarizations—is essential for realizing high-order non-Abelian excitations in several systems [40], [41], [43], [104]. To construct such a helical edge channel, we can start from the chiral QH edge state. By creating a narrow local barrier in the QH system, we easily get two counter-propagating channels across the barrier, but with the same polarization, as shown in Fig. 1.6(a). To get edge states with opposite spins in the same magnetic field, generally, we can locally tune the carrier density with a gate to get to a neighboring LL with opposite polarization. As we see in Fig. 1.6(b), we can only get a single chiral edge channel at the interface and two spin-polarized states propagating in the same direction along the common edge.

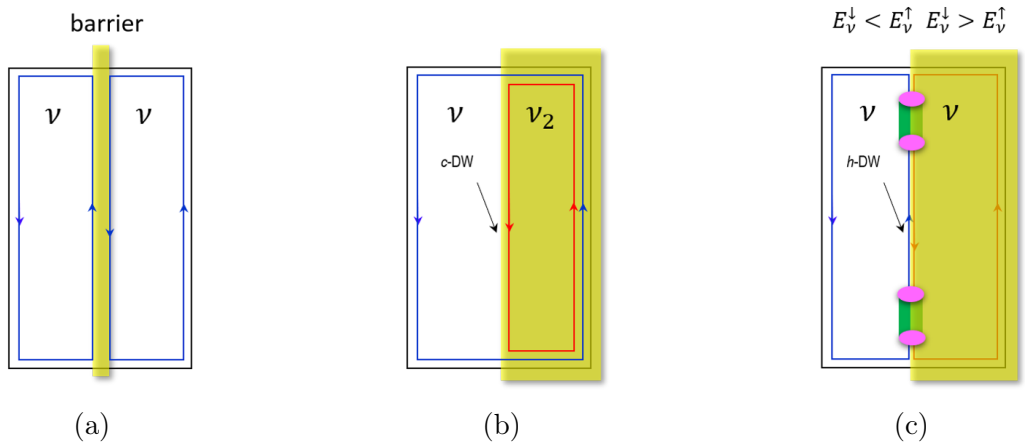


**Figure 1.6.** Constructing a 1-dimensional helical edge channel with quantum Hall ferromagnetic transition. (a) A potential barrier at a high magnetic field creates counter-propagating edge channels with the same spin polarization. (b) Local tuning of the filling factor by gating creates a chiral domain wall (c-DW) at the interface. (c) Local tuning of the spin polarization of the highest Landau level creates a helical domain wall (h-DW), where carriers with opposite polarization counter-propagate along the edge channels. When coupling the helical edge channel to superconducting contacts (green), non-Abelian excitations should form at the interface (magenta). Adapted from [101], with the permission of the American Physical Society.

However, systems with QHFM transition controlled by local gating enable 1D helical edge channels similarly [101]. By tuning the magnetic field and the local gate voltage, we let the gated and ungated regions lie in the same filling factor $\nu$ but across the QHFM transition. The two counter-propagating edge states at the highest LLs with opposite polarization form a 1D helical edge channel.

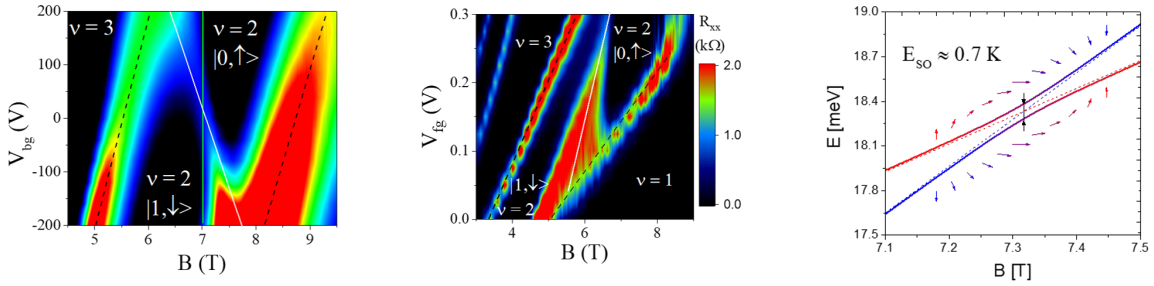


(a) (b) (c)

**Figure 1.7.** Quantum Hall ferromagnetic (QHFM) transition in the CdTe:Mn system at filling factor $\nu = 2$ controlled by (a) back gating and (b) front gating. (c) A small anticrossing gap is created due to spin-orbit coupling. Adapted from [101], with the permission of the American Physical Society.

The gate-controlled QHFM transition has been observed in several systems [36], [101]–[103]. In the CdTe:Mn system, Mn acts as a neutral impurity in $Cd_{1-x}Mn_xTe/Cd_{0.8}Mg_{0.2}Te$ QW and introduces a large $s$–$d$ exchange interaction between $d$ electrons in Mn and $s$ electrons in the QW [101]. In an external magnetic field, the energy spectrum of the system in the IQHE regime is:

$$E_n^{\uparrow\downarrow} = \left(n + \frac{1}{2}\right)\hbar\omega_c \pm \frac{1}{2}\left\{g^*\mu_B B + x_{Mn}E_{sd}\mathfrak{B}_s\left[\frac{g^*\mu_B SB}{k_B(T+T_{AF})}\right]\right\}, \tag{1.65}$$

where the first term is the IQHE LL spectrum, the second term is Zeeman splitting, and the third term is the $s$–$d$ exchange interaction energy. Here $g^* \approx -1.7$ is about a constant for CdTe, $x_{Mn}$ is the effective Mn concentration, $\mathfrak{B}(B,T)$ is the Brillouin function, and $T_{AF}$ comes from antiferromagnetic interaction between Mn. Gate voltage can induce an electric field in the $z$ direction that shifts the QW wavefunction and controls the overlap between $s$ electrons of CdTe and $d$ electrons of Mn in the QW, thus changing the $s$–$d$ exchange energy

and leading to LL crossing. Such level crossing has also been predicted in the FQHE regime and observed in the IQHE regime experimentally [101]. However, instead of a real crossing at $\nu = 2$, a small anticrossing gap is created due to SOC, indicating spin flip at the transition instead of a real level crossing. The development of superconducting contacts to CdTe:Mn is another challenge to realize non-Abelian excitations in this system.

The QHFM transition and helical edge channel are also observed in GaAs QW in the FQHE regime [103]. In GaAs/AlGaAs QW, Zeeman splitting remains simple $E_{\mathrm{Z}} \propto B$, and the cyclotron energy for CF is $E_{\mathrm{c}}^{\mathrm{CF}} = Ce^2/l_B \propto \sqrt{B}$, or more precisely $E_{\mathrm{c}}^{\mathrm{CF}} = Ce^2/\sqrt{l_B^2 + z_0^2}$, where $l_B = \sqrt{\hbar/eB}$ is the magnetic length, and $z_0$ is the expansion of the wavefunction in the $z$ direction. The difference between the field dependence of $E_{\mathrm{Z}}$ and $E_{\mathrm{c}}^{\mathrm{CF}}$ lead to the QHFM transition at $\nu = 2/3$. Due to the strong correlation of $\nu = 2/3$ state, helical edge channel built by such chiral edge states is expected to be more complex than simple overlapping of two non-interacting chiral modes. Although superconducting contacts to GaAs are possible with NbN [105], the critical field of the induced superconductivity is not yet high enough to reach the required field for the FQHE.

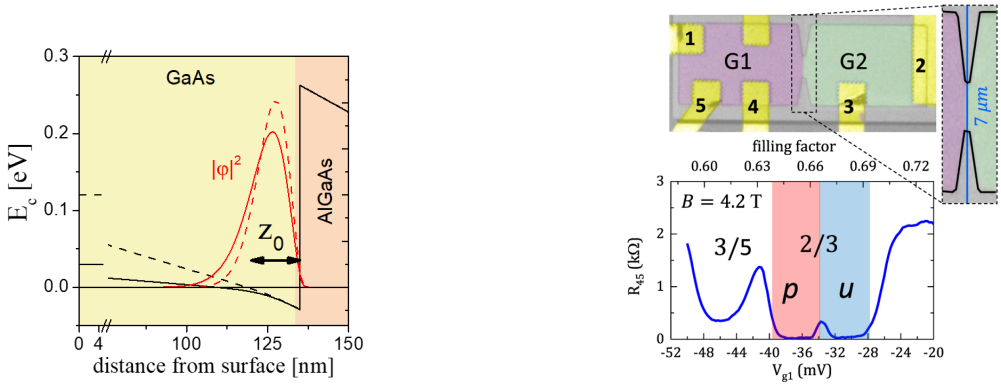


(a) (b)

**Figure 1.8.** Quantum Hall ferromagnetic (QHFM) transition in GaAs/AlGaAs quantum well (QW). (a) Band edge profile and wavefunction of GaAs/AlGaAs QW in growth direction, where $z_0$ is the expansion of wavefunction. (b) Sample structure and QHFM transition in GaAs/AlGaAs QW. (Adapted from [103] under CC-BY 4.0.)

The LL crossing and the QHFM transition observed in Ge/SiGe QW [36] are essential building blocks to realize non-Abelian excitations in Ge QW systems, which is the focus of our experiments. For holes in Ge, $g_\perp$ is mainly determined by the Luttinger parameters [106]. $m^*$ [107]–[109] and $g_\perp$ [37], [44], [110] can be significantly enhanced by inter-carrier interactions, which can be controlled by carrier density through local gating, due to the strong nonparabolicity of the valence band. Such enhancement has also been observed in other 2D systems like GaAs/AlGaAs [98] and MgZnO/ZnO [111], [112]. On wafer structure design, $m^*$ can also be tuned by the compressive strain [113], [114]. At low density, $r = m^* g_\perp / 2m_\mathrm{e}$ is expected to keep decreasing because of stronger many-body interactions and finally crosses 1, where QHFM transition occurs. In gated undoped Ge/SiGe QW, the LL crossing and QHFM transition at $\nu = 2$ occur and hole density $p \sim 2 \times 10^{10}\,\mathrm{cm}^{-2}$ and $B \sim 0.5\,\mathrm{T}$ [36]. Developing transparent superconducting contacts to Ge QWs that survive in high out-of-plane magnetic fields and maintaining high enough mobility at low carrier density remain challenging towards realizing Majorana excitations in strained Ge QWs.

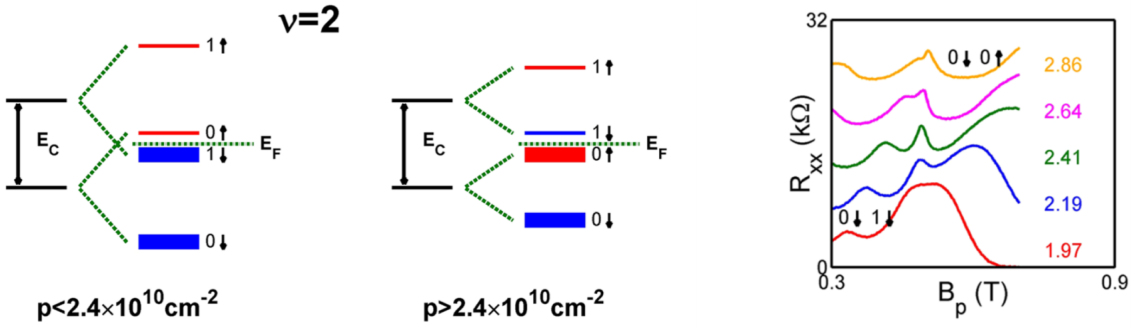


**Figure 1.9.** (a) Crossing of spin-polarized Landau levels in Ge/SiGe quantum well (QW) at filling factor $\nu = 2$ across a critical hole density $p = 2.4 \times 10^{10}\,\mathrm{cm}^{-2}$. (b) Quantum Hall ferromagnetic transition of Ge/SiGe QW near the critical density. (Adapted from [36] under CC-BY 4.0.)

## 1.4 Hybrid Superconductor-Semiconductor Systems

### 1.4.1 Andreev Reflection and Proximity Effect

According to BCS theory [53], [54], in conventional $s$-wave superconductors, pairs of electrons with opposite wave vectors $k$ and spins can form Cooper pairs through weak electron-phonon interactions.

We consider the interface between a normal conductor and a superconductor. Assuming $\varepsilon_{\mathrm{F}} = 0$ in the superconductor, for electrons (holes) with energy $|E| < \Delta$, single-particle transmission from normal material to superconductor is forbidden due to the lack of single-particle states on the superconductor side within the superconducting gap. However, a Cooper pair can be formed by taking an extra electron with opposite $k$ and spin from the Fermi sea on the normal side. Thus, the incident electron from the normal material forms a Cooper pair in the superconductor accompanied by the retroreflection of a hole. The hole possesses opposite spin and velocity but the same $k$ as the incident electron. The case is similar for incident holes. The group velocity of incident electrons (holes) is opposite from the retroreflected holes (electrons) because the effective mass of electrons and holes are opposite. This scattering process was discovered by A. Andreev in 1964 and is called Andreev reflection (AR) [115].

When two normal conductors are spatially separated by a thin superconductor of the order of $\xi_{\mathrm{BCS}}$, an incident electron at one interface becomes correlated with a retroreflected hole at the other interface, resulting in the same charge transfer as in a normal AR process [116]. Such non-local AR is called crossed Andreev reflection (CAR). However, the coexistence of normal AR, tunneling, and conventional scattering processes can mask the signature of CAR.

The picture of the proximity effect is based on Andreev reflection. When a normal conductor is in ohmic contact with a superconductor, the carrier order in one system is carried over to the other system. A suppressed superconducting gap appears in the superconductor near the interface, and a weak superconductivity is observed in the normal material over some mesoscopic distances [117], [118].

### 1.4.2 BTK Theory

G. E. Blonder, M. Tinkham, and T. M. Klapwijk (BTK) developed a general model for the $I-V$ curves to describe the normal-superconducting (N–S) contact behavior by including a barrier of arbitrary strength at the interface [119].

Considering the system clean enough for the momentum to be a good quantum number, we use the Bogoliubov-de Gennes (BdG) equation to deal with the interface by matching wavefunctions at the boundary. The BCS quasiparticle excitations in the superconductor are given by the Bogoliubov transformation as a superposition of electron-like and hole-like excitations:

$$\gamma_{k0}^{\dagger} = u_k c_{k\uparrow}^{\dagger} - v_k c_{-k\downarrow} \tag{1.66}$$

with well-defined $k$, since both $c_{k\uparrow}^{\dagger}$ and $c_{-k\downarrow}$ increase the total momentum of the system by an amount of $k$. In the simplest case where the order parameter $\Delta$, Fermi energy $\varepsilon_{\mathrm{F}}$, and potential energy $V = 0$ are position independent, the time-independent plane wave BdG equation is:

$$\begin{pmatrix} \frac{\hbar^2 k^2}{2m} - \varepsilon_{\mathrm{F}} + V & \Delta \\ \Delta^* & -\left(\frac{\hbar^2 k^2}{2m} - \varepsilon_{\mathrm{F}} + V\right) \end{pmatrix} \begin{pmatrix} u_k \\ v_k \end{pmatrix} = E \begin{pmatrix} u_k \\ v_k \end{pmatrix} \tag{1.67}$$

We obtain:

$$E^2 = \left(\frac{\hbar^2 k^2}{2m} - \varepsilon_{\mathrm{F}}\right)^2 + \Delta^2. \tag{1.68}$$

For $E > 0$ case, the BCS coherence factors and corresponding momenta are:

$$\begin{aligned} u_{k^\pm}^2 = 1 - v_{k^\pm}^2 = \frac{1}{2}\left(1 \pm \sqrt{\frac{E^2 - \Delta^2}{E^2}}\right), \\ \hbar k^{\pm} = \sqrt{2m(\varepsilon_{\mathrm{F}} \pm \sqrt{E^2 - \Delta^2})}. \end{aligned} \tag{1.69}$$

We define $u_0 = u_{k^+} = v_{k^-}$ and $v_0 = v_{k^+} = u_{k^-}$. For $E < 0$ case, $u_{k^\pm} = v_{k^\pm}^*$.

In the BTK model, normal/superconducting interfacial scattering is modeled by a potential barrier $H\delta(x)$ at the interface. A dimensionless barrier strength $Z = k_{\mathrm{F}} H / 2\varepsilon_{\mathrm{F}} = H/\hbar v_{\mathrm{F}}$, also called transparency, is introduced to simplify calculation. Due to the energy conservation, the energy of the incident electron and the retroreflected hole should be symmetric about $\varepsilon_{\mathrm{F}}$.

Therefore, for an incident quasiparticle with energy $\varepsilon_{\mathrm{F}} + E$, the time-independent plane wave BdG equation can be solved by plugging $V = H\delta(x) = (2\varepsilon_{\mathrm{F}} Z/k_{\mathrm{F}})\delta(x)$ into the single-particle Hamiltonian and using the quasiparticle wave of the form:

$$\begin{aligned}
\psi_{\mathrm{i}} &= \begin{pmatrix} 1 \\ 0 \end{pmatrix} \mathrm{e}^{\mathrm{i}q^{+}x}, \\
\psi_{\mathrm{r}} &= a \begin{pmatrix} 0 \\ 1 \end{pmatrix} \mathrm{e}^{\mathrm{i}q^{-}x} + b \begin{pmatrix} 1 \\ 0 \end{pmatrix} \mathrm{e}^{-\mathrm{i}q^{+}x}, \\
\psi_{\mathrm{t}} &= c \begin{pmatrix} u_0 \\ v_0 \end{pmatrix} \mathrm{e}^{\mathrm{i}k^{+}x} + d \begin{pmatrix} v_0 \\ u_0 \end{pmatrix} \mathrm{e}^{-\mathrm{i}k^{-}x}.
\end{aligned} \tag{1.70}$$

Here $\hbar q^{\pm} = \sqrt{2m(\varepsilon_{\mathrm{F}} \pm E)}$ are the momenta of electrons/holes on the normal side, $A = aa^{*}$, $B = bb^{*}$, $C = (u_0^2 - v_0^2)cc^{*}$, and $D = (u_0^2 - v_0^2)dd^{*}$ are the probabilities of AR, ordinary reflection, transmission without and with branch crossing. $N_{\mathrm{s}} = (u_0^2 - v_0^2)^{-1}$ is the normalized DOS in the superconductor, and $A + B + C + D = 1$ due to probability conservation.

For the normal state, $\Delta = 0$, we get:

$$B = \frac{Z^2}{1 + Z^2}, \quad C = \frac{1}{1 + Z^2}. \tag{1.71}$$

When $E > \Delta$, considering the simple case $k^{+} = k^{-} = p^{+} = p^{-} = k_{\mathrm{F}}$, the amplitudes:

$$\begin{aligned}
a &= \frac{u_0 v_0}{\gamma}, \\
b &= -\frac{(u_0^2 - v_0^2)(Z^2 + \mathrm{i}Z)}{\gamma}, \\
c &= \frac{u_0(1 - \mathrm{i}Z)}{\gamma}, \\
d &= \frac{\mathrm{i}v_0 Z}{\gamma},
\end{aligned} \tag{1.72}$$

which give rise to:

$$\begin{aligned} A &= \frac{u_0^2 v_0^2}{\gamma^2}, \\ B &= \frac{(u_0^2 - v_0^2)^2 Z^2 (1+Z^2)}{\gamma^2}, \\ C &= \frac{u_0^2 (u_0^2 - v_0^2)(1+Z^2)}{\gamma^2}, \\ D &= \frac{v_0^2 (u_0^2 - v_0^2) Z^2}{\gamma^2}. \end{aligned} \tag{1.73}$$

Here $\gamma = u_0^2 + (u_0^2 - v_0^2)Z^2$. When $E < \Delta$ within the gap, since there are no single particle states in the superconductor, $C = D = 0$, and:

$$A = \frac{\Delta^2}{E^2 + (\Delta^2 - E^2)(1+2Z^2)^2}, \quad B = 1 - A. \tag{1.74}$$

Specially, when $Z = 0$, all electrons with $E < \Delta$ are Andreev reflected. However, $k^{\pm}$ actually has an imaginary part when $E < \Delta$, which results in an exponential decay on a characteristic length scale $\hbar v_{\mathrm{F}} / 2\sqrt{\Delta^2 - E^2} \sim \xi$ before the current is converted into supercurrent. This describes the extension of carrier order from one system to the other in the proximity effect.

When we ground the superconductor and apply a voltage $V$ to the normal conductor, we can assume ballistic transport and equilibrium Fermi-Dirac functions as the distribution functions of all incoming particles for simplicity. All incoming electrons from the superconductor side have the distribution function $f(E, T)$, and $f(E - eV)$ for those from the normal conductor. Accounting for all different reflections and transmissions, we obtain the current between the normal conductor and the superconductor:

$$I_{\mathrm{NS}} = 2N(0) e v_{\mathrm{F}} \mathcal{A}_{\mathrm{c}} \int_{-\infty}^{+\infty} [f(E - eV, T) - f(E, T)][1 + A(E) - B(E)] \mathrm{d}E, \tag{1.75}$$

or:

$$I_{\mathrm{NN}} = \frac{2N(0) e^2 v_{\mathrm{F}} \mathcal{A}_{\mathrm{c}}}{1 + Z^2} V = \frac{V}{R_{\mathrm{N}}} \tag{1.76}$$

for above $T_c$. Here $N(0)$ is the DOS at $\varepsilon_F$ for each spin, and $\mathcal{A}_c$ is the effective cross-sectional area of the interface, and $f(E,T) = (1+e^{E/k_BT})^{-1}$ is the Fermi-Dirac distribution function. Therefore, we have:

$$\frac{I_{NS}(V)}{I_{NN}(V)} = \frac{1+Z^2}{eV}\int_{-\infty}^{+\infty}[f(E-eV,T)-f(E,T)][1+A(E)-B(E)]dE. \tag{1.77}$$

In the limit of $T \to 0$,

$$\frac{I_{NS}(V)}{I_{NN}(V)} = \frac{1+Z^2}{V}[1+A(eV)-B(eV)]V = (1+Z^2)[1+A(eV)-B(eV)]. \tag{1.78}$$

To compare more explicitly to the experiment, we calculate the differential resistance:

$$\begin{gathered}\frac{dI_{NS}}{dV} = 2N(0)ev_F\mathcal{A}_c\int_{-\infty}^{+\infty}\frac{df(E-eV,T)}{dV}[1+A(E)-B(E)]dE \\ \frac{dI_{NN}}{dV} = \frac{2N(0)ev_F\mathcal{A}_c}{1+Z^2} = \frac{1}{R_N}.\end{gathered} \tag{1.79}$$

More conveniently, we can calculate the ratio $R_N/R$:

$$R_N\frac{dI_{NS}}{dV} = (1+Z^2)\int_{-\infty}^{+\infty}\frac{df(E-eV,T)}{dV}[1+A(E)-B(E)]dE. \tag{1.80}$$

In addition, a parameter $\Gamma = \hbar/\tau_{qp}$ can be included to describe the energy broadening, which is associated with the finite lifetime $\tau_{qp}$ of the quasiparticles [120]. It can be done by simply replacing $E$ with $E+i\Gamma$ in $u_0$, $v_0$ and $\gamma$ of $A(E)$ and $B(E)$:

$$u_0^2 = 1-v_0^2 = \frac{1}{2}\left[1+\sqrt{\frac{(E-i\Gamma)^2-\Delta^2(T)}{(E-i\Gamma)^2}}\right]. \tag{1.81}$$

By fitting experimental $R_N/R$ to Eq. (1.80), we can easily extract the barrier strength $Z$ and energy broadening $\Gamma$.

### 1.4.3 Interplay of Superconductivity and Quantum Hall Effect


(a) (b)

**Figure 1.10.** Andreev bound states at the superconductor-normal interface in a strong magnetic field: (a) in the classical skipping orbit picture and (b) in the quantum mechanical picture. Adapted from [121], with the permission of the American Physical Society.

When a strong magnetic field within the critical field of a superconductor is applied to the interface of the superconductor and a 2DEG/2DHG perpendicular to the magnetic field, a link between AR and QHE is essential to study the transport across the interface [121]. The interface that is parallel to the magnetic field forces the nearby cyclotron orbits to move in skipping orbits along the interface in a classical qualitative picture [122], [123]. Applying this classical picture to the S–Sm interface, AR results in alternating electrons and holes in skipping orbits along the interface [124]. In the quantum mechanical picture, these alternating skipping orbits are described as current-carrying Andreev bound states (ABS) as coherent superpositions of electrons and holes propagating along the interface [121].

From our introduction of AR, the electron and hole in the AR process are opposite in the sign of both charge and effective mass. Therefore, in Fig. 1.10, electrons and holes propagate in the same chirality in the presence of a strong magnetic field. Similarly, in the quantum mechanical picture, the electron-like and hole-like Andreev excitations also have the same chirality.

We consider a planar interface at $x = 0$ between a semi-infinite superconductor region ($x < 0$) and a semi-infinite normal region ($x > 0$). In a real sample, this corresponds to a semiconductor junction length $L$ much larger than the cyclotron radius $r_{\mathrm{c}} = \hbar k_{\mathrm{F}}/eB$, so that current only transports through the edge state. A uniform magnetic field smaller

than the critical field of the superconductor is applied in $z$ direction. Neglecting the finite penetration depth, the magnetic field is screened in the superconductor region, leading to an abrupt change in magnetic field strength $H(x) = H_0\Theta(x)$, where $\Theta(x)$ is the Heaviside step function. Similarly, the superconducting pairing potential $\Delta(x) = \Delta_0\Theta(x)$. Following the BTK model [119], we use $V_{\text{ext}} = V_0\delta(x)$ to model the interface scattering. Choosing Landau gauge $\hat{\mathbf{A}}(x) = (0, H_0\Theta(x)\hat{x}, 0)$, we have the single particle electron/hole Hamitonians:

$$H_{0,\pm} = \begin{cases} \frac{p_x^2+p_z^2}{2m_{\text{N}}} + \frac{m_{\text{N}}\omega_{\text{c}}^2}{2}(x \mp X_{p_y})^2 - \varepsilon_{\text{F}}^{(N)}, & x > 0, \\ \frac{p_x^2+p_y^2+p_z^2}{2m_{\text{S}}} - \varepsilon_{\text{F}}^{(S)}, & x < 0. \end{cases} \tag{1.82}$$

Here operator $X_{p_y} = p_y l_B^2 \text{sgn}(\text{e}H_0)/\hbar$ is the guiding center coordinate.

Therefore, the ABS spectrum at the S–Sm interface can be calculated from the BdG equation:

$$\begin{pmatrix} H_{0,+} + V_{\text{ext}} & \Delta \\ \Delta^* & -H_{0,-} - V_{\text{ext}} \end{pmatrix} \begin{pmatrix} u \\ v \end{pmatrix} = E \begin{pmatrix} u \\ v \end{pmatrix}, \tag{1.83}$$

using the ansatz:

$$\begin{aligned} u(x, y, z) &= f_X(x)\text{e}^{\text{i}yX/l_B^2}\text{e}^{\text{i}k_z z}/\sqrt{L_y L_z}, \\ v(x, y, z) &= g_X(x)\text{e}^{\text{i}yX/l_B^2}\text{e}^{\text{i}k_z z}/\sqrt{L_y L_z}. \end{aligned} \tag{1.84}$$

We account for the motion in $z$ direction by renormalized Fermi energy $\tilde{\varepsilon}_{\text{F}}^{(\text{N,S})} = \varepsilon_{\text{F}}^{(\text{N,S})} - \hbar^2 k_z^2/(2m_{\text{N,S}})$. For a certain $X$ and $|E| < \Delta_0$, we match the wavefunction of a coherent superposition of electron and hole in the normal region:

$$\begin{pmatrix} f_X \\ g_X \end{pmatrix}_{x>0} = \begin{pmatrix} a\chi_{\varepsilon_+}(x - X) \\ b\chi_{\varepsilon_-}(x + X) \end{pmatrix} \tag{1.85}$$

with eigenvalues $\varepsilon_\pm = \tilde{\varepsilon}_{\text{F}}^{(\text{N})} \pm E$, to that in the superconductor:

$$\begin{pmatrix} f_X \\ g_X \end{pmatrix}_{x<0} = d_+ \begin{pmatrix} \gamma \\ 1 \end{pmatrix} \text{e}^{\text{i}x\lambda_-} + d_- \begin{pmatrix} \gamma^* \\ 1 \end{pmatrix} \text{e}^{-\text{i}x\lambda_+}, \tag{1.86}$$

where parameters $\gamma$ and $\lambda_{\pm}$ are defined as [125]:

$$\begin{aligned} \gamma &= \frac{\Delta_0}{E + \mathrm{i}\sqrt{\Delta_0^2 - E^2}}, \ |E| < \Delta_0 \\ \lambda_{\pm}^2 &= 2m_{\mathrm{S}} \left( \xi_q \pm \mathrm{i}\sqrt{\Delta_0^2 - E^2} \right), \ \xi_q = \varepsilon_{\mathrm{F}}^{(\mathrm{S})} - \frac{p_y^2 + p_z^2}{2m_{\mathrm{s}}}. \end{aligned} \tag{1.87}$$

We use a parameter $\nu = 2\varepsilon_{\mathrm{F}}^{(N)}/\hbar\omega_{\mathrm{c}} = 2(n_{\mathrm{s}}h/eB) = 2\nu_0$ to label the (spin degenerate) LL filling factor in the 2D gas region, $w = \sqrt{2m_{\mathrm{N}}V_0^2/\hbar^2\tilde{\varepsilon}_{\mathrm{F}}^{(\mathrm{N})}} = 2Z_{(\mathrm{BKT})}$ to measure interface scattering, and $s = \sqrt{\tilde{\varepsilon}_{\mathrm{F}}^{(\mathrm{S})} m_{\mathrm{N}}/\tilde{\varepsilon}_{\mathrm{F}}^{(\mathrm{N})} m_{\mathrm{S}}}$ to evaluate Fermi velocity mismatch.

For an ideal interface with perfect Fermi velocity matching ($s = 1$) but without interface scattering ($w = 0$), the spectrum is found to be:

$$\frac{\partial E}{\partial X} = -\frac{2\sqrt{2m_{\mathrm{N}}\tilde{\varepsilon}_{\mathrm{F}}^{(\mathrm{N})}}}{\hbar} \frac{\sqrt{\Delta_0^2 - E^2}}{1 + (\pi\sqrt{\Delta_0^2 - E^2})/(\hbar\omega_{\mathrm{c}})}, \tag{1.88}$$

where each band is labeled by the guiding center quantum number $X$.

For low energy $E \ll \min\left\{\Delta_0, \hbar\sqrt{\tilde{\varepsilon}_{\mathrm{F}}^{(\mathrm{N})}/(2m_{\mathrm{N}}X^2)}\right\}$, we have approximate dispersion:

$$\begin{aligned} E &= \Delta_0 \frac{(2n+1)\pi \pm \arccos(\Gamma_0) - 2X\sqrt{2m_{\mathrm{N}}\tilde{\varepsilon}_{\mathrm{F}}^{(\mathrm{N})}}/\hbar}{q + \pi\Delta_0/(\hbar\omega_{\mathrm{c}})}, \\ \Gamma_0 &= \frac{(s^2 + w^2 - 1)\sin(\pi\nu/2) + 2w\cos(\pi\nu/2)}{s^2 + w^2 + 1}, \\ q &= \frac{2s}{s^2 + w^2 + 1}. \end{aligned} \tag{1.89}$$

The hole probability $B \approx b^2$ is found to be:

$$B_\nu = \frac{1}{2} \frac{q^2/(1 - \Gamma_0^2)}{1 + \sqrt{1 - q^2/(1 - \Gamma_0^2)}}. \tag{1.90}$$

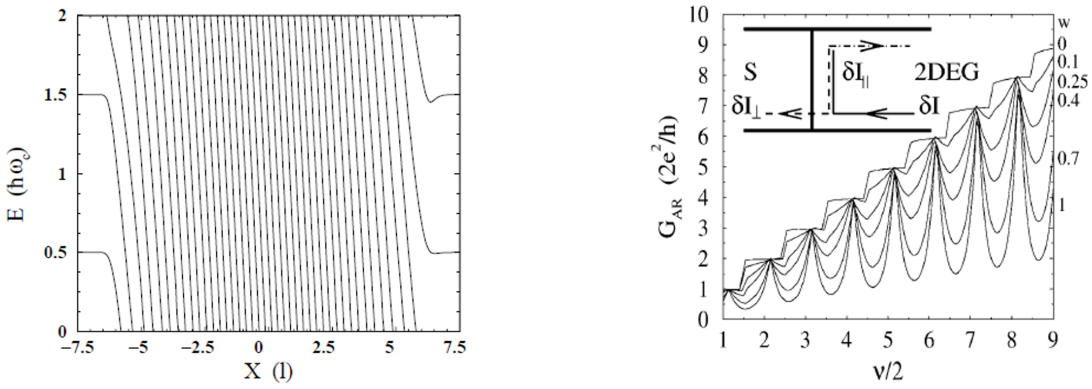


(a) (b)

**Figure 1.11.** (a) Andreev bound state levels at an ideal superconductor-normal interface in a strong magnetic field. (b) Contribution of Andreev reflection to small bias conductance $G_{\rm AR}$ for (non)ideal superconductor-normal interface in strong magnetic field, calculated from Eq. (1.91) with $\Delta_0 = 0.02\tilde{\varepsilon}_{\rm F}^{(\rm N)}$ and $s = 1$. The inset shows the current distribution of the chiral edge state at the interface. Adapted from [121], with the permission of the American Physical Society.

In the nonideal case, the ABS energies oscillate with $\nu$, which is also true for $B_\nu$ with minima at $\tan(\pi\nu/2) = 2w/(1 - s^2 - w^2)$. Therefore, the contribution of AR to the small bias conductance across the S–Sm interface is:

$$G_{\rm AR} = \frac{e^2}{\pi\hbar} \sum_{n=1}^{n^*} B_n, \tag{1.91}$$

as shown in Fig. 1.11(b), generalized from the Büttiker formalism [126]. The summation is over all ABS levels that intersect with $\varepsilon_{\rm F}^{(\rm N)}$, so that $n^*$ is twice the integer part of $\nu/2$. In experiments, $G_{\rm AR}$ can be directly measured as the two-terminal conductance in an S–Sm–S junction [127], [128]. The oscillatory $G_{\rm AR}$ has been observed in hybrid systems using, e.g., graphene [129]–[134], InAs [135], and ZnO [136]. The negative downstream resistance as another signature of ABS in the QH regime has also been observed [132], [133], [135]. Similarly, the negative downstream resistance resulting from CAR between QH edge states on both sides, which can be used to realize non-Abelian excitations [137], has been detected in graphene systems with narrow trench superconducting contacts [138], [139].

# 2. WAFER PROPERTIES AND EXPERIMENTAL TECHNIQUES

## 2.1 Wafer Characterization

All the strained Ge QW and $p^{++}$-Ge wafers we use in our experiment were grown using reduced pressure chemical vapor deposition (RP-CVD) in the laboratory of Prof. Maksym Myronov at the University of Warwick.

Fig. 2.1 shows an example of the Ge QW structure. A thick, relaxed graded SiGe/Ge buffer is grown on a Si(001) substrate to reduce strain and prevent cracks due to lattice constant mismatching. A boron modulation doping layer, such that carriers are spatially separated from donors, is placed below the Ge QW for better density control through the top gate, separated by a relatively thick top SiGe spacer for higher mobility. The Ge QW is capped with a thick SiGe spacer and an optional 2 nm Ge at the surface for ease of atomic layer deposition (ALD) of gate oxide. The list of Ge QW wafers is available in Appendix A.

| | |
|---|---|
| Ge cap | ~2nm |
| Si0.20Ge0.80 cap | 200nm |
| Ge QW | 15nm |
| Si0.20Ge0.80 spacer | 100nm |
| B (5e17/cm^3) Si0.20Ge0.80 spacer | 5nm |
| Relaxed graded Si0.20Ge0.80/Ge buffer | ~4500nm |
| $n^-$ (10-20 Ohm·cm) – Si <001> substrate | |

**Figure 2.1.** Ge/SiGe quantum well structure of wafer 19-219.

Wafers 19-218/219/220 have a thicker buffer and, as a consequence, larger stress and tend to create more cracks during sample cutting, which causes less controllable sample making and more waste of the wafers. Therefore, new sets of wafers, including 22-213, were grown with thinner buffers to reduce the probability of crack formation during processing. Some SiGe wafers (22-159/160, 22-211/212, 22-244/246) are used to characterize germanide superconductors by annealing platinum group metals (Ir, Pt, Pd, Rh) on (Si)Ge substrates.

Heavily doped $p^{++}$-Ge wafers were initially grown in a search for superconductivity in heavily B-doped Ge (expected for high doping levels of $> 3\%$). They were later used for Ge vertical junction research and preliminary superconducting contact tests. Fig. 2.2 shows an example of a $p^{++}$-Ge wafer, where a heavily doped strained Ge:B layer is directly grown on top of a relaxed Ge buffer.

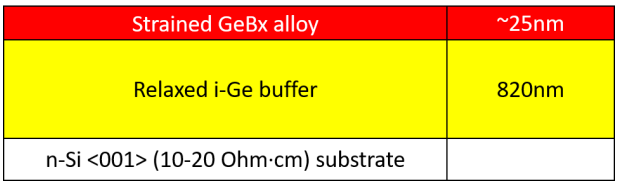


**Figure 2.2.** Structure of $p^{++}$-Ge wafer 21-316.

### 2.1.1 Basic Transport Measurement

Figs. 2.3 and 2.4 present characterizations of carrier density $p$ and mobility $\mu$ by top gate control for Ge QW wafers 19-218, 219, and 220.

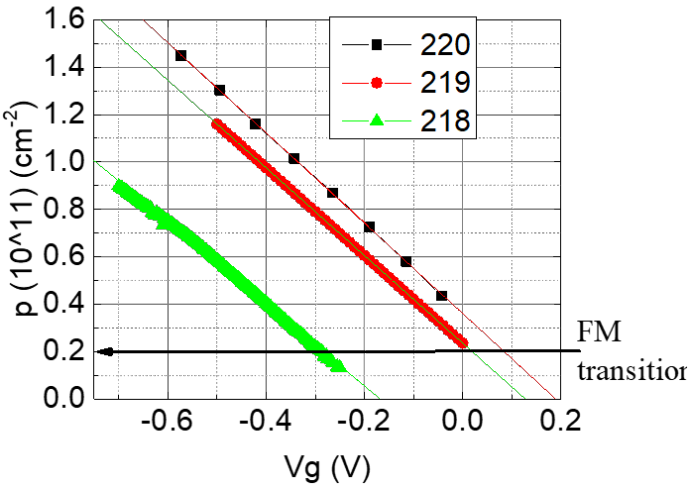


**Figure 2.3.** Carrier density $p$ vs. gate voltage $V_g$ for Ge quantum well wafers 19-218, 219, and 220. $AlO_x$ 40 nm/Al 300 nm gates were grown by thermal ALD and thermal evaporation. Fabrication and measurements were done by Dr. Ying Wang and Dr. Maxim Savchenko.

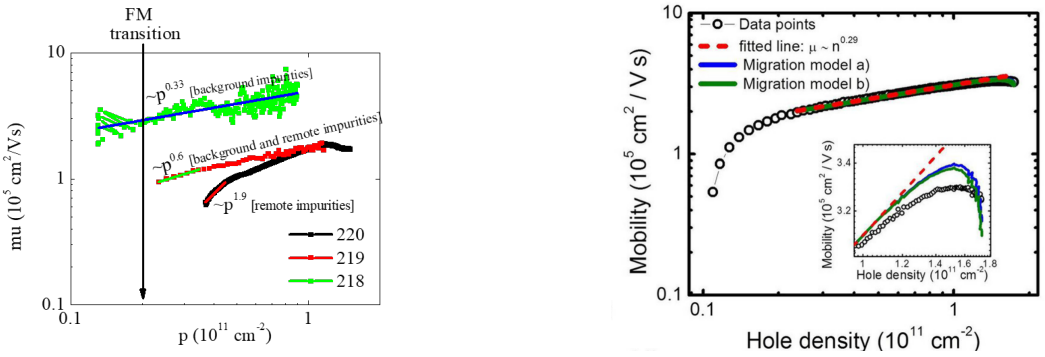


**Figure 2.4.** Mobility $\mu$ vs. hole density $p$ curves for (a) our Ge quantum well wafers 19-218/219/220 measured by Dr. Ying Wang and Dr. Maxim Savchenko, in comparison to (b) earlier research by D. Laroche *et al.*, adapted from [140], with the permission of AIP Publishing.

In these field effect transistor (FET) devices, 40 nm $AlO_x$ was first grown at 300 °C with Cambridge Nanotech Fiji ALD at the Birck Nanotechnology Center (BNC), and then a 150 nm Al gate was thermally evaporated in our lab. Details of the fabrication process are included in Appendix B.

The identical slopes in Fig. 2.3 show that when oxide is grown simultaneously on several samples, we get the same dielectric constant $\varepsilon_\mathrm{r}$ of $AlO_x$ and the same thickness of the oxide layer. We can model the heterostructure between the Al gate and the Ge QW as a plane capacitor, with dielectric constants and thicknesses of ALD $AlO_x$ and $Si_0.20Ge_0.80$ being $\varepsilon_{\mathrm{r,AlO}_x}$, $d_{\mathrm{AlO}_x} = 40\,\mathrm{nm}$, $\varepsilon_{\mathrm{r,SiGe}}$, $d_{\mathrm{SiGe}} = 200\,\mathrm{nm}$. For the plane capacitor with two layers of dielectric and areal charge density $\sigma = \mathrm{e}p$, the voltage across the capacitor is:

$$V = \frac{\sigma}{\varepsilon_0 \varepsilon_{\mathrm{r,AlO}_x}} d_{\mathrm{AlO}_x} + \frac{\sigma}{\varepsilon_0 \varepsilon_{\mathrm{r,SiGe}}} d_{\mathrm{SiGe}}, \tag{2.1}$$

where $\varepsilon_0$ is the vacuum permittivity. Therefore, we obtain the following expression of the slope $\mathrm{d}p/\mathrm{d}V_\mathrm{g}$ in Fig. 2.3:

$$\frac{\mathrm{d}p}{\mathrm{d}V_\mathrm{g}} = \frac{\varepsilon_0}{\mathrm{e}} \left( \frac{\varepsilon_{\mathrm{r,AlO}_x}}{d_{\mathrm{r,AlO}_x}} + \frac{\varepsilon_{\mathrm{r,SiGe}}}{d_{\mathrm{r,SiGe}}} \right)^{-1}. \tag{2.2}$$

The dielectric constant of Si is about 11–12, and that of Ge is about 16. If we assume $\varepsilon_{\mathrm{r,SiGe}} \approx 15$, by plugging $\mathrm{d}p/\mathrm{d}V_{\mathrm{g}} \approx 2.3 \times 10^{11}/(\mathrm{cm}^2 \cdot \mathrm{V})$ into Eq. (2.2), we get a low dielectric constant $\varepsilon_{\mathrm{r,AlO}_x} \approx 3.7$, which indicates low-quality ALD $\mathrm{AlO_x}$ films.

At the same $V_{\mathrm{g}}$, wafer with higher doping shows higher $p$. As $p$ increases, $\mu$ increases as a power law $\mu \propto p^{\alpha}$, where the exponent $\alpha$ depends on the scattering mechanism. For background charged impurity scattering $\alpha \sim 0.5$, for remote charged impurity scattering $\alpha \gtrsim 1.5$, and for interface roughness scattering $\alpha < 0$ [141], [142]. In Fig. 2.4, $\alpha \sim 0.33$, measured in 19-218 wafer with no intentional doping is consistent with $\alpha \sim 0.29$ reported in Ref. [140], where background charged impurity scattering is expected to be the dominant scattering mechanism. For wafers 19-219 and 220 with modulation doping, remote and background charged impurity scattering (in the case of boron segregation toward the QW region) become possible mechanisms. From Fig. 2.4, we conclude that for the 19-219 wafer, background impurity scattering remains the dominant scattering mechanism in the entire density range, while remote charged impurity scattering limits mobility at low densities in the 19-220 wafer with the largest doping concentration, indicating migration of boron into the QW region.

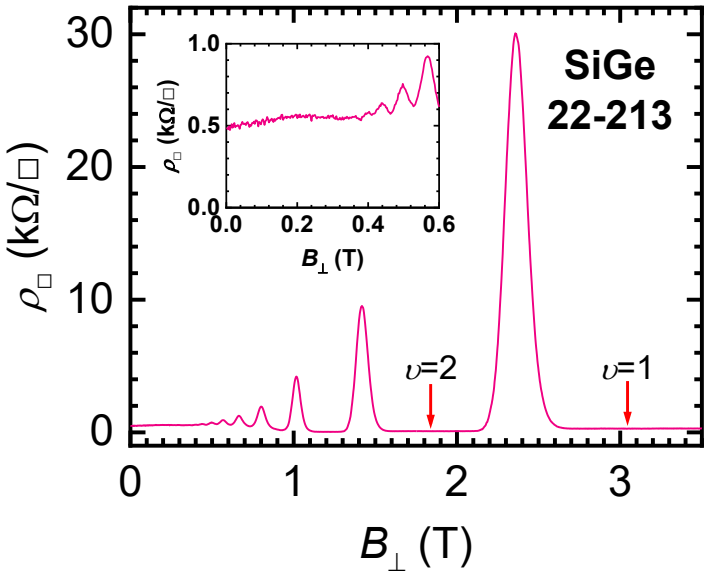


**Figure 2.5.** Shubnikov–de Haas oscillations of Ge quantum well wafer 22-213 upon arrival, with soldered In contacts and no other fabrication.

The Shubnikov–de Haas (SdH) oscillation of wafer 22-213 upon arrival without extra chemical treatment is plotted in Fig. 2.5. The wafer shows carrier density $p \approx 8.8 \times 10^{10}/\mathrm{cm}^2$ at $V_\mathrm{g} = 0$, comparable to that of 19-219/220. However, wafers 22-211 and 22-212, grown in series with 22-213 with a shallower top SiGe spacer, appear to be insulating without a gate. And within more than two years of attempts to induce carriers into 22-211/212 and all following deep/shallow Ge QW wafers by electrostatic gating, all other wafers except the four wafers plotted above are insulating regardless of fabrication process, which confused us. This issue was solved recently, which will be discussed later in Section 2.2.1.

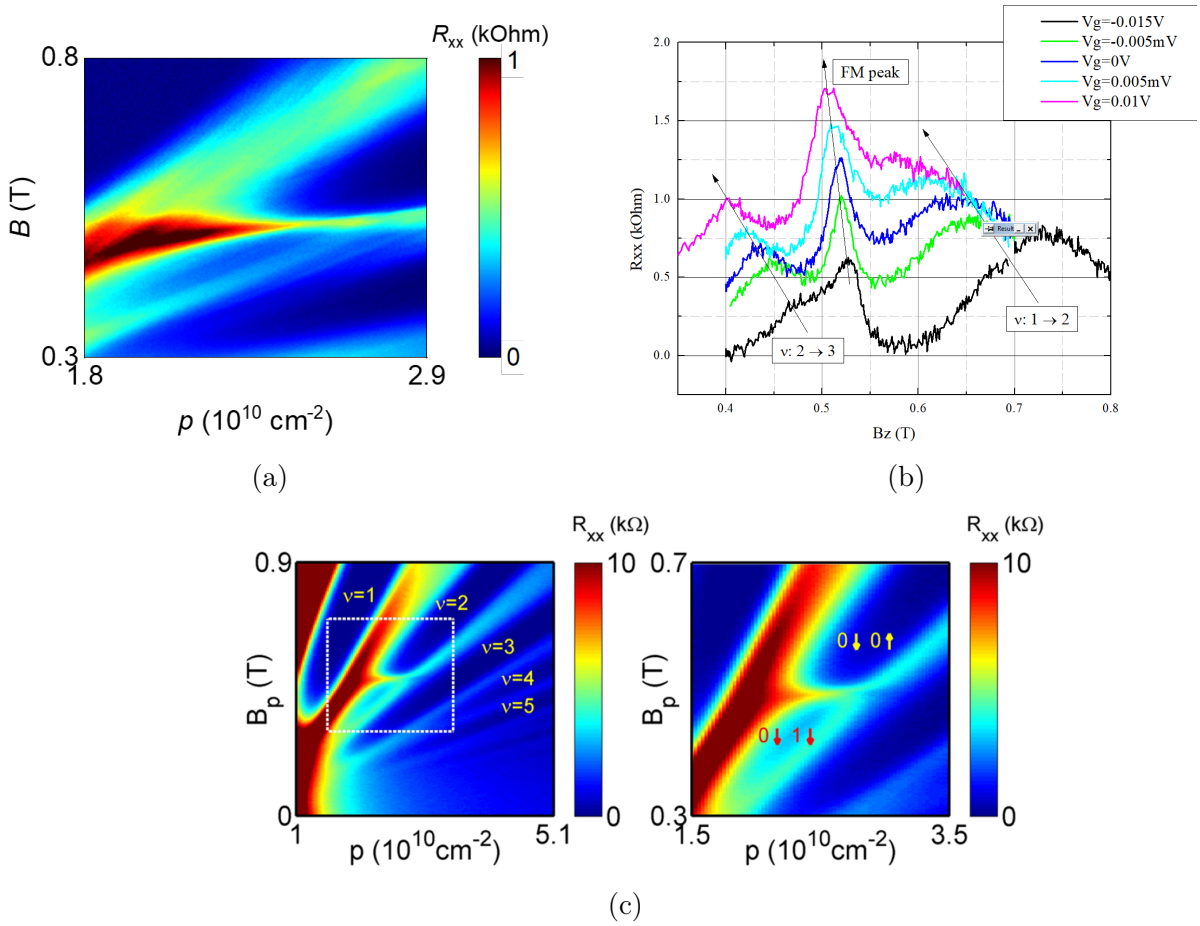


**Figure 2.6.** (a-b) Quantum Hall ferromagnetic transition observed in top-gated device fabricated with Ge quantum well (QW) 19-219, compared with (c) earlier measurement by T. Lu *et al.* in an undoped deep Ge QW (adapted from [36] under CC-BY 4.0). (a) is measured by Dr. Ying Wang and Dr. Maxim Savchenko at $T \sim 30$mK.

### 2.1.2 Quantum Hall Ferromagnetic Transition in Ge Quantum Well

The device made from wafer 19-219 in Fig. 2.4(a) is still conducting at very low density $p \sim 2\times10^{10}/\mathrm{cm}^2$ and remains good quantum mobility to observe QHFM transition. Therefore, we try to reproduce Fig. 2.6(c) in T. Lu *et al.* [36] with this device.

In Fig. 2.6(a), the hole density $p$ and the critical magnetic field $B^*$ of the QHFM transition are well-matched with those in Fig. 2.6(c). In both plots, a weak field dependence of the $R_{xx}$ peak is observed. Meanwhile, $R_{xx}$ does not reach zero on both sides of the peak, unlike the well-developed transition observed in CdTe:Mn [101] and GaAs [103] shown in Figs. 1.7 and 1.8. Therefore, to get clean helical edge channels made from strained Ge QW, we might need to find ways to improve the quantum mobility at low density. And if we cannot improve the gate dependence of the QHFM transition $B^*(V_\mathrm{g})$ so that the QHFM transition between two well-developed LLs can be controlled by gate at a fixed $B$, we will need to control the transition via an alternative approach. For example, we can use a ferromagnetic gate over the 2DHG to locally change the out-of-plane magnetic field that the 2DHG experiences.

## 2.2 Development of Nanofabrication Recipes of Ge QWs

### 2.2.1 Cleaning of Tools and Samples

In the CMOS industry and the fabrication of $\mathrm{Al/AlO}_x$ superconducting qubits, piranha cleaning is the standard cleaning procedure, which efficiently removes organic residues that can affect device yield and quality. However, Ge can react with the piranha solution ($\mathrm{H_2SO_4}$ 98%:$\mathrm{H_2O_2}$ 30%=3:1) [143], so we cannot clean our Ge QW wafers with piranha etch. Our cleaning procedure of tools (beakers and tweezers) and Ge QW samples is therefore initially the standard toluene-acetone-isopropanol (IPA) cleaning with agitation. However, our yield of gated devices of all Ge QW wafers except 19-218/219/220 and 22-213 remained zero for more than two years, regardless of other fabrication processes, including surface passivation or gate dielectric annealing.

In Ref. [144], it is found that the sample cleaning process between metal contact liftoff, contact annealing, and ALD dielectric growth can significantly affect contact resistance.

To study the efficiency of this cleaning process and rule out the effect of all other possible contamination, we first thoroughly clean all the beakers and tweezers that will be used during fabrication to remove organic residues and metal salts using piranha solution and aqua regia (HCl 37%:$HNO_3$ 69%=3:1) or at least one of them depending on the tool material. During fabrication, tools used in dirty processes that involve photoresists or metal salt-based developers (e.g., sodium-based AZ developer), including development and liftoff, are not mixed with other cleaner processes free of organic or metal salt contaminants.

Before ALD oxide growth, the samples are cleaned with toluene, acetone, dioxolane, and IPA, $> 5$ min each with ultrasonication, followed by TMAH etching for $< 1$ min (use the commercial MF-26A developer with 2.38% TMAH) and DI water rinse [144]. An additional IPA rinse can be done after the DI water rinse to better dry the samples. For between contact liftoff and annealing, an NMP cleaning (e.g., remover PG) can be added before IPA cleaning to remove resist residue.

Unlike Si, HF can only remove some kinds of native oxides of Ge, while HCl with a concentration not less than HCl:$H_2O = 1 : 4$ can effectively remove metal contamination and all types of $GeO_x$, leaving a Cl-terminated surface that remains stable in the air for hours [145]–[147]. The -Cl termination can be replaced by -F termination and finally by -H termination after further dipping in HF. The HF-cleaned Ge surface can remain passivated in air for $\sim 10$ min before re-oxidation. A long rinse with DI water can also lead to -OH termination at the Ge surface. Considering all these effects, we choose the following acid cleaning procedure: $HCl : DI = 1 : 4$ dip for 15 s–1 min, $HF : DI = 1 : 6$ (or 1:10) or buffered oxide etch (BOE) 6:1 dip for 10 s (for contact deposition) to 1 min (when there is no resist on samples), DI rinse 10 s–1 min, and $N_2$ blow dry, before immediate transfer to vacuum.

Since the cleanliness of the semiconductor-dielectric interface is crucial to reduce the interface roughness scattering, an optional thin ALD oxide protection layer can be deposited as the first step of lithography to protect the interface from other contaminants during fabrication. To test the efficiency of the protection layer, we start with 5 nm $AlO_x$ grown at 300 °C by thermal ALD, followed by rapid thermal annealing (RTA) at 450 °C for 75 s in forming gas ($N_2/H_2$). More details of the tests are presented in Section 2.2.6.

In our first test of applying these rigorous cleaning procedures of tools and samples, we are able to fabricate FET devices of 22-211 and 212 with high mobility, which appeared to be insulating in previous fabrications. All other solvent cleaning except dioxolane has been used before but has resulted in only insulating devices. An additional dioxolane is unlikely to be so efficient in solving all the problems. Presumably, organic residues from resist and other kinds of contaminants can accumulate on beakers and tweezers over time, migrate onto the samples during fabrication, and diffuse into the sample surface during high-temperature processes such as contact annealing and ALD growth. These contaminants might create a high density of uncompensated ionized acceptors $N_{\mathrm{A}}$ on the surface, fully screening the electrostatic gate of the Ge QW. These traps bend the valence band energy profile so that the Fermi level lies above the QW ground state, and no charge is accumulated in the device.

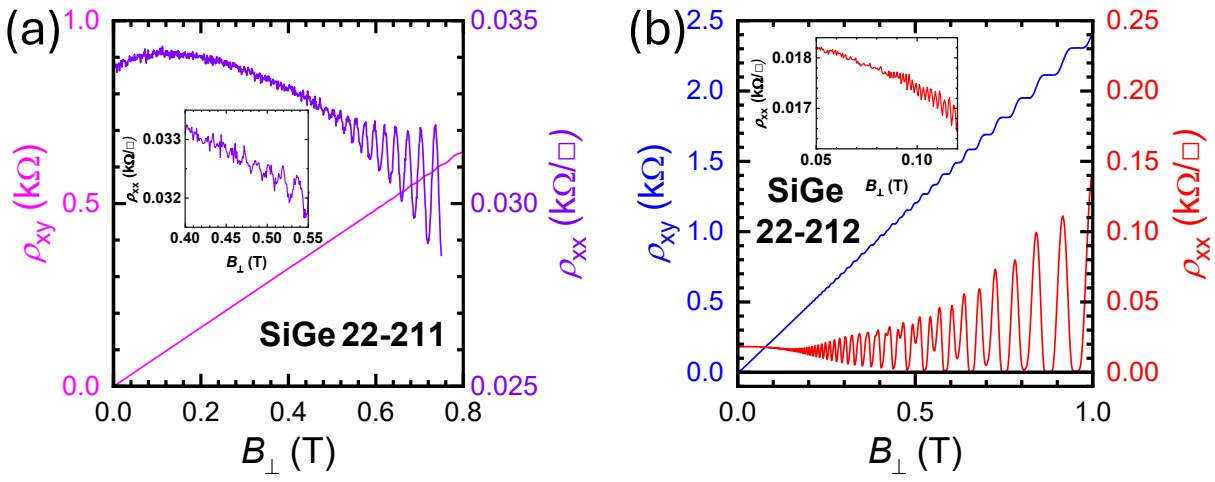


**Figure 2.7.** Shubnikov–de Haas oscillations and Hall resistivity of Ge quantum well wafers 22-211 and 212 at gate voltage $V_{\mathrm{g}} = 0$. The samples are fabricated after rigorous cleaning of beakers and tweezers with piranha solution and aqua regia solution. Wafers are cleaned by toluene-acetone-dioxolane-IPA-TMAH-DI with agitation. Additional HCl and BOE dipping is applied before the initial growth of 5 nm $AlO_x$ grown at 300 °C by thermal ALD. NMP (remover PG) cleaning is added between acetone-IPA cleaning after contact liftoff.

Fig. 2.7 shows the SdH oscillation and Hall resistivity of the FET devices of wafers 22-211 and 212 with 30 nm ALD $AlO_x$ grown at 300 °C and Ti/Au gate. The carrier density $p$ of both wafers is close to saturation at $V_{\mathrm{g}} = 0$. 22-212 with a 100 nm SiGe top barrier achieves

$\mu = 1.3 \times 10^6\,\mathrm{cm}^2/(\mathrm{V}\cdot\mathrm{s})$ at $p = 2.6 \times 10^{11}/\mathrm{cm}^2$, a mobility about 5 times higher than 22-211 with a thinner 20 nm SiGe top barrier. The onset of SdH oscillations occurs when the disorder broadening $\Gamma = \hbar/2\tau_\mathrm{q}$ of the LL is comparable to the cyclotron energy $\hbar\omega_\mathrm{c} = \hbar e B_\mathrm{SdH}/m^*$, or $\omega_c\tau_q \sim 1$. $B_\mathrm{SdH}$ can be used to estimate the quantum mobility using the empirical formula $\mu_\mathrm{q} = 1/B_\mathrm{SdH}$. We get $\mu_\mathrm{q} \approx 1.2 \times 10^5\,\mathrm{cm}^2/(\mathrm{V}\cdot\mathrm{s})$.

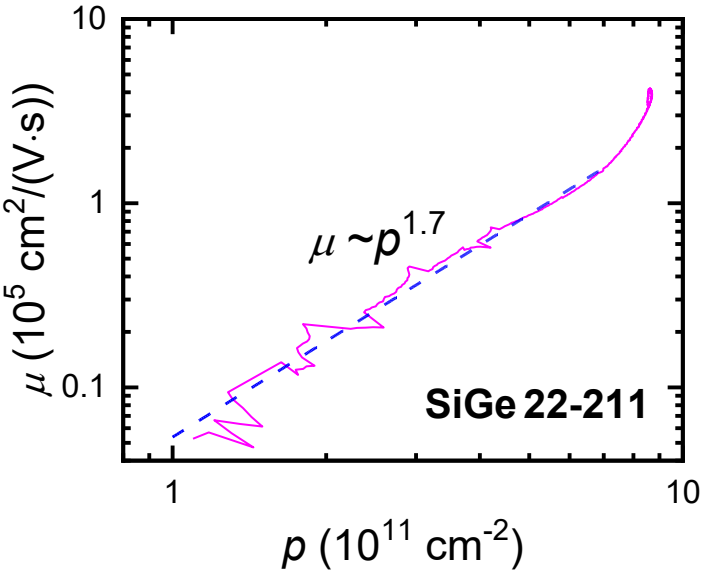


**Figure 2.8.** Mobility $\mu$ vs. hole density $p$ curve for Ge quantum well wafer 22-211.

The $\mu$ vs. $p$ curve for wafer 22-211 is plotted in Fig. 2.8. Within the entire range of carrier density accessible by gate control, we have a power law $\mu \sim p^{1.7}$. The large exponent $\alpha \sim 1.7 > 1.5$ indicates that the dominant scattering mechanism for this shallow Ge QW is remote charge scattering.

### 2.2.2 Optical Lithography

Optical lithography with a mask or maskless aligner is a fast way to obtain patterns with a feature size of $\gtrsim 1\,\mu$m using photoresist like AZ 1518 ($\approx 2\,\mu$m thick when spun at 3000-4000 rpm). For samples smaller than $5 \times 5\,\mathrm{mm}^2$, edge beads need to be removed, typically by Q-tip with acetone or scrubbing with a blade, to have hard contact with the mask and achieve $\sim 1\,\mu$m resolution. Metal ion-free developers based on tetramethylammonium

hydroxide (TMAH), e.g., MF-26A or AZ 726 MIF, are used to avoid metal ion contamination of samples. However, when surfaces with Al or $AlO_x$ are exposed, TMAH-based developers may need to be avoided due to reaction. Other developers, including sodium-based AZ developer:DI water=1:1, can be used in this case. Following the development process and to prevent scumming, the resist should be immersed or sprayed with the rinse liquid, here DI water, immediately. Otherwise, the residue is sometimes difficult to remove with additional development.

Compared to e-beam resist, photoresist is more resistant to dry etching and adheres better to Si or Ge surfaces. Hard baking can further improve adhesion in wet etching and pattern stability in dry etching by removing the residue developer, moisture, or rinse solvent from the resist. Therefore, optical lithography is a suitable option before dry/wet etching to increase selectivity or reduce undercut. The hard baking temperature should be carefully controlled to minimize pattern distortion and avoid cross-linking. Excessive soft or hard baking may also char the resist patterns, making them unable to dissolve in solvent. This residue may contaminate the samples during some subsequent high-temperature processes.

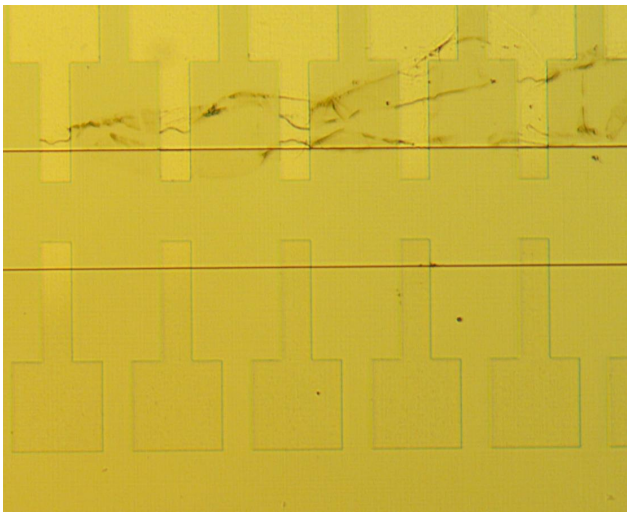

**Figure 2.9.** Optical image of the residue films of photoresist (irregular dark regions on the top) on an Ir/Ge quantum well sample after liftoff, likely due to excessive soft baking time of 3 min at 110–115 °C on a hotplate for AZ 1518 photoresist.

Fig. 2.9 shows an example of some thin films of photoresist residue that are observed after liftoff. The soft baking condition of this sample is 3 min at 110–115 °C on a hotplate for AZ 1518 photoresist. The baking time may be a bit excessive, so it chars or cross-links the resist surface. This kind of flake-like residue has sometimes been observed when the rinse after development or liftoff is not performed properly. Generally, the samples should remain in liquids until blowing/spinning dry, including when we transfer samples between different liquids.

A chlorobenzene soak for $\sim 10$ min before development can be used to create an overhang for easier liftoff. Hard baking is not recommended for liftoff because of the difficulty of stripping.

### 2.2.3 E-beam Lithography

E-beam lithography is used when the minimum feature size is $\ll 1\,\mu$m. We usually use PMMA 950k C4 ($\approx 400$ nm thick when spun at $\approx 4000$ rpm) or AR-P 6200.13 (CSAR 62) with a similar thickness. CSAR 62 is comparable to ZEP 520A e-beam resist and photoresists in dry etching resistance, which is about twice that of PMMA.

For small samples ($\sim 3\,\text{mm} \times 3\,\text{mm}$), the edge beads will be troublesome when we spin the resists at $\leqslant 2500$ rpm. Higher dilution resists will be needed to obtain thicker uniform films.

The dose has to be calibrated depending on the purpose of subsequent processes. Higher doses can usually be applied for undercut structures due to the proximity effect. For dry etching, vertical sidewalls are desired to increase the aspect ratio of etched structures.

The clean development of e-beam resists uses MIBK:IPA=1:1 to 1:3 or DI water:IPA=1:2 to 1:3, which should leave less residue than optical lithography. When using the same process conditions, the sensitivity of DI:IPA is considerably higher than MIBK:IPA and requires much lower doses. Cold development (4–10 °C) can help significantly improve resolution and contrast in this case.

The adhesion of e-beam resists to Si (or Ge) substrates is worse than that of photoresists. Hard baking is recommended before wet etching to reduce undercut. The hard baking temperature has to be limited due to the reflow that softens the top edges.

### 2.2.4 Wet Etching

We usually use the following wet etching recipe to etch SiGe: ($HF:H_2O_2:HAc = 1:2:3$):DI $H_2O = 1:3$ [148]–[151], where 30% $H_2O_2$ and > 99.7% acetic acid ($CH_3COOH$, HAc) are used, and HF is first diluted with DI water by 49% HF:DI=1:9. The etch rate at room temperature is about 100 nm/min, and the sidewall angle is about 20° to 25°. If HF is diluted by 49% HF:DI=1:4, we get an etch rate of 130 nm/min. Since the percentage of concentrated HF in the mixture is only about 0.4%, a small error in the ratio does not lead to a significant change in the etch rate, typically within 20-30%. When using the same mixture, the etch rate can remain accurate with < 2% error for at least about 6 hours.

An alternative etchant for Ge is dilute $HCl/H_2O_2$ [152], [153], which can effectively remove germanium oxides. Anisotropic etch of Ge can be achieved by tuning the concentration. Care must be taken in that concentrated solutions can potentially etch stainless steel, gold [154], and some other metals.

Ge can be oxidized in water or $H_2O_2$ to water-soluble $GeO_2$. For SiGe with Ge concentration > 60%, DI water and $H_2O_2$ are alternative etchants [154]–[156], whose etch rate can be controlled by etching temperature. We measure an etch rate of $\approx 4$ nm/min for diluted $H_2O_2$:DI $H_2O = 1:85$ and $Si_{0.15}Ge_{0.85}$ at room temperature. Dilute $H_2O_2$ has also been used to clean the native oxide layer of Ge [157]–[160].

When we protect the semiconductor-dielectric interface by ALD of a thin dielectric film before any other fabrication steps, the dielectric film has to be etched through before making contact to the Ge QW. So far, we have only tested 5 nm $AlO_x$ grown by thermal ALD at 300 °C as the protection layer. The results of the wet etch test for thin ALD $AlO_x$ films are as follows.

In dilute HCl:DI $H_2O = 1:6$, the etch rate of ALD $AlO_x$ is negligible < 1 Å/min. The etch rate in dilute HF:DI $H_2O = 1:10$ is > 24 nm/min, but HF wet etching creates a large

undercut of $> 200$ nm after only 20 s of etching, even if we use photoresist with good adhesion. As a result, we can use a short dip in dilute HCl to clean the SiGe samples with ALD $AlO_x$ protection layers, while HF cleaning should not be used on ALD $AlO_x$ films. It also prevents the attack of the e-beam resists by HF. The -Cl termination layer after HCl cleaning can be removed by *in situ* ion milling right before contact deposition.

A more controllable recipe for ALD $AlO_x$ wet etching is dilute TMAH. We measure a reproducible etch rate of 1.0 nm/min using MF-26A developer (containing 2.38% of TMAH) and a similar rate using AZ 726 MIF developer. The sidewall angle is only about 3° to 5°, so the $AlO_x$ layer between the electrodes in sub-micron JJs can possibly be removed due to undercut. Dry etching should be used instead to maintain the $AlO_x$ protection layer.

### 2.2.5 Dry Etching and Ion Milling

Following the procedures used on shallow Ge QWs [22]–[30], we etch perpendicularly just to the 15 nm-thick Ge QW for better proximity of superconducting contacts to the QW by $SF_6/O_2$ dry etching [161], using a Panasonic E620 ICP-RIE Etcher at BNC. The etching process is optimized to obtain reproducible etching depth with $\leqslant 2\%$ error. Dry etching of Ge using $SF_6$ is isotropic [162], and the additional $O_2$ helps to form a sidewall oxide and promote an anisotropic etch profile [161].

With a small RF bias power ICP/bias = 100/20 W, the dry etching sidewall profiles for both $CF_4$/Ar and $SF_6/O_2$ have visible overhang, as we see in Figs. 2.10(a) and 2.10(b). Since $CF_4$/Ar etching looks more isotropic, while the $SF_6/O_2$ etching profile can be tuned by $SF_6/O_2$ gas flow ratio [161], we choose $SF_6/O_2$ etching with different gas contents and power settings to get the desired profiles for mesas and contacts. The sharp upper edge of the sidewall and the isotropic profile of $CF_4$/Ar make this recipe not suitable for mesa etching or contact etching regarding contact continuity and good proximity to Ge QW.

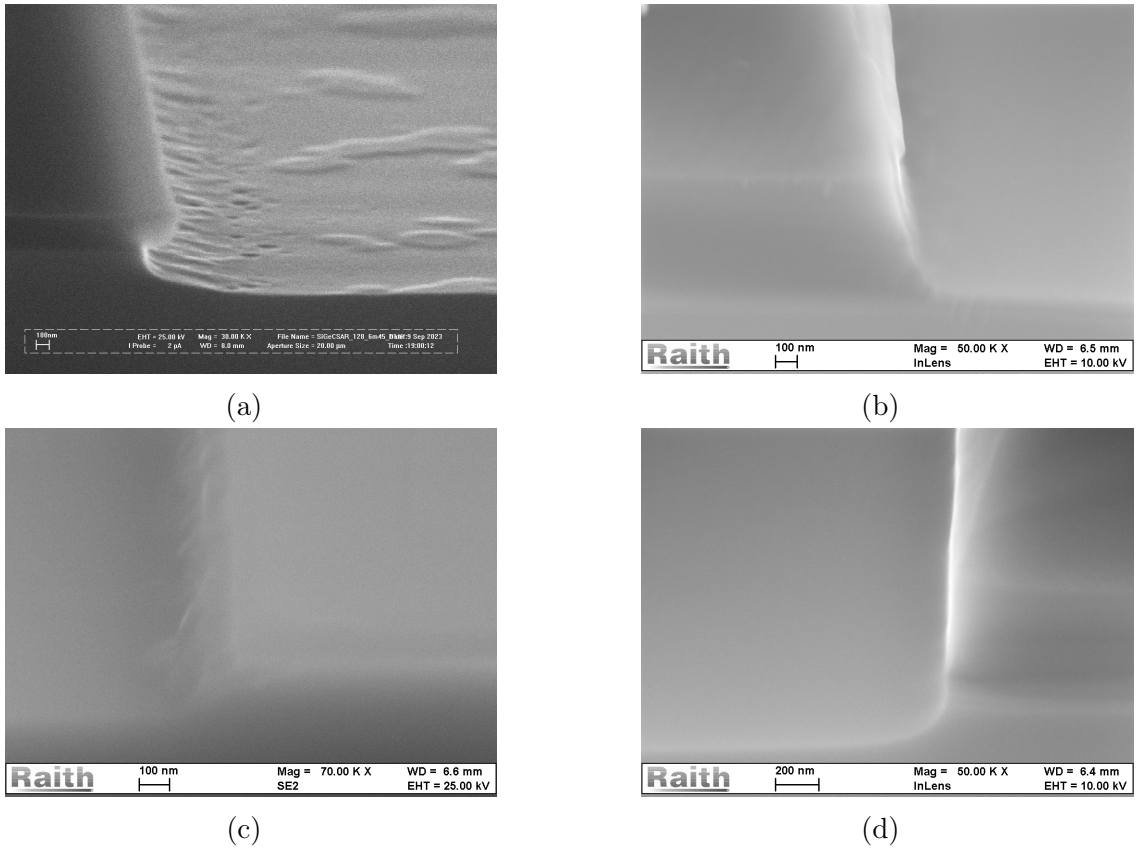


**Figure 2.10.** SiGe dry etching profile of (a) gas flow $CF_4/Ar = 70/10$ sccm, $P = 6$ Pa, RF power ICP/bias = 100/20 W; (b) $SF_6/O_2 = 20/10$ sccm, 1.35 Pa, ICP/bias = 100/20 W; (c) $SF_6/O_2 = 20/10$ sccm, 1.35 Pa, ICP/bias = 50/50 W; and (d) $SF_6/O_2 = 15/15$ sccm, 1.35 Pa, ICP/bias = 50/50 W, using Panasonic E620 ICP-RIE Etcher at Birck Nanotechnology Center, Purdue University. (a) uses AR-P 6200.13 e-beam resist spin coated at 4000 rpm ($\sim 400$ nm), (c) uses AR-P 6200.13 at 2500 rpm ($\sim 500$ nm), and (b,d) uses AZ1518 photoresist at 3500 rpm ($\sim 2\,\mu$m).

For $SF_6/O_2$ etching, we have tested the gas flows $SF_6/O_2 = 10/20$, 15/15, or 20/10 sccm, and the RF powers ICP/bias = 100/20 or 50/50 W. From etching tests with PMMA 950 C4 and AR-P 6200.13 e-beam resists, the selectivity to SiGe at ICP/bias = 100/20 W is $\sim 2:1$ for PMMA and $\sim 1:1$ for AR-P resist. 200 nm of contact etching can already consume all PMMA 950 C4, so AR-P 6200.13 is the better choice for deep mesa and contact etching with about the same resolution as PMMA. However, when ICP/bias = 50/50 W, the selectivity of the AR-P resist decreases to $\sim 1:2$ at least for $SF_6/O_2 = 20/10$ sccm. Therefore, to allow

contact etching to the 200 nm QW, we need to use thicker layers of resist $\sim 500$ nm (slower spin coating speed 2500 rpm).

The sidewall angle we measured follows the same trend as described in Ref. [161]. $SF_6/O_2 = 10/20$ sccm results in more isotropic etching with a $> 90°$ sidewall angle. $SF_6/O_2 = 15/15$ sccm creates a mostly vertical sidewall, as shown in Fig. 2.10(d). $SF_6/O_2 = 20/10$ sccm generates a sidewall angle of $\theta \sim 60°$, according to Figs. 2.10(b) and 2.10(c). As overhang is not an issue for mesa etching, ICP/bias = 100/20 W and $SF_6/O_2 = 20/10$ sccm is chosen to avoid resist consumption in etching and have a less steep sidewall to ensure contact continuity. For contact etching, since the overhang might interfere with the metal deposition in that its shadow can cause disconnection between the metal contact and the Ge QW, we can choose ICP/bias = 50/50 W and $SF_6/O_2 = 15/15$ or 20/10 sccm depending on the requirement. Because the discontinuity in the valence band edge profile of Ge/SiGe QW originates from strain, ideally, a vertical sidewall should allow for better contact, especially for our deep Ge QW. The strain gradient on a flatter sidewall will result in a gradient and reduction of the confining potential near the contact, thus causing a bad connection between the contact and the QW.

Concerning the serious attack on the resists due to the oxygen content in the $SF_6/O_2$ recipe, we test Cl-based recipes that are free of oxygen. When SiGe substrates are coated with an $AlO_x$ protection layer/hard mask, Cl-based recipes are required for $AlO_x$ dry etching. The selectivity of $AlO_x$ over SiGe is >100 using the $SF_6/O_2$ recipe, so $AlO_x$ is a good material as a hard mask in $SF_6/O_2$ dry etching. Fig. 2.11 shows the dry etching profile of $BCl_3$/Ar recipes using AZ1518 as the mask. The $BCl_3$-rich recipe creates a smooth etched SiGe surface with an etch rate of $\sim 6$ nm/min and a selectivity a few times higher than the $SF_6/O_2$ recipes. A sidewall angle of $> 45°$ is created after etching without overhang. The Ar-rich recipe shows an etch rate of $\sim 20$ nm/min and creates a rough etched SiGe surface.

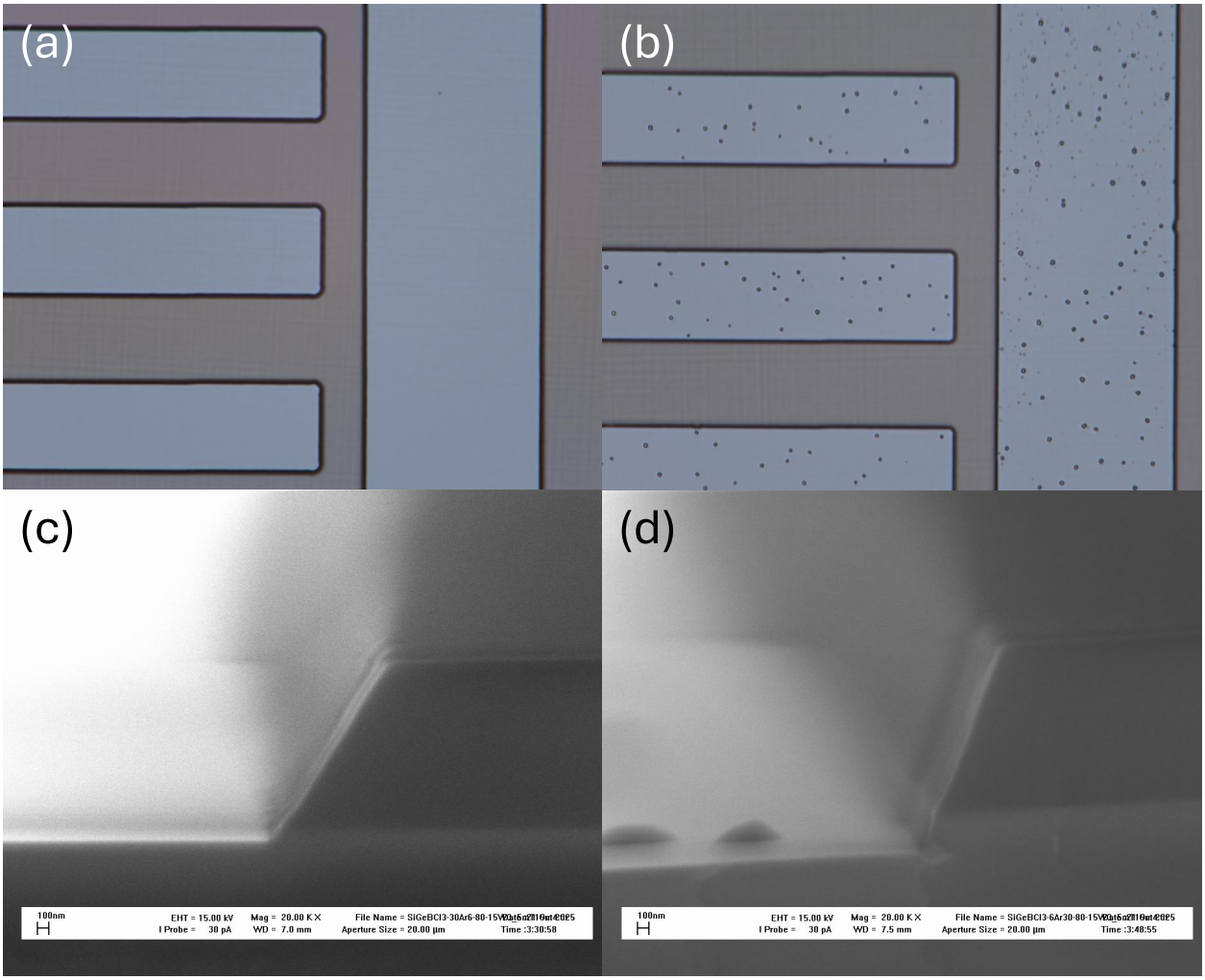


**Figure 2.11.** SiGe dry etching profile of (a,c) $BCl_3/Ar = 30/5$ sccm and (b,d) $BCl_3/Ar = 5/30$ sccm with RF power ICP/bias = 100/50 W, pressure $P = 3.5$ mTorr, using AZ1518 resist as the mask. The spinning speed is 5000 rpm and dose is $\sim 20\,mW/cm^2 \times 5.2$ s using a mask aligner. The photoresist is not stripped after etching. The darker regions (c,d) are resist layers, and the brighter regions below are the etched SiGe substrates.

However, the sidewall profile is also affected by the resist profile after development, especially when selectivity is low. The ideal resist profile for dry etching would be a vertical sidewall. As we did not know the profile of photoresist before dry etching in Figs. 2.10(b,d) and 2.11, and we do see non-vertical resist profiles after etching, the etching profile may need to be recalibrated with the optimal resist profile.

Ion milling is useful for etching thin layers of materials, for example, the native oxide layer on the sample surface. We use Ar ion milling in our AJA system to clean the sample surface before contact deposition. With Ar flow 4 sccm, pressure $P = 0.2$ mTorr, discharge voltage 40 V (for Ar, 28 V if using Xe), beam voltage 200 V, acceleration voltage 200 V, beam current 10 mA, tilt angle 22°, substrate rotation at 20 rpm and neutralized beam, we measure an etch rate of $\sim 3.2$ nm/min for Ge substrates. Frequent cooling after every 15–30 s of etching is required to avoid softening the top surface of the resist that destroys the device pattern. This is also true for Ar-rich recipes in ICP-RIE dry etchers. Redeposition of materials usually happens during ion milling, and the fence created by redeposition may have to be removed properly in some way when necessary.

### 2.2.6 Dielectric Growth by Atomic Layer Deposition and Rapid Thermal Annealing

From our measurements, it is found that $\varepsilon_{\mathrm{r}}$ and the density of charges trapped at the SiGe/oxide interface $D_{\mathrm{it}}$ are very sensitive to the ALD chamber conditioning, the growth temperature, and the post-growth annealing condition. In general, higher $\varepsilon_{\mathrm{r}}$ and lower $D_{\mathrm{it}}$ require proper chamber conditioning (several growth cycles with the same precursor to be used), possibly higher growth temperature, or high-temperature post-growth annealing. For oxide growth on Ge or SiGe wafers, since they will form an unstable thin $GeO_x$ layer at the surface shortly after exposure to air, proper acid cleaning may be necessary to reduce $D_{\mathrm{it}}$.

Furthermore, the hole density $p$ of SiGe 19-219 and 22-213 bare wafers without any oxide growth was also measured in van der Pauw (vdP) geometry [163] with In contacts placed at the corners. Comparing the data obtained in ungated devices with the data measured in gated devices at $V_{\mathrm{g}} = 0$, presented in Table. 2.1, we find that $p$ of ungated devices can be several times higher than in gated devices. But as described above, devices fabricated using higher ALD growth temperature or post-growth temperature have $p$ similar to the devices with no gates; in other words, high $T$ treatment can help to reduce $D_{\mathrm{it}}$.

**Table 2.1.** Hole density $p\,(10^{10}\,\mathrm{cm}^{-2})$ of Ge quantum well wafers at gate voltage $V_\mathrm{g} = 0$ after annealing or atomic-layer deposition at different temperatures. For samples with a gate, 40 nm $AlO_x$ is ALD grown at 300 °C, followed by thick Al gate thermal or e-beam evaporation. For samples with $AlO_x$ and post-annealing, oxide is ALD grown at 200 °C, followed by 350 °C annealing in Ar or $N_2/H_2$ atmosphere using our home-built annealing station. All the densities are estimated from quantum oscillations at high fields.

| wafer | w/o gate | w/gate* | w/gate 300 °C | oxi Ar 350 °C | oxi $N_2/H_2$ 350 °C |
|---|---|---|---|---|---|
| 19-219 | 16.15 | 2.34 | 1.48 | ** | ** |
| 19-220 | ··· | 3.60 | ··· | 12.84 | 5.08 |
| 22-213 | 8.78 | ··· | 4.11 | ··· | ··· |

*: By Dr. Ying Wang.

**: Not conducting after 200 °C $AlO_x$ ALD growth.

For all the samples fabricated until the past few months, we find that none of them appear to be conducting, except for 19-218 (undoped deep QW) and those in Table. 2.1. Recently, after we realized the importance of sample cleaning to contact/device quality [144] (see Section 2.2.1), all the new samples made from shallow QWs are conducting, while previous samples were fabricated using beakers and tweezers that had not undergone Piranha cleaning. Table. 2.2 shows the carrier density and mobility of the shallow QW devices fabricated with thorough cleaning before the 5 nm $AlO_x$ protective ALD layer growth.

For the samples in Table. 2.2, they are first thoroughly cleaned in clean beakers following the procedures described in Section 2.2.1 and immediately loaded into the ALD chamber for pumping. The ALD chamber has been stabilized at 300 °C and conditioned with a few layers of $AlO_x$ growth before sample loading. Right after loading the samples, we start with 3 cycles of $AlO_x$ growth with 60 s long wait of $H_2O$ pulse (compared to 8 s normal waiting time), to fully oxidize the precursor near the interface. Another 17 cycles of $AlO_x$ are deposited that end up with $\sim 2$ nm of $AlO_x$ at the interface. Then the samples are annealed in forming gas at 450 °C for 75 s at atmosphere pressure. Right after annealing, another 3 nm of $AlO_x$ is

grown on top to further protect the $AlO_x$/(Si)Ge interface. After contact liftoff, 25 nm more $AlO_x$ is grown as gate oxide.

**Table 2.2.** Carrier density $p$, transport mobility $\mu$ and quantum mobility $\mu_q$ of shallow Ge quantum well field effect transistors at zero gate voltage $V_g = 0$, with thorough sample cleaning before the 5 nm protective $AlO_x$ oxide growth at the very beginning. $d$ is the thickness of the SiGe top spacer.

| Wafer | 22-211 | 22-212 | 24-231 | 24-232 | 24-233 |
|---|---|---|---|---|---|
| $d$ (nm) | 20 | 100 | 7 | 10 | 5 |
| $p$ ($10^{11}$/cm$^2$) | 7.76 | 2.59 | 7.86 | 3.12 | 9.62 |
| $\mu$ ($10^5$ cm$^2$/(V $\cdot$ s)) | 2.37 | 13.4 | 0.011 | 0.066 | 0.006 |
| $\mu_q$ ($10^4$ cm$^2$/(V $\cdot$ s)) | 2.38 | 11.9 | – | – | – |

For wafers with similar structure and only different top spacer thickness $d$, for example, 24-231, 232, and 233, the carrier density at $V_g = 0$ is higher for smaller $d$. Furthermore, for these three undoped wafers, we measure high hole densities at zero $V_g$. This evidence indicates that there is a high density of donor-type trapped charges $N_d$ at the $AlO_x$/SiGe interface [164], which affects the total density more seriously when the trapped charges are closer to the QW. Scattering by these trapped charges also causes lowering of the mobility at small $d$. We see a similar trend for doped wafers 22-211 and 212: deeper QW has a lower carrier density and a higher mobility when samples are fabricated in parallel.

Comparing Tables. 2.1, 2.2 and the behavior of the insulating shallow QW devices without proper cleaning, we may conclude that the contaminants from the beakers, tweezers, resist residue, etc., might stay at the semiconductor/dielectric interface or even diffuse into (Si)Ge, which creates a very high density of acceptor-type trapped charges $N_A > 5 \times 10^{12}$/cm$^2$ at the interface and drags the chemical potential profile close to or even above $\varepsilon_F$. Thus, the hole density at $V_g = 0$ is lowered toward zero and requires a strong negative $V_g$ to possibly induce hole carriers again.

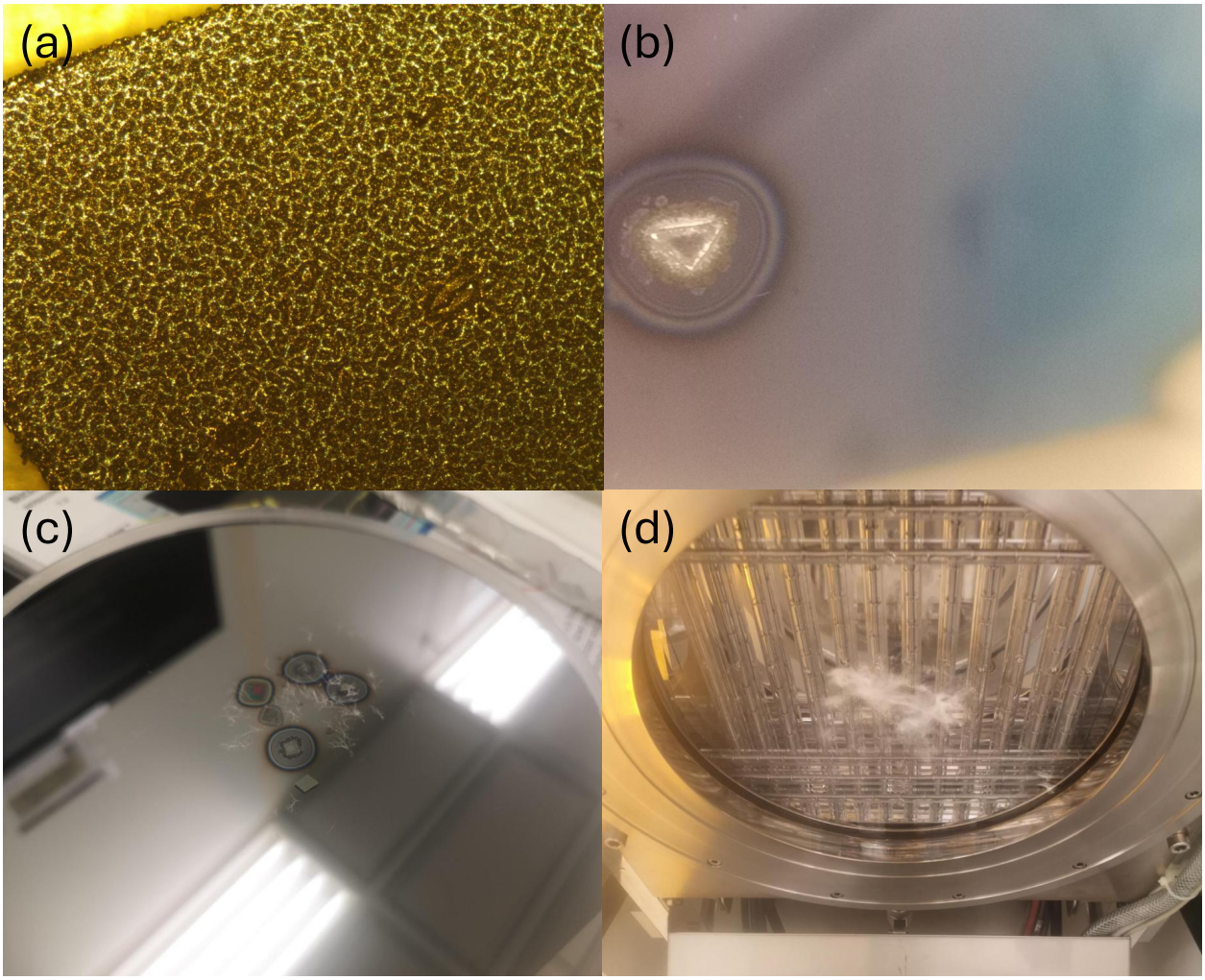


**Figure 2.12.** (a) An $i$-Ge wafer after 500 °C RTA for 30 s in an oxygen atmosphere, with (b) its remainder on the Si carrier wafer. Some loose white oxide fibers are left on (c) the Si carrier wafer and (d) the cover of the RTA equipment.

As a thin layer of $GeO_2$ by oxidation might help in improving the quality of Ge-based FETs [165], we also want to know if the quality of our Ge QW-based FETs can be improved similarly. The only difference in the fabrication process compared to those in Table. 2.2 is that the forming gas annealing after the first 2 nm of $AlO_x$ protection layer growth is replaced by annealing in oxygen. So far, we have tested two samples made from wafers 24-231 and 232 that are annealed in oxygen at atmospheric pressure at 450 °C for 75 s. Both of them are insulating up to $V_g = -10$ V. It indicates that a very high density of acceptor-type trapped charges $N_A$ are created by oxidation, or the top SiGe spacer has been fully oxidized. A clue

is that SiGe without an oxide protection layer becomes extremely rough after oxidation. The effect is more serious on the i-Ge wafers grown by the CZ method. A visible fume of oxide deposited on the carrier wafer is observed after oxidation, and the surface roughness of i-Ge wafers becomes $> 1\,\mu$m. Therefore, (Si)Ge epitaxial layers are denser than CZ Ge substrates but still require oxide protection to slow down the oxidation speed.

We also notice before that the conducting deep Ge QW wafers become insulating if they have been stored in air for over 1 to 2 years and if they are not cleaned in acid again or annealed at high temperature (in Ar, $Ar/H_2$, $N_2$, or $N_2/H_2$ atmosphere). It can possibly tell us that improper germanium oxide layers can create a high density of acceptor-type charges and deplete the carriers. Similarly, PEALD of $AlO_x$ or $SiO_x$ seems to create a similar effect and result in metallic or insulating samples. Further optimization of ALD oxide growth and RTA is ongoing to lower the interface charge density reproducibly.

### 2.2.7 Wire bonding

The last step before measurement is sample packaging. Careful handling is still required in case the samples get damaged.

For FET samples with top gates, avoiding gate leakage is crucial. For samples with Si or Ge substrates, the substrates are not as insulating as ALD dielectrics even at cryogenic temperatures. Ensuring that the substrates have no unwanted electrical connection to any chip carrier contact, including spatial separation or insulator (e.g., thin glass) separation, can reduce the leakage current at high gate voltages. Similarly, during gate pad wire bonding, high ultrasonic power can punch the wire through the thin dielectric layer to the substrate, which results in extra leakage currents. Usually, gate pads are deposited on top of dielectric layers and are as adhesive as on top of Si(/Ge) wafers. Au wires require lower ultrasonic power than Al wires to solidly bond to the gate pads without peeling them off.

In our FET samples, instead of making vias to contact pads, we directly punch through the thin dielectric layer with high ultrasonic power to connect to the metal contact pads. From our tests, we cannot find a power setting for Au wires that works for this method. Aluminum wires are used for contact wire bonding in a calibrated power range with close to

100% yield. Since high ultrasonic power is required for contact bonding, the maintenance of the wire bonding pins is important to prevent poor adhesion, cratering, peeling, or chipping.

Microscopic FETs can easily burn due to electrostatic discharge. In addition to wearing anti-static grounding wristbands during wire bonding and sample mounting, extra precautions can be applied to further ensure sample safety. The following procedures have been tested with high yield.

1. Remove clothing that is subject to severe electrostatic discharge or wear anti-static lab coats. Wear anti-static grounding wristbands before sample mounting.

2. Ground all contacts on the chip carrier to the chassis ground of the wire bonder before bonding wires to the samples. If they cannot be grounded directly through a holder, we can temporarily bond some wire between all contacts.

3. For each sample that is electrically disconnected from the others, start with at least one contact bonding to ground the contacts/channels first.

4. After the channels are grounded, the gate pads can be safely bonded. The channels and gates are guaranteed to be on the same electric potential when the gate pads are bonded.

5. To avoid burning during sample transfer, make sure that there is at least one wire between the gate and the channel for each sample as a short after completing all the wiring.

6. Ground ourselves and the sample holder on the measurement equipment before mounting the samples. Only remove the shorts after the samples have been mounted on well-grounded equipment.

Similar procedures can be applied for any charge-sensitive samples like quantum dots or van der Waals materials.

From our tests, we can safely contact $p^{++}$-Ge wafers or $\lesssim 10\,\mathrm{nm}$ thin films of hard materials, e.g., Ir(Ge), NbTiN, or MoRe grown on Si or Ge substrates, by direct wire bonding. Extra bonding pads with thick metals are not always necessary for testing. For example,

to measure the resistivity of a square/rectangular piece of thin film, we can wire bond at the very corners directly. By measuring the horizontal and vertical longitudinal resistivity $\rho_{xx}$, $\rho_{yy}$ using low-frequency lock-in measurements, the sheet resistivity $\rho_{\square}$ can be calculated using the vdP equation [163]:

$$e^{-\pi\frac{\rho_{xx}}{\rho_{\square}}} + e^{-\pi\frac{\rho_{yy}}{\rho_{\square}}} = 1.$$

Direct bonding cannot be applied for capped QWs. A quick conventional way to contact Ge QWs is to scribe at the very corners of a square piece of wafer and solder indium contacts at the scratches. Indium contacts to GaAs QWs can be made similarly with additional annealing (without scribing). Indium puddles are too thick and soft for wire bonding. Manual soldering is thus needed, or wires can be connected by mechanically pressing them between indium contacts and small pieces of indium.

# 3. CHARACTERIZATION OF SUPERCONDUCTING GERMANIDE AND GERMANOSILICIDE FILMS OF PD, PT, RH, AND IR FORMED BY SOLID-PHASE EPITAXY[1]

## 3.1 Introduction

The development of superconductor–semiconductor hybrid technology based on group IV semiconductors [20]–[30] is facilitated by advances in the growth of compressively strained Ge on Si (cs-GoS) heterostructures via relaxed SiGe buffer, where the mobility of two-dimensional hole gases in Ge quantum wells can exceed $10^6\,\mathrm{cm}^2/(\mathrm{V}\cdot\mathrm{s})$ [31]–[35]. Aluminum forms low-resistance contacts with strained Ge due to Fermi-level pinning close to the top of the valence band [20], [21], and superconductivity can be induced in Ge QWs by the proximity effect, either in direct Al/Ge contacts [22]–[24], [29] or when Al is separated from Ge by a thin, semitransparent SiGe barrier [26], [27]. The diffusion of Al into (Si)Ge is not self-limiting, which makes the transparency of annealed Al contacts a strong function of post-deposition processing. The sensitivity of Al contacts to thermal treatment, their low superconducting critical temperature $T_\mathrm{c} < 1.5\,\mathrm{K}$, and low out-of-plane critical field $B_{\mathrm{c},\perp} \sim 10\,\mathrm{mT}$ have stimulated the development of alternative contacts.

To induce a hard superconducting gap in Ge, an ideal superconducting contact should have a low Schottky barrier and form a sharp, transparent interface with Ge. In CMOS technology, mono- and polycrystalline silicides are used to form low-resistance contacts between metal interconnects and Si/Ge channels [166], in which case, contacts are formed via a solid-phase reaction between a metal and Si/Ge. Although a number of silicides and germanides are superconducting at low temperatures [167]–[177], many compounds with high $T_\mathrm{c} > 4$ K, such as $NbGe_2$ [170], [171], [174], form at very high temperatures beyond the $\sim 500\,^\circ\mathrm{C}$ thermal budget of strained Ge/SiGe heterostructures [178]. Some platinum group metals form silicides and germanides at low temperatures ($< 500\,^\circ\mathrm{C}$), and the formation of superconducting PtGe ($T_\mathrm{c} = 0.4$ K) [167]–[169], [172] and RhGe ($T_\mathrm{c} = 0.96$–$1.7$ K) [167]–[169], [172], [173] has been demonstrated. Notably, polycrystalline platinum germanosilicide

[1]↑Adapted and expanded from [1] (CC-BY 4.0). Supplemental material is integrated into the main text.

(PtSiGe) contacts have been shown to induce a hard superconducting gap in shallow Ge QWs with high transparency $\tau \sim 0.95$ [25], [28]. A high out-of-plane upper critical magnetic field $B_{c2,\perp} = 0.9\,\mathrm{T}$ has been measured in hybrid devices with small PtSiGe leads [30], substantially higher than $B_{c2,\perp} \sim 0.1\,\mathrm{T}$ in large contacts [25], [30]. Another transition metal, Ta, has recently been found to form a solid solution of $Ta_5Ge_3$ and $TaGe_2$ when grown via molecular beam epitaxy (MBE) on Ge substrates at $T = 400\,^{\circ}\mathrm{C}$ [177]. These films exhibit $T_c \sim 1.8$–$2$ K, $B_{c2,\perp} \sim 1.88\,\mathrm{T}$, and $B_{c2,\parallel} \sim 5.1$ T, in agreement with previous studies of tantalum germanide [170], [179].

Within the platinum group germanides, Ir-based compounds show the highest $T_c$: IrGe ($T_c = 4.7$–$5.3\,\mathrm{K}$, $B_{c1}(0) = 13.3\,\mathrm{mT}$, $B_{c2}(0) = 0.82$–$1.13\,\mathrm{T}$) [167]–[169], [172], [173], [175], $Ir_3Ge_7$ ($T_c = 0.87\,\mathrm{K}$) [168], [169], and $IrGe_4$ ($T_c = 1.22\,\mathrm{K}$, $B_{c2} = 11.5$–$22.5\,\mathrm{mT}$) [176]. Based on results from specific heat and muon spin relaxation experiments, an enhanced $T_c$ of IrGe is attributed to the presence of low-lying phonons [173], [175]. Although single IrGe crystals are grown at $T = 700\,^{\circ}\mathrm{C}$ [173], there is some evidence that the onset of solid-phase reaction between Ir and Ge begins at $400\,^{\circ}\mathrm{C}$ [180]. While IrGe shows an enhanced $T_c$, IrSi is not known to be a superconductor down to mK temperatures. The superconducting properties of IrSiGe have not been investigated.

In this chapter, we compare the superconducting properties of thin films formed by solid-phase epitaxy of Pd, Pt, Rh, and Ir on Ge(001) or relaxed $Si_{0.15}Ge_{0.85}$ layers grown on Si(001) and present a systematic study of Ir-based films. We show that within the temperature range of 400–500 °C (within the thermal budget of strained Ge/SiGe heterostructures), self-limiting polycrystalline films of IrGe and IrSiGe are formed by solid-phase epitaxy. For optimally grown IrGe (IrSiGe) films, we report $T_c \sim 3.4\,\mathrm{K}$ ($2.6\,\mathrm{K}$) and $B_{c2,\perp} \sim 3.4\,\mathrm{T}$ ($2.8\,\mathrm{T}$), the latter being significantly larger than $B_c = 0.82$–$1.13\,\mathrm{T}$ reported for bulk IrGe [173], [175]. High-resolution scanning transmission electron microscopy (HRSTEM) of optimally annealed Ir/Ge films reveals the formation of IrGe microcrystals with sharp boundaries between IrGe and Ge.

## 3.2 Results

### 3.2.1 Superconducting Transport Properties

In this study, we use two types of substrates: undoped Ge(001) single-crystal wafers ($i$-Ge) and strain-relaxed $Si_{0.15}Ge_{0.85}$ thick films capped with 2 nm of Ge, grown epitaxially on strain-relief buffers on Si(001) wafers (SiGe). All heterostructures are grown by reduced pressure chemical vapor deposition (RP-CVD) [33], [34]. Prior to metal deposition, the wafers are cleaned using acetone, isopropanol, and deionized water, followed by dipping in diluted HCl and HF to remove native oxides. We expect that most of the 2 nm Ge capping layer on SiGe is naturally oxidized and is removed during the last step of acid treatment. Metal films are deposited either by DC sputtering (Ir) or electron-beam evaporation (Pt, Pd, and Rh) onto substrates held at room temperature in ultra-high vacuum deposition systems with a base pressure of $\sim 10^{-9}$ Torr. After metal deposition, the samples are annealed in a custom-built rapid thermal annealer (RTA) with precise temperature control in an Ar atmosphere. Transport measurements are carried out in either a dilution refrigerator or a $^3$He cryostat using standard four-probe low-frequency lock-in techniques.

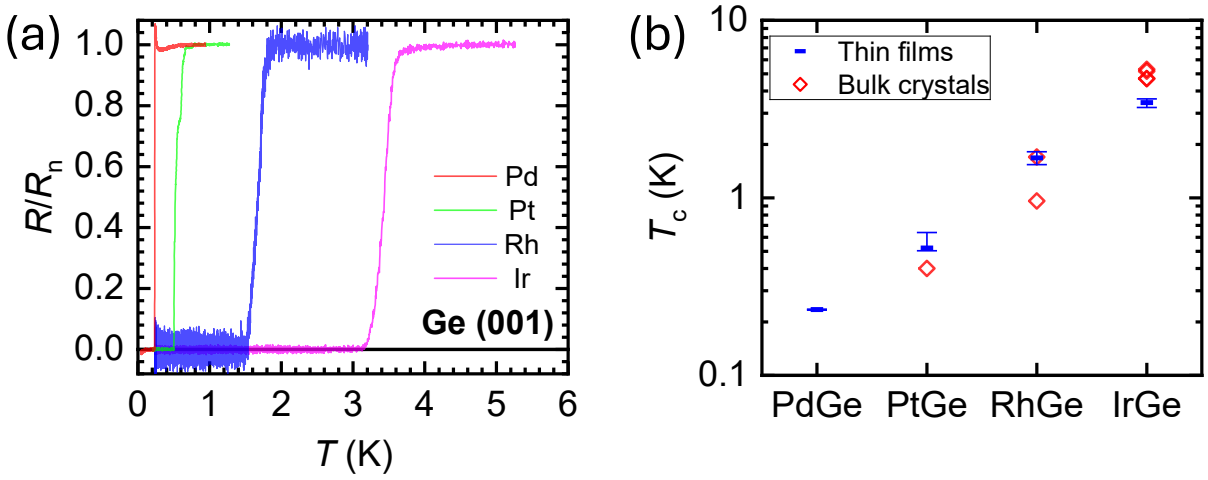


**Figure 3.1.** (a) Temperature dependence of the normalized resistance $R/R_n$ for optimally annealed 10 nm Pd, Pt, Rh, and Ir films deposited on Ge(001) substrates. (b) $T_c$ for thin films in this study (blue) are compared with $T_c$ for bulk crystals (red) from Refs. [167]–[169], [172], [173], [175]. The vertical bars indicate the width of the transition region defined as $0.05 < R/R_n < 0.95$. (Reproduced from [1] under CC-BY 4.0.)

**Table 3.1.** Properties of optimally annealed MGe (in Fig. 3.1) and MSiGe films, where M = Pd, Pt, Rh, or Ir, $d^{\mathrm{M}}$ is the metal thickness, $T_{\mathrm{ann}}$ is the annealing temperature, and $t_{\mathrm{ann}}$ is the annealing time. Superconducting transition widths for critical temperature $\Delta T_{\mathrm{c}} = T_{\mathrm{c}}^{95} - T_{\mathrm{c}}^{5}$ and for out-of-plane critical field $\Delta B_{\mathrm{c2},\perp} = B_{\mathrm{c2},\perp}^{95} - B_{\mathrm{c2},\perp}^{5}$, where $T_{\mathrm{c}}^{XX}$ and $B_{\mathrm{c2},\perp}^{XX}$ refer to temperatures and out-of-plane fields where resistance reaches $XX\%$ of its normal value. $B_{\mathrm{c2},\perp}(0)$ is the critical field extrapolated to $T = 0$. (Reproduced from [1] under CC-BY 4.0.)

| Substrate | Ge(001) | | | | $Si_{0.15}Ge_{0.85}$ | | | |
|---|---|---|---|---|---|---|---|---|
| M | Pd | Pt | Rh | Ir | Pd | Pt | Rh | Ir |
| $d^{\mathrm{M}}$ (nm) | 10 | 10 | 10 | 10 | 20 | 20 | 10 | 10 |
| $T_{\mathrm{ann}}$ (°C) | 400 | 400 | 500 | 450 | 400 | 350 | 475 | 475 |
| $t_{\mathrm{ann}}$ (min) | 10 | 5 | 5 | 30 | 10 | 5 | 5 | 20 |
| $T_{\mathrm{c}}$ (K) | 0.235 | 0.522 | 1.68 | 3.44 | 0.299 | 0.585 | 1.28 | 2.56 |
| $\Delta T_{\mathrm{c}}$ (K) | 0.002 | 0.134 | 0.28 | 0.38 | 0.01 | 0.02 | 0.22 | 0.31 |
| $B_{\mathrm{c2},\perp}(0)$ (T) | 0.007 | 0.11 | 1.46 | 3.43 | ··· | 0.18 | 1.37 | 2.84 |
| $\Delta B_{\mathrm{c2},\perp}$ (T)[a)] | 0.001 | 0.06 | 0.30 | 1.38 | ··· | 0.12 | 0.15 | 0.73 |

[a)] Measured at $T = 0.25$ K for RhGe, IrGe, and IrSiGe films and $T \sim 50$ mK for all other films.

In Fig. 3.1(a), the temperature dependence of the normalized resistance is plotted for Pd, Pt, Rh, and Ir germanides formed under the optimal thermal treatment conditions of 10 nm films. The superconducting transition temperatures $T_{\mathrm{c}}$, defined here as the midpoint of the transition where the resistance drops by a factor of two relative to the normal resistance ($R = 0.5R_{\mathrm{n}}$), follow the trend of bulk germanides.

Previous studies of diffusion kinetics using x-ray diffraction (XRD) and TEM techniques indicate that the solid-phase reaction between Pd and Ge initially proceeds via the diffusion-controlled growth of $Pd_2Ge$, which is converted into PdGe at $T > 150\,^{\circ}$C; PdGe phase remains stable up to its melting point $T \approx 740\,^{\circ}$C [180]–[191]. Thus, we expect that the PdGe phase dominates in our samples for annealing at $T \geqslant 300\,^{\circ}$C, and the measured $T_{\mathrm{c}} = 0.24$ K reflects the superconducting properties of PdGe films. For annealed Pt/Ge films,

the measured $T_c = 0.5\,\mathrm{K}$ is higher than the reported $T_c = 0.4\,\mathrm{K}$ for bulk PtGe [167]. Earlier studies using XRD indicate the formation of the PtGe phase when films are annealed in the 380–440 °C temperature range [178]. For Rh/Ge, we measure $T_c = 1.68\,\mathrm{K}$, close to the bulk RhGe $T_c \sim 1.7\,\mathrm{K}$ [173]. $Rh_5Ge_3$ orthorhombic phase has higher $T_c = 2.12\,\mathrm{K}$ [167]–[169], [172], but this phase has not been found in previous studies of the solid-phase reaction of Rh/Ge thin films [178], [180], [181]. $RhGe_4$ phase also has higher $T_c = 2.55\,\mathrm{K}$, but this phase is only stabilized under high pressure [176] and we do not expect it to be formed in our experiments. For Ir/Ge, the measured $T_c = 3.44\,\mathrm{K}$ is slightly less than the 4.7–5.3 K reported for stoichiometric IrGe crystals [167], [173], but higher than that for $Ir_3Ge_7$ ($T_c = 0.87\,\mathrm{K}$ [168]) or $IrGe_4$ ($T_c = 1.22\,\mathrm{K}$ [176]) phases.

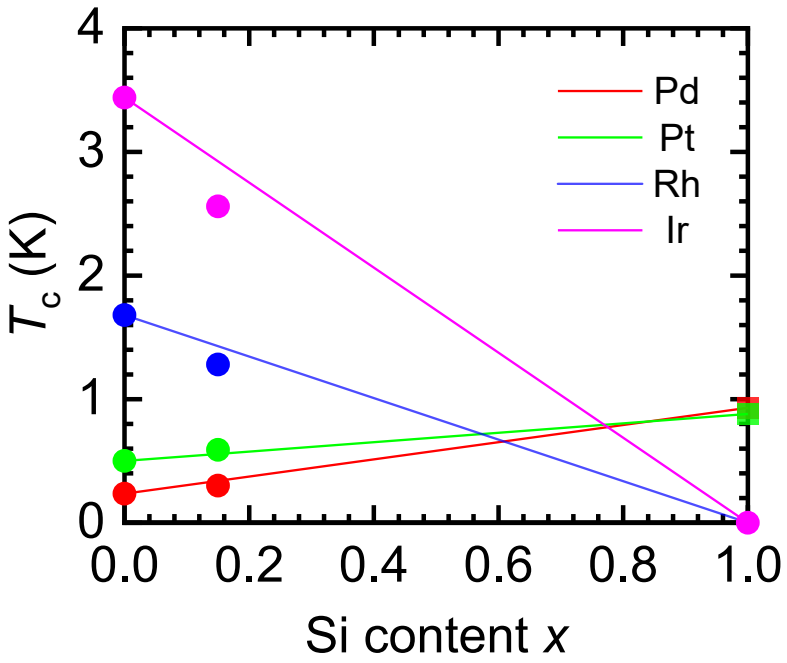


**Figure 3.2.** $T_c$ for pure MSi are shown by square symbols [167]–[169], [172], where M = Pd, Pt, Rh, or Ir. Measured $T_c$ for MGe, MSi, and $MSi_{0.15}Ge_{0.85}$ are plotted as dots. These values are close to the values linearly extrapolated between $T_c$ of MSi and MGe. (Reproduced from the supplemental material of [1] under CC-BY 4.0.)

The superconducting properties of Pd, Pt, Rh, and Ir germanosilicides in Table. 3.2 are found to reflect the composition of the $Si_xGe_{1-x}$ substrate. For films grown on $Si_{0.15}Ge_{0.85}$

substrates, we measure $T_c = 0.30\,\mathrm{K}$ for Pd/SiGe, $T_c = 0.59\,\mathrm{K}$ for Pt/SiGe, $T_c = 1.28\,\mathrm{K}$ for Rh/SiGe, and $T_c = 2.56\,\mathrm{K}$ for Ir/SiGe. These values are close to $T_c^{\mathrm{MSiGe}} \approx 0.15 \times T_c^{\mathrm{MSi}} + 0.85 \times T_c^{\mathrm{MGe}}$ (M = Pd, Pt, Rh, or Ir) (Fig. 3.2). The observation of a weighted $T_c$ suggests the formation of a proportional mixture of germanides and silicides.

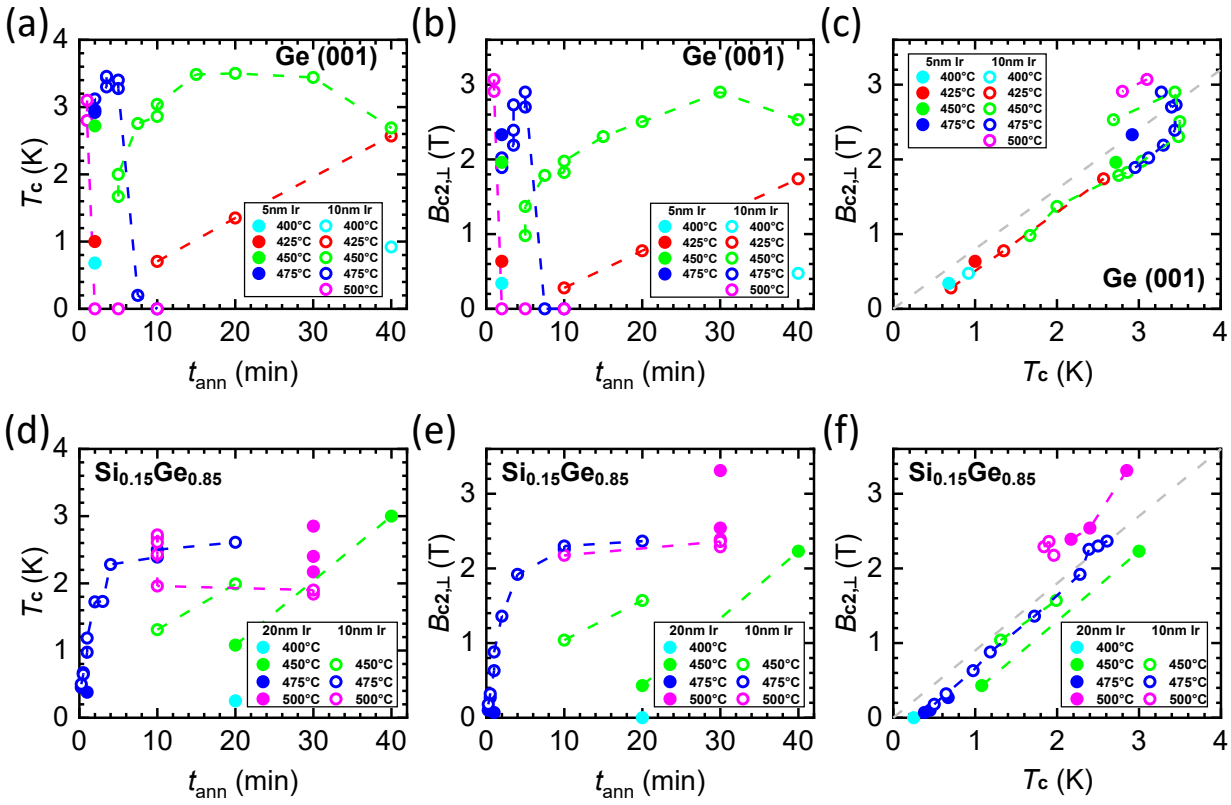


**Figure 3.3.** (a,b,d,e) The critical temperature $T_c$ and the out-of-plane critical field $B_{c2,\perp}$ are plotted as a function of annealing time $t_{\mathrm{ann}}$ for $i$-Ge and SiGe substrates, showing their dependence on the Ir film thickness and annealing temperature. $T_c < 0.25\,\mathrm{K}$ is plotted as $T_c = 0$. The filled (open) circles correspond to different Ir thicknesses indicated in the legends, and the colors differentiate different annealing temperatures. (c,f) $B_{c2,\perp}$ is re-plotted as a function of $T_c$. (Reproduced from [1] under CC-BY 4.0.)

The dependence of $T_c$ and $B_{c2}$ (defined at a midpoint of resistance drop, $R(B_{c2}) = 0.5R_n$) of Ir/Ge and Ir/SiGe films on Ir thickness, annealing time $t_{\mathrm{ann}}$, and annealing temperature is summarized in Fig. 3.3. The initial increase in $T_c$ and $B_{c2,\perp}$ with $t_{\mathrm{ann}}$ is attributed to the finite barrier for Ir diffusion into $i$-Ge and SiGe substrates. The corresponding activation energy can be found by analyzing the time $t_{\mathrm{ann}}^0$ needed to anneal a film to reach the same $T_c$

for different annealing temperatures $T_{\mathrm{ann}}$. The $t^0_{\mathrm{ann}}(T_{\mathrm{ann}})$ dependence for $T_{\mathrm{c}} \sim (2.8 \pm 0.2)\,\mathrm{K}$ is found to be exponential, and from the Arrhenius plot we extract the activation energy $E_{\mathrm{a}} \approx 2.7\,\mathrm{eV}$ assuming $t^0_{\mathrm{ann}} \propto 1/D$ and a diffusion coefficient $D \propto \exp(-E_{\mathrm{a}}/k_{\mathrm{B}}T_{\mathrm{ann}})$, where $k_{\mathrm{B}}$ is the Boltzmann constant (Fig. 3.4). Here, we assume that partially formed germanides are morphologically similar and neglect the reduction in $T_{\mathrm{c}}$ due to the reverse proximity effect in the presence of metallic Ir in under-annealed samples. The samples with thinner Ir films require shorter annealing times to reach the same $T_{\mathrm{c}}$.

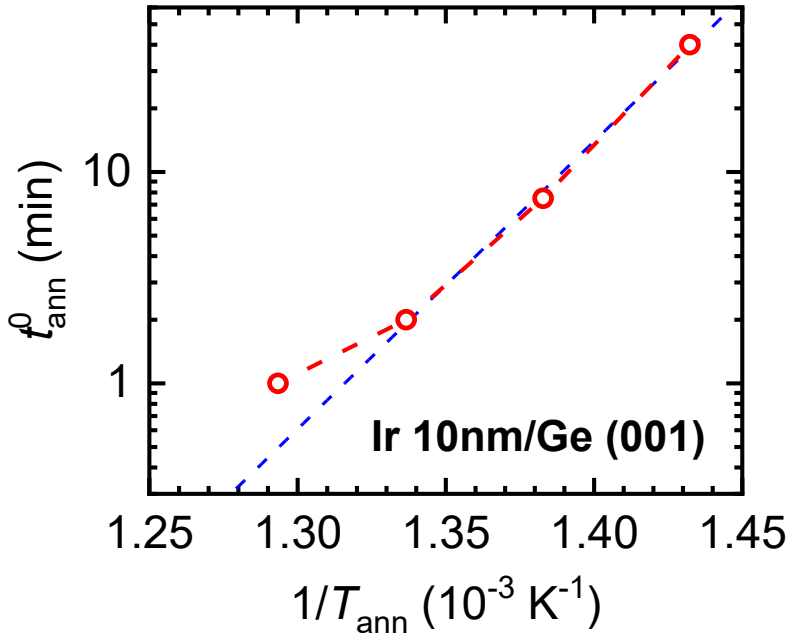


**Figure 3.4.** The Arrhenius plot of $t^0_{\mathrm{ann}}$ vs. $1/T_{\mathrm{ann}}$ for Ir 10 nm/$i$-Ge films. $t^0_{\mathrm{ann}}$ is defined as the annealing time required for the film to have a critical temperature $T_{\mathrm{c}} \sim (2.8 \pm 0.2)\,\mathrm{K}$. The dashed line corresponds to the activation energy 2.7 eV. (Reproduced from the supplemental material of [1] under CC-BY 4.0.)

For Ir on $i$-Ge samples, after an initial increase from $T_{\mathrm{c}} \sim 0.2$ K for Ir films with annealing time, $T_{\mathrm{c}}$ reaches a maximum and then decreases with further annealing. A sharp decrease in $T_{\mathrm{c}}$ is observed for samples annealed at $T \geqslant 475\,^{\circ}\mathrm{C}$, where an extra minute of annealing results in a drop in $T_{\mathrm{c}}$ from 3.2 K to $< 0.25\,\mathrm{K}$. For IrGe films, the optimal annealing temperature is

found to be 450 °C; this $T_{\mathrm{ann}}$ provides a large $t_{\mathrm{ann}} \approx 12$–30 min window to form films with the highest $T_{\mathrm{c}}$. As we will discuss below, optimally annealed films consist of IrGe microcrystals.

For Ir on SiGe, no significant decrease in $T_{\mathrm{c}}$ for long annealing times has been observed. We speculate that the reduction in $T_{\mathrm{c}}$ in over-annealed Ir/Ge samples is due to the formation of a competing semiconducting $Ir_4Ge_5$ phase with lower formation energy [192]–[194]. This explanation is consistent with the observed higher stability of IrSiGe films, since IrSi is expected to have a lower formation energy than the competing $Ir_3Si_4$ and $Ir_3Si_5$ metallic phases [192]–[194]. The formation of a semi-insulating phase in over-annealed Ir/Ge samples is also consistent with a sharp increase in resistivity and a semiconducting $T$-dependence (slight resistance increase below 1 K) (Table. 3.2 and Fig. 3.5).

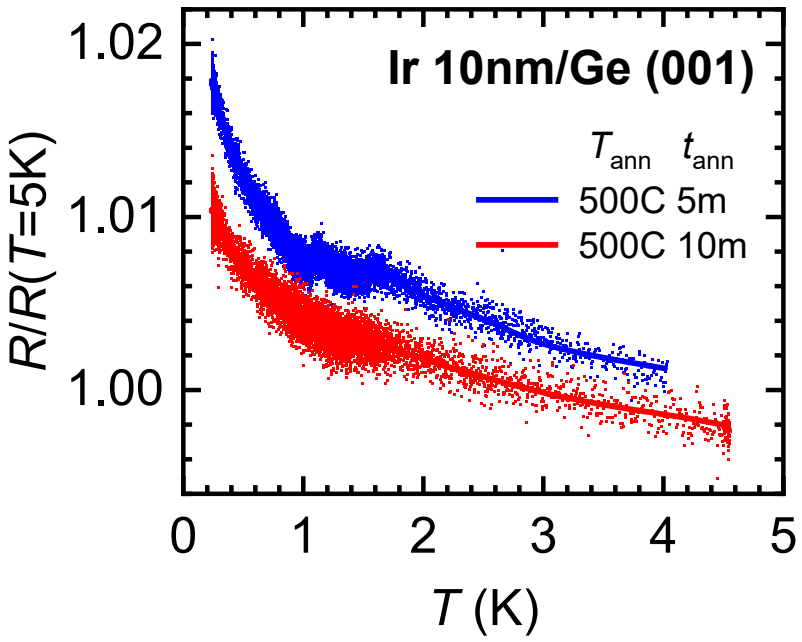


**Figure 3.5.** Temperature dependence of normalized resistance in over-annealed Ir/*i*-Ge films shows a negative trend at low temperatures, indicating semiconducting properties of the film. (Reproduced from the supplemental material of [1] under CC-BY 4.0.)

**Table 3.2.** Parameters of IrGe (top) and IrSiGe (bottom) films formed using different annealing conditions. Most parameters are defined in Table. 3.1. Sheet resistivity $\rho_\square$ is measured in van der Pauw geometry. Resistivity $\rho$ and electron density $n$ are calculated assuming that all Ir reacts with Ge to form IrGe with the thickness 2.37 $d^{\mathrm{Ir}}$. (Reproduced from the supplemental material of [1] under CC-BY 4.0.)

| $d^{\mathrm{Ir}}$ | $T_{\mathrm{ann}}$ | $t_{\mathrm{ann}}$ | $T_{\mathrm{c}}$ | $\Delta T_{\mathrm{c}}$ | $B_{\mathrm{c2},\perp}$ | $\Delta B_{\mathrm{c2},\perp}$ | $\rho_\square$ | $\rho$ | $n$ |
|---|---|---|---|---|---|---|---|---|---|
| (nm) | (°C) | (min) | (K) | (K) | (T) | (T) | ($\Omega/\square$) | ($\mu\Omega\cdot$m) | $10^{27}$m$^{-3}$ |
| ***i*-Ge** | 400 | 2 | 0.68 | 0.09 | 0.34 | 0.16 | 136 | – | – |
| 5 | 425 | 2 | 1.00 | 0.08 | 0.64 | 0.17 | 134 | – | – |
| | 450 | 2 | 2.72 | 0.14 | 1.96 | 0.33 | 117 | 1.39 | – |
| | 475 | 2 | 2.92 | 0.16 | 2.33 | 0.46 | 115 | 1.36 | – |
| 10 | 350 | 40 | 0.39 | 0.04 | 0.12 | 0.11 | 38.4 | – | – |
| | 375 | 40 | 0.35 | 0.02 | 0.10 | 0.02 | 40.0 | – | – |
| | 400 | 40 | 0.92 | 0.07 | 0.48 | 0.10 | 51.3 | – | – |
| | 450 | 30[a)] | 3.44 | 0.31 | 2.90 | 1.39 | 209 | 4.95 | 1.88 |
| | 475 | 3.5 | 3.30 | 0.23 | 2.19 | 0.58 | 44.5 | 1.05 | 13.9 |
| | 475 | 3.5 | 3.44 | 0.19 | 2.39 | 0.76 | 52.0 | 1.23 | – |
| | 500 | 1 | 3.10 | 0.84 | 3.07 | 2.10 | 217 | 5.14 | – |
| | 500 | 2[b)] | <0.25 | – | – | – | 430 | – | – |
| **SiGe** | 450 | 20 | 1.99 | 0.23 | 1.57 | 0.45 | 64.9 | 1.54 | – |
| 10 | 475 | 10 | 2.50 | 0.21 | 2.30 | 0.65 | 59.5 | 1.41 | – |
| | 475 | 20[a)] | 2.61 | 0.32 | 2.37 | 0.76 | 64.2 | 1.52 | – |

[a)] These conditions are used in the main text analysis.

[b)] For this annealing condition, there is an onset of a broad transition with $T_{\mathrm{c}}^{95} = 1.00\,\mathrm{K}$ and $B_{\mathrm{c2},\perp}^{95} = 2.71\,\mathrm{T}$.

The critical field $B_{\mathrm{c2},\perp}$, plotted in Figs. 3.3(b) and 3.3(e), evolves similarly to $T_{\mathrm{c}}$ as a function of Ir thickness, annealing time, and annealing temperature. This similarity is

emphasized by an almost linear dependence $B_{c2,\perp} \propto T_c$, shown in Figs. 3.3(c) and 3.3(f), where $B_{c2,\perp}$ is plotted as a function of $T_c$ for all devices and annealing conditions. The highest $B_{c2,\perp} = 3.07\,\mathrm{T}$ measured in Ir/Ge and $B_{c2,\perp} = 3.31\,\mathrm{T}$ measured in Ir/SiGe films are significantly higher than the $B_{c2,\perp} = 0.82$–$1.13\,\mathrm{T}$ reported for bulk IrGe crystals [173], [175].

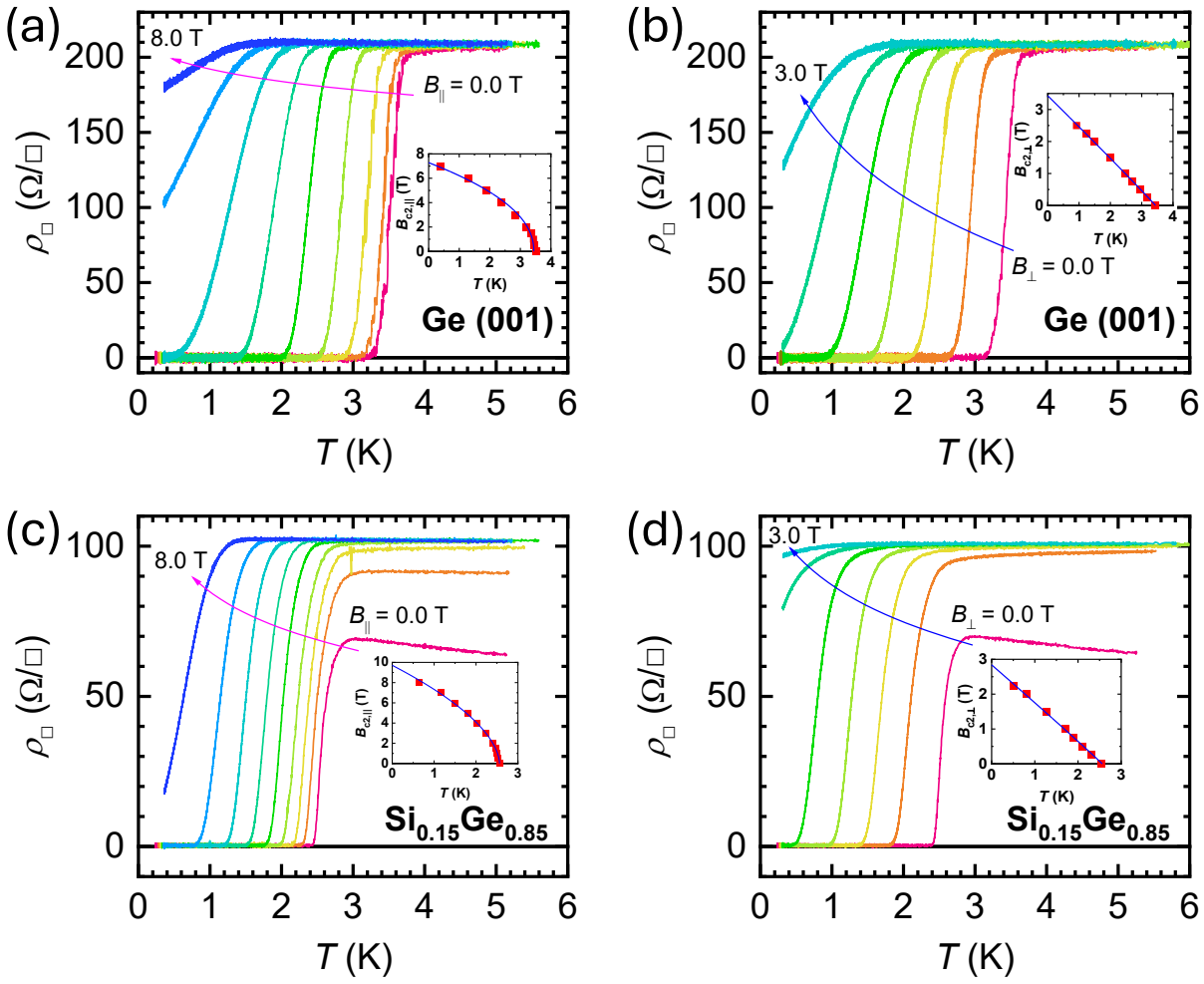


**Figure 3.6.** The change in resistivity as a function of temperature is plotted for various (a,c) in-plane $B_\parallel$ and (b,d) out-of-plane $B_\perp$ magnetic fields for the optimally annealed (a,b) Ir/$i$-Ge and (c,d) Ir/SiGe films. The insets show the temperature dependence of $B_{c2}$, and the blue lines represent fits using Eq. (3.1). (Reproduced from [1] under CC-BY 4.0.)

**Table 3.3.** $T_c$ is an experimental value for the films studied in Fig. 3.6, while $B_{c2}$ and $\alpha$ are extracted from the fits to Eq. (3.1). $B_P$ is an estimated Pauli limit as discussed in the text. The superconducting coherence length $\xi(0)$ and effective film thickness $d_{eff}$ are calculated from measured in-plane (IP) and out-of-plane (OOP) critical fields $B_{c2,\perp}(T) = \Phi_0/(2\pi\xi^2)$ and $B_{c2,\parallel}(T) \approx \sqrt{3}\Phi_0/(\pi\xi d_{eff})$. The Ginzburg–Landau coherence length $\xi_0$ and mean free path $l$ are calculated using $\xi(0) = \sqrt{\xi_0 l}$ and $l = \hbar\sqrt[3]{3\pi^2}n^{2/3}/(e^2\rho)$, where $n$ is the carrier density, $\rho$ is the three-dimensional resistivity, and $\xi(0)$ is $\xi$ at the lowest $T$. (Reproduced from [1] under CC-BY 4.0.)

| | Ir/Ge | | Ir/SiGe | |
|---|---|---|---|---|
| | IP | OOP | IP | OOP |
| $T_c$ (K) | 3.44 | | 2.56 | |
| $B_{c2}(0)$ (T) | 7.28 | 3.43 | 9.71 | 2.84 |
| $\alpha$ | 0.46 | 0.97 | 0.57 | 0.98 |
| $B_P$ (T) | 8.3 | | 6.2 | |
| $\xi(0)$ (nm) | 9.8 | | 10.8 | |
| $d_{eff}$ (nm) | 16.0 | | 10.9 | |
| $l$ (nm) | 1.7 | | ... | |
| $\xi_0$ (nm) | 56.5 | | ... | |

In Fig. 3.6, the temperature dependence of resistivity is plotted for different in-plane ($B_\parallel$) and out-of-plane ($B_\perp$) magnetic fields. In the insets, the temperature dependencies of $B_{c2,\perp}$ and $B_{c2,\parallel}$ are fitted to

$$B_{c2}(T) = B_{c2}(0)\left(1 - \frac{T}{T_c}\right)^{\alpha}, \tag{3.1}$$

where $\alpha$ and $B_{c2}(0)$ are the fitting parameters summarized in Table. 3.3. For the out-of-plane field $\alpha \approx 1$, while for the in-plane field $\alpha \approx 0.5$, confirming the two-dimensional nature of IrGe and IrSiGe films with $d_{eff} \lesssim 1.8\xi$. The temperature dependence of the critical fields, $B_{c2,\perp}(T) = \Phi_0/(2\pi\xi^2)$ and $B_{c2,\parallel}(T) \approx \sqrt{3}\Phi_0/(\pi\xi d_{eff})$, originates from the temperature dependence of the coherence length, $\xi(T) \approx \xi(0)/\sqrt{1 - T/T_c}$, where in a dirty superconductor $\xi(0) = \sqrt{\xi_0 l}$ is a geometrical average of a Ginzburg–Landau coherence length

$\xi_0$ and a mean free path $l$, $\Phi_0 = h/2e$ is the magnetic flux quantum [195]. The mean free path, $l = \hbar\sqrt[3]{3\pi^2}n^{2/3}/(e^2\rho)$, is calculated using the resistivity $\rho$ and electron density $n$ measured in the normal state just above $T_c$. The ratio $\xi_0/l = 33.2$ indicates dirty-limit superconductivity in IrGe. We note that the critical in-plane field is comparable to (IrGe), or exceeds (IrSiGe), the Pauli limit $B_P = \Delta_0/(\sqrt{2}\mu_B)$, where $\Delta_0 \approx 2.3k_BT_c$ is the zero-temperature superconducting gap for Ir(Si)Ge and $\mu_B$ is the Bohr magneton, indicating strong spin–orbit interactions [196]. The high $B_{c2,\perp}$ values, $B_{c2,\perp}(\mathrm{IrGe}) = 3.43\,\mathrm{T}$ and $B_{c2,\perp}(\mathrm{IrSiGe}) = 2.84\,\mathrm{T}$, significantly exceed the 1.13 T reported in bulk IrGe [175]. This enhancement can be attributed to the microcrystalline nature of the films [197]. These high $B_{c2,\perp}$ values could be useful for studying the interplay between superconductivity and quantum Hall states in high-mobility Ge two-dimensional hole gases.

### 3.2.2 Structural Analysis of Superconducting Ir/*i*-Ge films

The high-resolution scanning transmission electron microscopy (STEM) analysis of a 10 nm Ir/*i*-Ge film annealed at 475 °C for 3.5 min ($T_c \sim 3.4\,\mathrm{K}$) is presented in Figs. 3.7 and 3.8. The low-resolution image Fig. 3.7(a) shows the formation of a uniform film with a thickness of $d = (24 \pm 3)\,\mathrm{nm}$. The density of IrGe, $13.10\,\mathrm{g/cm^3}$, can be calculated from its structural parameters [173], [175]. Assuming that all Ir reacts with Ge to form the IrGe phase, 10 nm of Ir should react with 16 nm of Ge to form 23.7 nm of IrGe. This value is in excellent agreement with the film thickness $d$ obtained from the wide-area STEM image Fig. 3.7(a), suggesting that most Ir reacts with Ge to form IrGe, and close to the effective thickness $d_{\mathrm{eff}}$ calculated in Table. 3.3.

This conclusion is corroborated by cross-sectional aberration-corrected high-angle annular dark-field scanning transmission electron microscopy (HAADF-STEM) images, which show the formation of IrGe microcrystals with lateral sizes of $> 10\,\mathrm{nm}$ throughout the thickness of the film. In Figs. 3.7(b) and 3.7(c), an IrGe/Ge boundary is shown at two slightly different angles, highlighting the crystalline structure of an IrGe crystal and the surrounding Ge matrix. The boundary is sharp, with a negligibly small concentration of Ir in Ge, as evidenced by the energy-dispersive x-ray spectroscopy (EDX) analysis of Ir and Ge distribution across

the boundary (Figs. 3.7(d) and 3.7(e)). Note that the STEM specimen is $\lesssim 100\,\text{nm}$ thick, a few times larger than the average IrGe grain size. Unlike STEM, which probes only a few nanometers from the surface, EDX averages the Ir concentration over the entire thickness of the film. Near an IrGe/Ge interface, EDX may pick up a signal from an overlapping IrGe microcrystal at the back of the specimen not visible in the STEM image, which can explain some small Ir background detected in the otherwise stoichiometrically perfect Ge matrix.

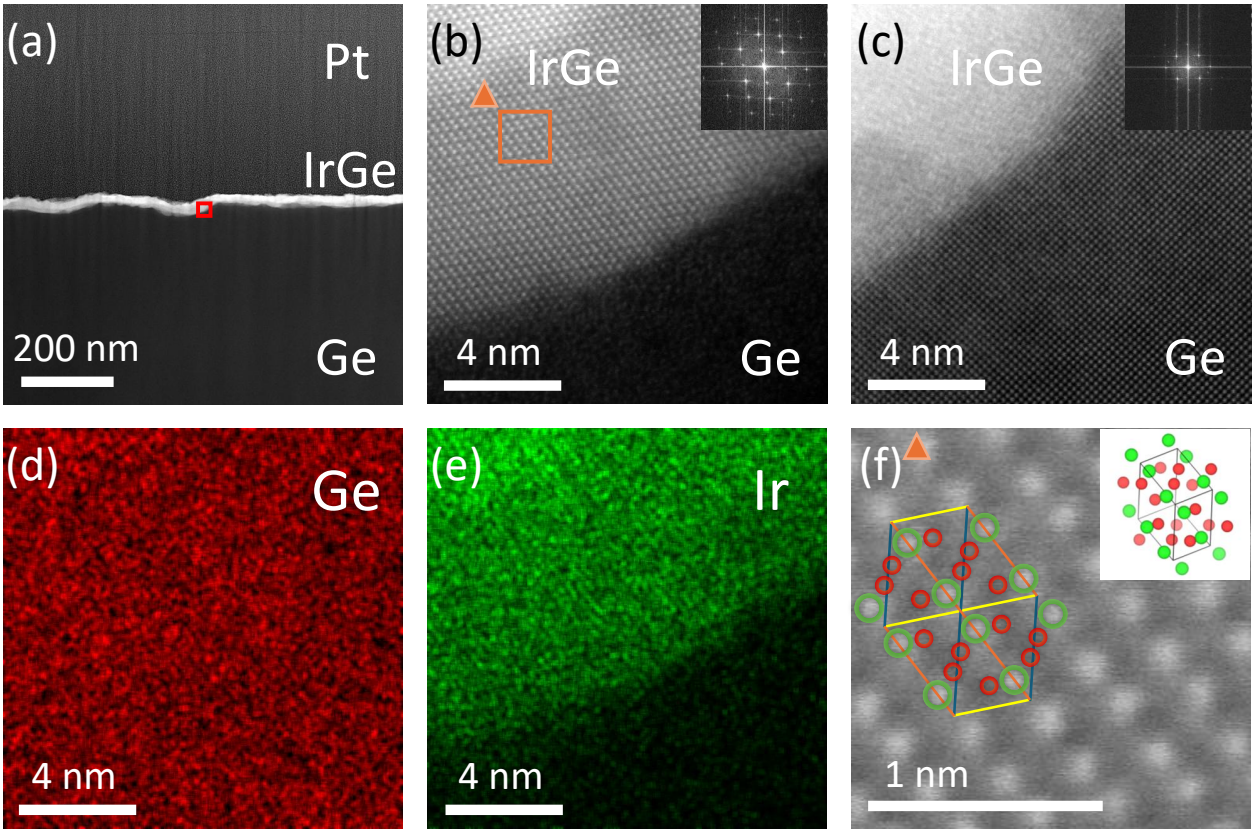


**Figure 3.7.** (a) Low magnification cross-sectional STEM image of an Ir 10 nm/Ge(001) sample annealed at 475 °C for 3.5 min. The sample is coated with a Pt protection layer. (b,c) High-angle annular dark field scanning transmission electron microscopy (HAADF-STEM) near the IrGe/Ge interface (red region in (a)) is performed at slightly different angles to match either the [111] orientation of IrGe or the [100] orientation of Ge lattices. Insets: fast Fourier transforms (FFT) of the images. (d,e) Energy-dispersive x-ray spectroscopy (EDX) of (b). (f) Atomic resolution STEM image of IrGe (orange region in (b)) with red and green circles indicating the positions of Ir and Ge atoms correspondingly. The yellow, blue, and orange lines indicate the $a$, $b$ and $c$ axes of the IrGe lattice. Inset: a view of an IrGe lattice seen along the [111] direction. (Reproduced from [1] under CC-BY 4.0.)

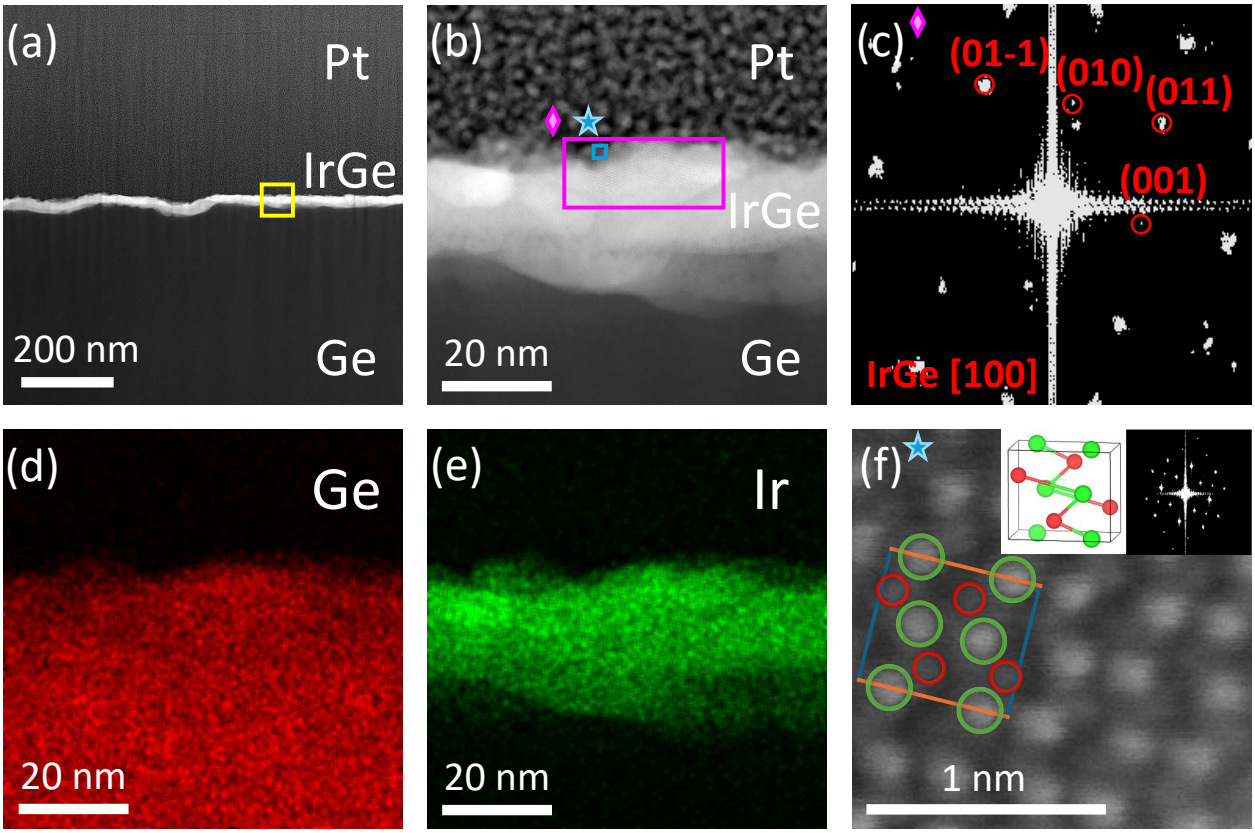


**Figure 3.8.** (a) Low-magnification cross-sectional STEM image of an Ir 10 nm/*i*-Ge film annealed at 475 °C for 3.5 min. The sample is coated with a Pt protection layer. (b) HAADF-STEM image of a flat region of the IrGe film (yellow region in (a)), with (c) the indexed FFT (of the magenta region in (b)) and (d,e) corresponding EDX maps. (f) Atomic-resolution STEM image near the top surface of the film (blue region in (b)), showing the orthorhombic phase (Pnma, space group No. 62) of IrGe, taken along the [100] orientation of the IrGe grain. Insets: schematic of the IrGe lattice and FFT of (f). The green circles mark Ir atoms, and the red circles mark Ge atoms. The *b* and *c* axes of the IrGe lattice are highlighted by blue and orange lines, respectively. (Reproduced from [1] under CC-BY 4.0.)

The detailed analysis of an atomic-resolution image of IrGe microcrystals Fig. 3.8(f) reveals the formation of an orthorhombic IrGe phase (Pnma, space group No. 62) with lattice parameters $b = (5.607 \pm 0.028)$ Å, $c = (6.294 \pm 0.018)$ Å, and angle $(89.62 \pm 0.34)°$ between $b$ and $c$. Lattice parameters determined for bulk IrGe crystals using XRD [173], [175] fall within the error bars of our measurements, indicating the formation of unstrained IrGe.

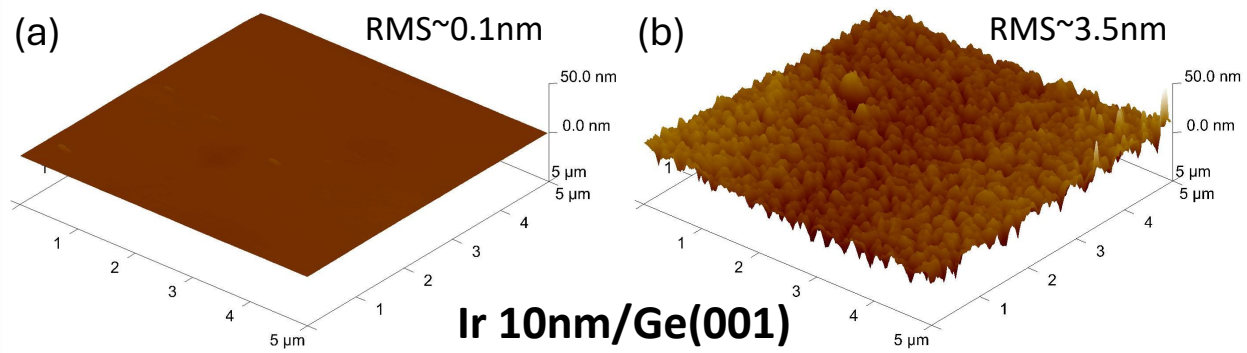


**Figure 3.9.** AFM images of 10 nm Ir on $i$-Ge before (a) and after (b) annealing at 475 °C for 3.5 min. (Reproduced from [1] under CC-BY 4.0.)

The surface morphology studies of IrGe films corroborate the formation of a polycrystalline film. In Fig. 3.9, we plot atomic force microscope (AFM) images of a sample before and after annealing. The surface of an Ir/Ge(001) sample before annealing is smooth with an RMS roughness $R_q \sim 0.1$ nm. Some shallow holes (a few nm deep) likely originate from the surface of the Ge wafer and are formed during acid cleaning prior to Ir deposition. The surface of the annealed sample shows the formation of bumps with a lateral size of $(57 \pm 22)$ nm and $R_q \sim (3.5 \pm 1.0)$ nm. Based on TEM images, these bumps can be attributed to the formation of IrGe microcrystals.

### 3.2.3 Additional Surface Analysis

Preliminary x-ray photoelectron spectroscopy (XPS) tests of Ir/SiGe samples before and after annealing with unannealed Ir/Si control samples are conducted by Dr. Gyula Eres at Oak Ridge National Laboratory. From the XPS results, the chemical interaction between Ir and SiGe is qualitatively confirmed by the binding energy (BE) shift of Ir $4f$ peaks.

When a base element is doped with another element, if there is some chemical interaction between them and the base element has a higher electronegativity, the electron density around it will increase because of its reduction, so the BE will decrease, and vice versa. In our case, the electronegativity is 2.20 for Ir, 1.90 for Si, and 2.01 for Ge. Therefore, we expect the BE of Ir to decrease and the BE of Ge to increase.

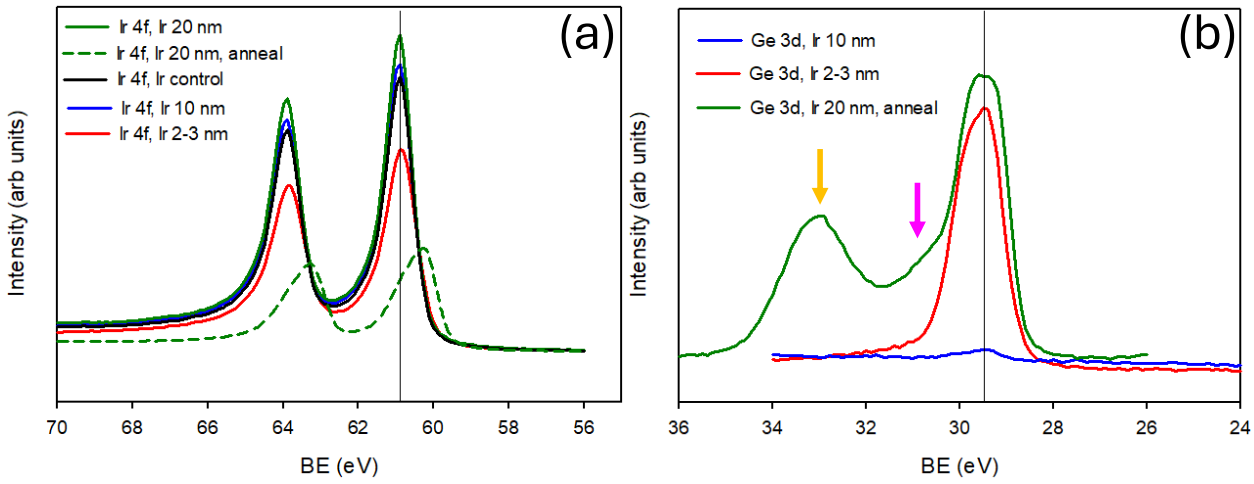


**Figure 3.10.** The x-ray photoelectron spectroscopy (XPS) results of Ir/SiGe 22-244 before and after long 475 °C annealing. A clear shift in the binding energy (BE) of Ir $4f$ peaks is observed after annealing, indicating chemical interaction between Ir and SiGe. XPS measurements are performed by Dr. Gyula Eres at Oak Ridge National Laboratory.

In Fig. 3.10(a), the Ir/Si control sample and the unannealed samples of Ir 10 nm or 20 nm/SiGe are equal in BE($4f_{5/2}$) = 63.8 eV and BE($4f_{7/2}$) = 60.8 eV for the elemental Ir. The unannealed sample of Ir 2–3 nm/SiGe shows a tiny shift of $\approx -0.06$ eV in these peaks, which is consistent with its slightly higher $T_c \approx 0.15$ K compared to $T_c \approx 0.1$ K of the Ir/Si reference film. A BE shift of $\approx -0.7$ eV is observed relative to elemental Ir for annealed Ir 20 nm/SiGe, indicating the formation of an IrSiGe phase due to the chemical interaction at the Ir/SiGe interface. The minor peaks of elemental Ir observed for the annealed sample denote that a small amount of elemental Ir may still exist. This is in agreement with the higher concentration of Ir near the top surface even in optimally annealed IrGe films (Fig. 3.8(e)).

In Fig. 3.10(b), BE($3d_{3/2}$) = 29.7 eV and BE($3d_{5/2}$) = 29.1 eV for the elemental Ge in the SiGe substrate are observed from both unannealed and annealed Ir/SiGe samples. The elemental Ge peaks for the Ir 10 nm/SiGe sample are barely visible due to screening by the thick Ir film, while those for Ir 10 nm/SiGe with an ultrathin Ir capping layer are clearer. Extra peaks (pink and orange arrows) appear in the annealed Ir 20 nm/SiGe sample, with BE shifts of $\approx +(1\text{–}1.5)$ eV and $\approx +3.5$ eV. The BE shift of $\approx +3.5$ eV might be too strong for Ge if we assume that it comes from the oxidation by Ir. However, this peak agrees with

the BE($3d_{5/2}$) = 32.5 eV for $GeO_2$ [198]. GeO also has a peak of BE($3d_{5/2}$) = 30.9 eV with a shift of $< +1$ eV relative to the Ge bulk, which might be very close to what we expect for IrSiGe. Before Ir/SiGe samples are annealed, only Ir is exposed to air, but Ir hardly reacts with oxygen at room temperature. After annealing and the film turns to IrSiGe, Ge is transferred to the top surface of the samples and is subject to reaction with oxygen in the air, possibly forming thin GeO and $GeO_2$ films. Therefore, it is difficult to discern directly from Fig. 3.10(b) whether there is some chemical interaction between Ir and SiGe. A possible approach is to repeat the XPS measurement after cleaning the potential $GeO_x$ on the surface with HCl and HF/BOE and immediately loading to vacuum, although XRD or STEM is a more straightforward way to characterize the phase of the obtained IrSiGe.

### 3.2.4 Thermal budget of strained Ge quantum wells

For superconducting germanides to be used with strained Ge quantum wells grown at $\sim 550\,^{\circ}$C, it is important to identify annealing conditions beyond which the quality of the two-dimensional (2D) gas is degraded, either due to strain relief or Si diffusion across the SiGe/Ge interface. As a metric, we choose the quantum mobility of a 2D hole gas $\mu_{\mathrm{q}} = 1/B^*$, which can be obtained from the onset magnetic field $B^*$ where Schubnikov-de Haas (SdH) oscillations appear. For these experiments we used a deep (200 nm) quantum well with modulation doping, where density and mobility are not very sensitive to the surface condition, and 2D gas with hole density $\sim 1.2 \times 10^{11}$ cm$^{-2}$ is formed in as-grown wafer without an external electric field. The samples were annealed at $T_{ann}$ for $t_{ann}$ in a forming gas, then indium contacts were made to the corners of square samples in order to measure transport properties in the van der Pauw geometry. Transport measurements were performed at $T = 250$ mK using low-frequency lock-in techniques.

In Table. 3.4, we show that wafers annealed at 475 °C do not degrade at least up to 20 min of annealing. A sample annealed at 500 °C for 10 minutes shows reduced $\mu_{\mathrm{q}}$, indicating degradation of the 2D gas quality either due to the reduction of the quantum well depth due to partial Ge strain relief or the onset of Si migration into the quantum well. Therefore, we use 500 °C as the upper limit for our studies. More details will be discussed in Section 4.4.1.

**Table 3.4.** Dependence of a Ge QW 2D hole gas quantum mobility $\mu_q$ on the annealing temperature $T_{ann}$ and time $t_{ann}$. (Reproduced from the supplemental material of [1] under CC-BY 4.0.)

| $T_{ann}$ (°C) | 475 | | | | | | 500 |
|---|---|---|---|---|---|---|---|
| $t_{ann}$ (min) | 1 | 2 | 4 | 10 | 10 | 20 | 10 |
| $p$ ($10^{11}$/cm$^2$) | 1.21 | 1.17 | 1.22 | 1.12 | 1.55 | 1.41 | 1.21 |
| $B^*$ (T) | 0.20 | 0.22 | 0.21 | 0.20 | 0.21 | 0.20 | 0.30 |
| $\mu_q$ ($10^4$ cm$^2$/(V · s)) | 5.0 | 4.5 | 4.8 | 5.0 | 4.8 | 5.0 | 3.3 |

### 3.3 Discussion

In this chapter, we have investigated and compared the superconducting properties of Pd, Pt, Rh, and Ir germanide thin films formed by solid-phase epitaxy, with the detailed characterization of IrGe and IrSiGe films. The optimal annealing temperature increases from Pd to Ir but remains within the thermal budget of strained Ge/SiGe heterostructures. We verified that the quantum mobility $\mu_q = (3\text{–}5) \times 10^4\,\mathrm{cm}^2/(\mathrm{V}\cdot\mathrm{s})$ of the two-dimensional hole gas in strained Ge quantum wells is not substantially degraded by the highest annealing temperatures used in this study. The high-resolution STEM and EDX analyses of IrGe films reveal that Ir reacts with Ge to form a self-limiting, polycrystalline IrGe layer with a sharp IrGe/Ge interface. Optimally annealed IrGe films exhibit the highest critical temperature $T_c \approx 3.4\,\mathrm{K}$ and upper critical magnetic field $B_{c2} \approx 3.4$ T. In contrast, over-annealed IrGe films show a suppression of superconductivity, with both $T_c$ and $B_{c2}$ dropping to near zero, which we attribute to the formation of the semiconducting $Ir_4Ge_5$ phase. IrSiGe films exhibit slightly lower superconducting parameters, with $T_c \approx 2.6\,\mathrm{K}$ and $B_{c2} \approx 2.8\,\mathrm{T}$ but demonstrate greater thermal stability. This enhanced robustness is likely due to the formation of the more stable metallic IrSi phase. Our results establish that Ir(Si)Ge thin films formed via solid-phase epitaxy provide a viable route for fabricating high-$T_c$, high-$B_c$ superconducting contacts to Ge-based Josephson field-effect transistors (Ge JoFETs). These materials offer a promising platform for integrating high-performance superconducting electronics with strained Ge quantum wells in a process fully compatible with mature CMOS technology.

## 3.4 Methods

$Si_{0.15}Ge_{0.85}$ wafers used in this study were grown on *p*-doped Si(001) substrates by reduced-pressure chemical vapor deposition (RP-CVD). Undoped Ge(001) wafers were purchased from MTI Corporation. All wafers were degreased using toluene, acetone, and isopropanol with ultrasonication. Prior to loading into the deposition system, the native surface oxide was removed by sequential dips in HCl:$H_2O$ (1:6) for 15 seconds and HF:$H_2O$ (1:10) for 10 seconds, followed by a 10-second rinse in deionized (DI) water.

Iridium (Ir) was deposited by DC sputtering in a KJL PVD-75 system at Sandia National Laboratories under a 3 mTorr Ar atmosphere, using 100 W DC power, substrate rotation at 20 rpm, and a 75° tilt angle, at a deposition rate of approximately 1 Å/s. Palladium (Pd), platinum (Pt), and rhodium (Rh) films were deposited at normal incidence by electron-beam evaporation in an AJA ATC 1800-HY hybrid deposition system at Purdue University, with a base pressure below $10^{-8}$ Torr and a deposition rate of 1–1.5 Å/s. In both systems, substrates were maintained at room temperature during deposition.

Following deposition, samples were annealed in an Ar atmosphere using a home-built rapid thermal annealing system with a heating and cooling rate of 1 °C/s. Electrical and magnetotransport measurements were conducted on samples patterned in either Hall bar or van der Pauw geometries, using a $^3$He system or a dilution refrigerator. Conventional low-frequency (10–30 Hz) four-terminal lock-in techniques were employed.

For high-resolution scanning transmission electron microscopy (HRSTEM) studies, a $< 100$ nm-thick lamella was prepared using a Thermo Scientific Helios G4 UX DualBeam focused ion beam (FIB) system. Transmission electron microscopy (TEM) imaging and energy-dispersive x-ray spectroscopy (EDX) were performed using a Thermo Scientific Themis Z system at an acceleration voltage of 300 kV. Atomic force microscopy (AFM) images were acquired using a Veeco Dimension 3100 AFM system.

### 3.4.1 Analysis of IrGe lattice constants and microcrystal sizes

The lattice constants of IrGe microcrystals were measured and calculated from STEM images. In high-magnification STEM images, such as Fig. 3.8(f), the periods of Ir lattices

along different orientations are directly measured using ImageJ software [199]. Using the calibrations derived from Ge lattices, such as Fig. 3.7(c), which has known lattice constants, the lattice constants of IrGe crystals are calculated and averaged over several images.

The size of IrGe microcrystals was estimated from STEM and AFM images. In low-magnification STEM images, such as Fig. 3.7(b), grain boundaries are visible, and grain sizes are measured directly using ImageJ software [199] and averaged over several grains in the image. AFM images are analyzed using Gwyddion software [200], which calculates the average grain size and the grain size distribution.

## 3.5 Extended Tables

The superconducting properties and the resistivity of a few annealed PdGe and RhSiGe films are listed below in Tables. 3.5 and 3.6.

**Table 3.5.** Parameters of some PdGe films formed using different annealing conditions. Most parameters are defined in Table. 3.2. Sheet resistivity $\rho_\square$ is measured in van der Pauw geometry. Resistivity $\rho$ is calculated assuming that all Pd reacts with Ge to form PdGe with the thickness 2.15 $d^{\mathrm{Pd}}$. (Reproduced from the supplemental material of [1] under CC-BY 4.0.)

| $d^{\mathrm{Pd}}$ (nm) | $T_{\mathrm{ann}}$ (°C) | $t_{\mathrm{ann}}$ (min) | $T_{\mathrm{c}}$ (K) | $\Delta T_{\mathrm{c}}$ (K) | $B_{\mathrm{c2},\perp}$ (T) | $\Delta B_{\mathrm{c2},\perp}$ (T) | $\rho_\square$ ($\Omega/\square$) | $\rho$ ($\mu\Omega\cdot$m) |
|---|---|---|---|---|---|---|---|---|
| 10 | 350 | 10 | 0.236 | 0.043 | 0.005 | 0.026 | 4.29 | 0.09 |
| | 400 | 10 | 0.235 | 0.002 | 0.007 | 0.001 | 5.30 | 0.11 |

**Table 3.6.** Parameters of some RhSiGe films formed using different annealing conditions. Most parameters are defined in Table. 3.2. Sheet resistivity $\rho_\square$ is measured in van der Pauw geometry. Resistivity is calculated assuming that all Rh reacts with Ge to form RhGe with the thickness 2.16 $d^{\mathrm{Rh}}$. (Reproduced from the supplemental material of [1] under CC-BY 4.0.)

| $d^{\mathrm{Rh}}$ | $T_{\mathrm{ann}}$ | $t_{\mathrm{ann}}$ | $T_{\mathrm{c}}$ | $\Delta T_{\mathrm{c}}$ | $B_{\mathrm{c2},\perp}$ | $\Delta B_{\mathrm{c2},\perp}$ | $\rho_\square$ | $\rho$ |
|---|---|---|---|---|---|---|---|---|
| (nm) | (°C) | (min) | (K) | (K) | (T) | (T) | ($\Omega/\square$) | ($\mu\Omega\cdot$m) |
| | 450 | 10 | 1.26 | 0.03 | 0.98 | 0.40 | 17.1 | 0.37 |
| 10 | 475 | 5 | 1.28 | 0.22 | 1.30 | 0.15 | 25.1 | 0.54 |
| | 500 | 5 | 1.26 | 0.02 | 1.06 | 0.60 | 22.4 | 0.48 |

# 4. DEVELOPMENT OF SUPERCONDUCTING CONTACTS TO GE QUANTUM WELL

In this chapter, we present our work on the development of different types of superconducting contacts to Ge.

## 4.1 Superconducting Contacts Without Annealing

Since Al has been proven to form superconducting contacts to Ge QW with high transparency [22]–[24], [26], [27], [29], we first try to reproduce the highly transparent Al contacts using the Ge wafers we have.

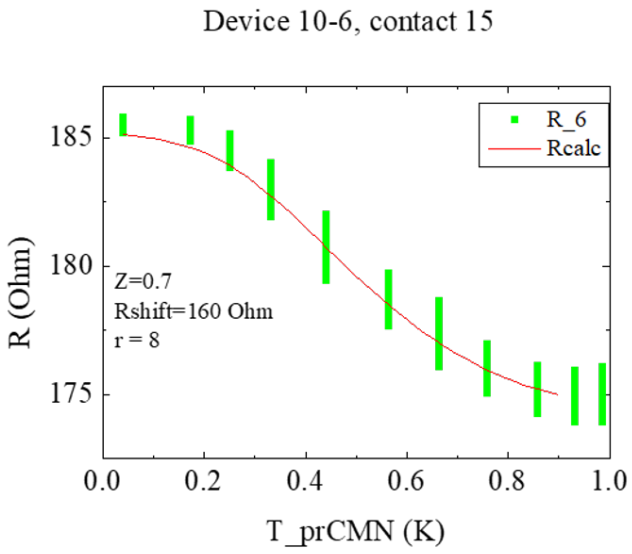


**Figure 4.1.** BTK fitting of Al contacts on wafer 19-220. A constant shift of resistance is introduced trying to extract the transparency $Z$.

Although induced superconductivity was not directly observed due to the large optical lithographic patterns we used, we get some signs of relatively low interface transparency, with the best $Z \sim 0.7 < 1$ using the fit from the BTK model. Although the fitting in Fig. 4.1 is not unambiguous, which requires an additional parameter for better fitting, the contact resistance gets low and does not increase significantly below $T_c$(Al). These signs indicate we are probably close to optimal cleaning procedures.

To help optimize superconducting contact fabrication, we test different contact metal stacks with $p^{++}$-Ge wafers. The possibility of surface contact and large carrier density make superconducting contacts easier to fabricate and optimize than working with Ge QWs. The assumption is that we might lower the Schottky barrier by choosing suitable materials with better band alignment to $p$-Ge as the interface and induce a larger superconducting gap by proximitizing the very thin interface material with higher $T_c/Bc$ superconductors, like NbTi or MoRe. Thus, a larger induced superconducting gap with improved transparency is expected if we choose the proper contact metal stack.

Thin Al, Pd, MoRe, and NbTi are evaporated on $p^{++}$-Ge wafer 21-335 as interface material, with widely separated optical lithographic contact patterns. NbTi/NbTiN caps are deposited on top, trying to induce a larger superconducting gap and prevent oxidation. Fig. 4.2 shows the $T$-dependence of 3-terminal contact resistance $R_{3t}$ below the $T_c$ of the capping superconductor. Samples with Al or Pd interfaces show a similar trend of decreasing $R_{3t}$ at lower temperatures compared to the increasing $R_{3t}$ of MoRe- or NbTi-interfaced samples. Therefore, among these four materials we have at the time of the experiment, Al and Pd may work better as the superconducting contact interface material to $p$-Ge.

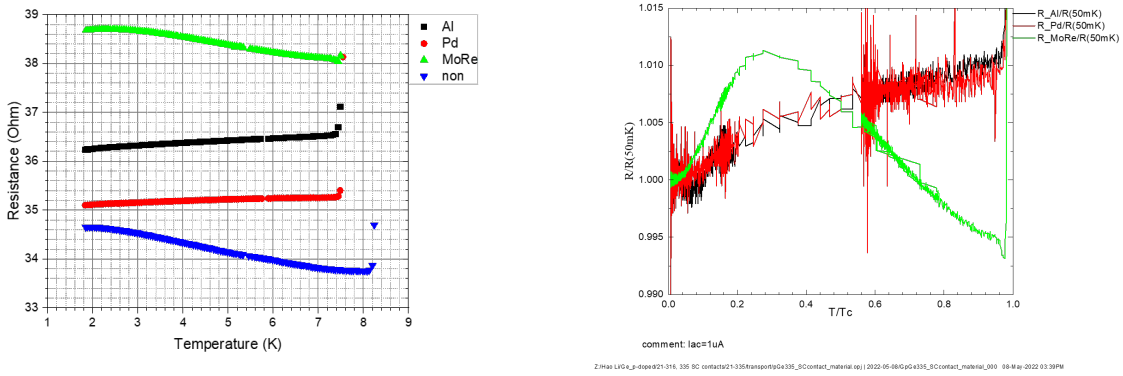


(a) (b)

**Figure 4.2.** Superconducting contact material testing with $p^{++}$-Ge 21-335. The contact metal stacks include thin Al, Pd, MoRe, or NbTi as interface materials and NbTi/NbTiN caps. The blue curve in (a) corresponds to the NbTi/NbTiN contact stack with no extra interface material below the cap but NbTi itself.

In Fig. 4.2(b), there is a decrease of $R_{3t}$(MoRe) below $\sim 0.25T_c$(MoRe), so we cannot completely rule out MoRe as a candidate for contact interface material from this experiment. However, a disadvantage of MoRe is that it can be dissolved in water or aqueous solutions, especially when adding $H_2O_2$ or heating, because MoRe can be easily oxidized even in air, and their oxides are soluble in water. From some follow-up characterization of MoRe thin films after months of storage in air, the metal surface becomes visibly rough. The resistivity increases and $T_c$ decreases clearly, especially for $< 10\,\text{nm}$ ultra-thin films, indicating the possible formation of a few nanometers of oxide layer. Therefore, we need to be careful with wet processing and sample storage after MoRe growth. Dipping of MoRe samples in aqueous solutions has to be limited and not conducted at high temperatures. Storage of MoRe samples in an oxygen- and moisture-free environment is crucial to avoid sample degradation.

## 4.2 Annealed Superconducting Contacts to $p^{++}$-Ge

Some detailed results of the annealing condition tests for Pd or Pt on $p^{++}$-Ge substrates are posted in Table. 4.1.

The annealed Pt(Pd)Ge samples are dipped in $\text{HCl} : \text{DI} = 1 : 6$ or $\text{HF} : \text{DI} = 1 : 10$ for 10 min respectively. No visual degradation or a clear decrease in $T_c$ has been observed. Therefore, it should be safe to clean Ge samples with annealed PdGe or PtGe contacts in dilute HCl or HF/BOE.

After optimizing the annealing condition for PtGe and PdGe contacts, we first characterize the induced superconductivity to $p^{++}$-Ge to get an initial understanding of the band alignment and interface barrier. JJs are fabricated without mesa and contact etching, so the current can not only transport across the junction but also the entire area. The measured resistance is the junction resistance in parallel with a small shunt resistance from transport through the surrounding area. When the junction is in the superconducting state, the measured resistance should be zero. Therefore, this configuration is not very suitable for direct measurement of $I_cR_N$ because the measured resistance is not the normal resistance of the junction $R_N$ itself, but we can still measure the correct $I_c$.

**Table 4.1.** Critical temperatures of palladium or platinum germanides at different annealing conditions. 10 nm Pd/$p^{++}$-Ge 22-188 or 10 nm Pt/$p^{++}$-Ge 22-187 is annealed in an Ar atmosphere using our home-built annealing station. Each condition states the highest annealing temperature with the time delay at this temperature. Critical temperature $T_c$ denotes the temperature where resistance starts to rise from zero.

| Metal | Pd | | | Pt | | | |
|---|---|---|---|---|---|---|---|
| Anneal $T$ (°C) | 300 | 350 | 400 | 350 | 400 | 400 | 400 |
| Anneal $t$ | 10′ | 10′ | 10′ | 5′ | 15″ | 1′ | 5′ |
| $T_c$ (K) | 0.132 | 0.129 | 0.146 | 0.460 | 0.485 | 0.500 | 0.494 |

Fig. 4.3(a) is an example of the annealed Pt(/NbTi) JJ sample structure. For each sample, JJs with three different junction lengths $L$ around 100, 500, and 900 nm are characterized. Figs. 4.3(b) and 4.3(c) show the differential resistance $R$ when applying DC current $I_{dc}$ across the JJs for Pt and Pt/NbTi samples. A hard gap is induced across $\sim$ 100 nm JJ for both samples, on $p^{++}$-Ge 22-208 with a very short mean free path $l = 10$ nm. Although Pt/NbTi 100 nm JJ has a slightly harder gap than Pt JJ, and Pt/NbTi 900 nm JJ has a clearer sign of induced superconductivity compared to Pt JJ, no significant enhancement in $I_c$ or $T_c$ is observed when Pt is capped with NbTi(N) before annealing. We guess that the issue might be a small physical gap created between PtGe and NbTi after annealing, due to the change in Pt thickness. As a consequence, NbTi is still in contact with the Pt contact below, but only through some random points. Such a gap created between metal films after diffusion of one metal layer into the semiconductor has been seen in Ti/Pd/$WTe_2$ contacts, where a gap appears between Ti and Pd after Pd diffuses into $WTe_2$ [201].

Meanwhile, since vertical JJs with $p^{++}$-Ge at the surface may be of significant interest, we run a few tests to check its feasibility with Al or PtGe contacts. The sample structure is very similar to Fig. 4.3(a) but with a common ground. For the Al sample, 50 nm Al is annealed at 350 °C for 1 min to limit Al diffusion into Ge. For the Pt sample, 20 nm Pt is annealed at 400 °C for 10 min with a 1 °C/s ramp. $I_c$ vs. $L$ plots are measured at $T \sim 32$ mK.

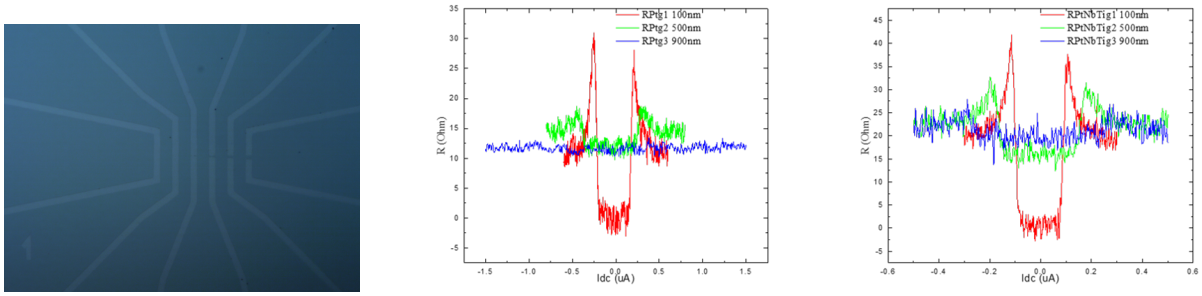


(a) (b) (c)

**Figure 4.3.** Characterization of Pt(/NbTi) Josephson junctions (JJs) with $p^{++}$-Ge 22-208. (a) Pt JJ sample without mesa and contact etching, after 15 min 400 °C annealing in Ar atmosphere. (b) Differential resistance $R$ vs. $I_{\mathrm{dc}}$ across the junction for Pt JJs with different gap widths of 100, 500, and 900 nm. (c) $R$ vs. $I_{\mathrm{dc}}$ for Pt/NbTi JJs with different gap widths of 100, 500, and 900 nm. For both samples, Pt thickness is 20 nm. The Pt/NbTi sample is capped with 5 nm NbTi/10 nm NbTiN.

Since the thickness of $p^{++}$-Ge layer 25 nm in 21-316 is much larger than the mean free path $l \sim 1.5\,\mathrm{nm}$, this wafer is effectively a 3D system. We use $m^* = (2/m_{\mathrm{t}} + 1/m_{\mathrm{l}})^{-1} = 0.042m_{\mathrm{e}}$ as the effective mass, where $m_{\mathrm{l}} = 1.56m_{\mathrm{e}}$ and $m_{\mathrm{t}} = 0.087m_{\mathrm{e}}$. The mean free path:

$$l = \frac{\hbar k_{\mathrm{F}} \mu}{e}, \tag{4.1}$$

where $k_{\mathrm{F}} = \sqrt[3]{3\pi^2 p_{3\mathrm{D}}}$ and $p_{3\mathrm{D}}$ is the 3D hole density. In the clean limit, the coherence length $\xi_0 = \xi_{\mathrm{BCS}} = \hbar v_{\mathrm{F}}/\pi\Delta$, where $v_{\mathrm{F}} = \hbar k_{\mathrm{F}}/m^*$. In the dirty limit ($l \ll \xi_0$), the coherence length:

$$\xi_{\mathrm{d}} = \sqrt{\xi_0 l}, \tag{4.2}$$

where Usadel equation [202] is valid. Using $p_{3\mathrm{D}} = 6.58 \times 10^{20}/\mathrm{cm}^3$, $\mu = 8.47\,\mathrm{cm}^2/(\mathrm{V}\cdot\mathrm{s})$, and $T_{\mathrm{c}} \approx 1.3\,\mathrm{K}$ for the deposited Al film from measurement, we estimate $\xi_{\mathrm{d}} \sim 90\,\mathrm{nm}$ for Al JJ.

For diffusive JJs, the relevant energy scale is the Thouless energy:

$$E_{\mathrm{Th}} = \frac{\hbar D}{L^2} = \frac{\hbar}{\tau_{\mathrm{Th}}}, \tag{4.3}$$

where $D = v_F l/3$ is the diffusion constant, and $\tau_{Th}$ is the dwell time in the JJ. In short diffusive JJs ($\Delta \gg E_{Th}$, or equivalently, $L \ll \xi_d$), a full gap $\Delta$ is induced, and the critical current should follow [203]–[205]:

$$eI_c R_N \approx \frac{1.326\pi}{2}\Delta \approx 2.07\Delta. \tag{4.4}$$

In long diffusive JJs ($\Delta \ll E_{Th}$, or $L \gg \xi_d$), a much smaller gap $\Delta_g \approx 3.1E_{Th}$ is induced [206], and the zero temperature $eI_c R_N$ is proportional to $E_{Th}$ [207], [208]:

$$eI_c R_N(T = 0) \approx 10.82E_{Th} \approx 3.2\Delta_g. \tag{4.5}$$

In our samples without mesa etching, we estimate the normal resistance $R_N$ of the junction region between two superconducting leads by:

$$R_N \approx \frac{\rho L}{W}, \tag{4.6}$$

where $\rho$ is the 2D resistivity of the $p^{++}$-Ge wafer, and $W$ is the width of the junction. Therefore, we expect $I_c \propto 1/L$ in the short-junction regime and $I_c \propto 1/L^3$ in the long-junction regime at low temperature, which has been observed in long diffusive graphene JJs [209].

In Fig. 4.4, both Al and PtGe JJs seem to follow the power law relation, $I_c R_N \propto E_{Th} \propto 1/L^2$, in the long-junction regime, when $E_{Th} \gg k_B T$ is true for these data points. The $I_c R_N$ of the $L \sim 50\,\text{nm} < \xi_d$ Al JJ clearly deviates from the power law trend to the lower side, indicating that $I_c R_N$ starts to saturate when getting close to the short-junction regime. The $eI_c R_N \approx 18\mu$eV induced gap in the shortest Al JJ is comparable to the induced gap in Ge QW solely by Al [22], [23].

We estimate $eI_c R_N \sim 0.1E_{Th}$ for Al JJs, and $eI_c R_N \sim 0.2E_{Th}$ for PtGe JJs in the long-junction regime, which are suppressed by about two orders of magnitude from the theoretical prediction. Similar suppression has also been observed in graphene-based JJs [130], [209], [210], where people attribute it probably to the effective increase of the dwell time in the JJ due to the suppressed transmission at the S-Sm interface. In this sense, PtGe contacts seem

to have better transparency to $p$-Ge than Al contacts. Similar enhancement of induced gap to $p$-Ge by annealed contacts using Pt compared to Al contacts has been observed in Ge QW in the ballistic regime, although Al has the larger gap [25].

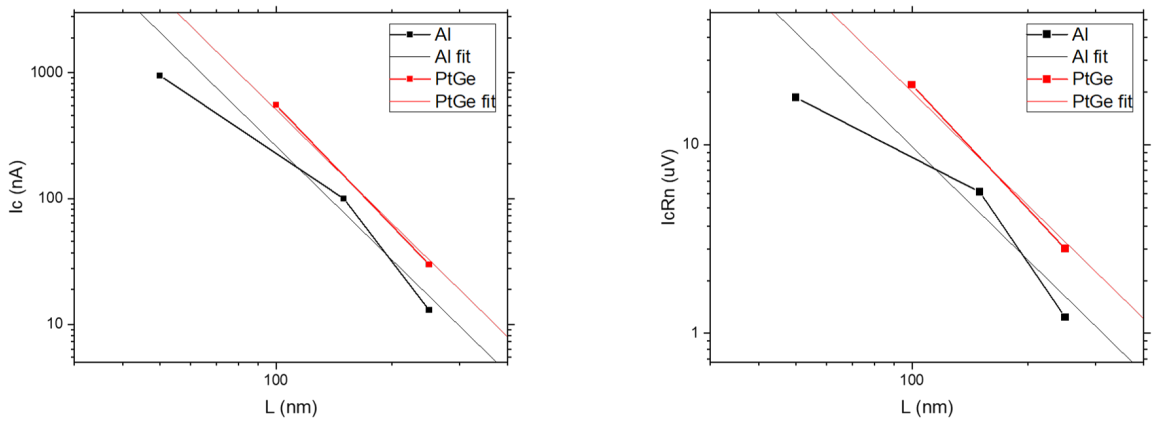


(a) (b)

**Figure 4.4.** Characterization of coherence length for Pt and Al Josephson junctions (JJ) with $p^{++}$-Ge 21-316 and no mesa or contact etching. (a) Critical current $I_c$ vs. junction length $L$ for Al and Pt JJs, fitted by $I_c \sim L^{-3}$ in the long-junction regime. (b) $I_cR_N$ vs. $L$ for Al and Pt JJs, where $R_N$ is the normal resistance of the shunted JJ, fitted by $I_cR_N \sim L^{-2}$ the long-junction regime. For the Al sample, 50 nm Al is annealed at 350 °C for 1 min for a limited diffusion. For the Pt sample, 20 nm Pt is annealed at 400 °C for 10 min with a 1°C/s ramp.

On vertical JJs using $p^{++}$-Ge, since $I_c$ drops dramatically when $L > \xi_d$, fabrication may be much easier if we use $p^{++}$-Ge wafers with larger $\xi_d$. Utilizing the several wafers with almost 3 times larger $\xi_d$ than the wafer used in Fig. 4.4, we can hopefully get JJs that work up to $0.5 \sim 1\,\mu$m if we use the same kind of contacts.

We also measured the out-of-plane critical field $B_{c,z}(R = 0)$ of the contact materials, as $B_{c,z}$ is important for superconducting contacts to Ge QW in the QH regime. For the shortest $L \sim 100$ nm PtGe JJ in Fig. 4.4, $B_{c,z} \approx 80$ mT, and for the shortest $L \sim 50$ nm Al JJ, $B_{c,z} \approx 25$ mT. They are all below the $\sim 0.5$ T requirement of the QHFM regime for Ge QW.

Although $NbGe_2$ [170], [171], [174] forms at very high temperatures $\gg 500$ °C, $Nb_5Ge_3$ ($T_c = 0.30$ K) [211] can form $\lesssim 500$ °C [178], [212], [213]. Interdiffusion of amorphous Nb/Si

also begins at low temperature $T \leqslant 250\,^{\circ}\mathrm{C}$ [214], which might be able to create superconducting $Nb_5Si_3$ ($T_c = 0.70\,\mathrm{K}$) [215] $\lesssim 500\,^{\circ}\mathrm{C}$. Therefore, Nb might be a candidate material for contacts to (Si)Ge. While both $Nb_5Ge_3$ and $Nb_5Si_3$ have $T_c < 1\,\mathrm{K}$, a possible way to induce a larger superconducting gap into Ge is to control the annealing temperature and time, only to form a thin layer of $Nb_x$(Si)Ge at the Nb/(Si)Ge interface. The Nb(Si)Ge interlayer may help create a clean and sharp interface to Ge and proximitize the superconductivity of the remaining Nb film to Ge, thus enhancing $T_c$ and $B_c$ of the contacts.

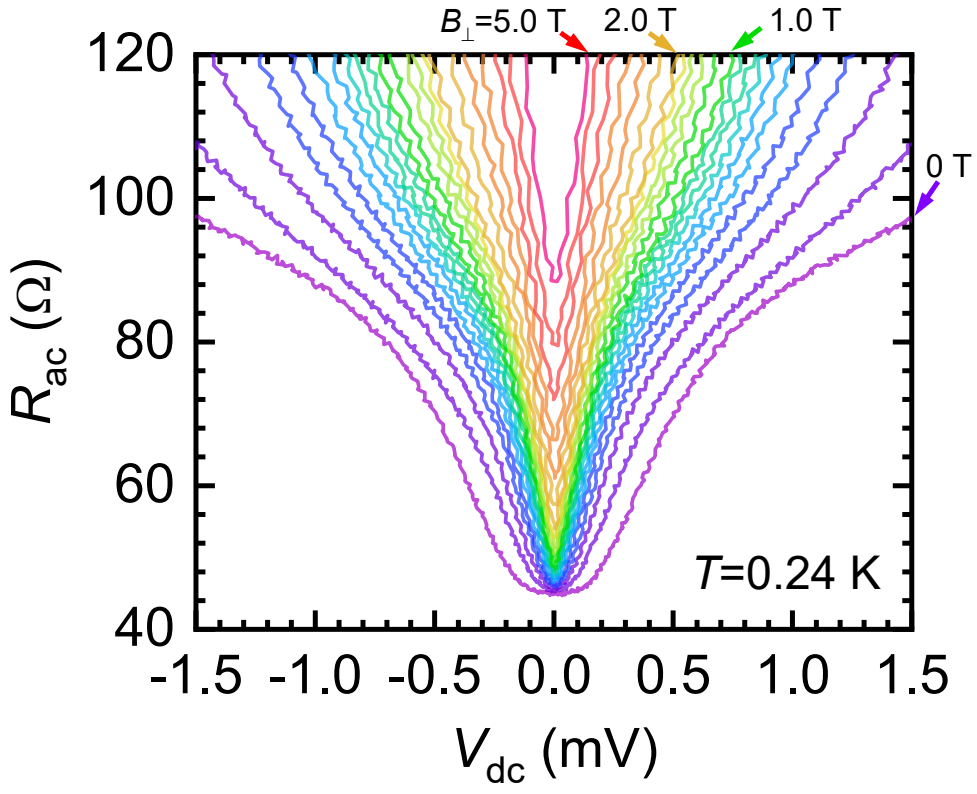


**Figure 4.5.** Contact resistance of annealed NbTi 15 nm/NbTiN 5 nm contacts deposited on $p^{++}$-Ge 21-335. The sample is annealed in an Ar atmosphere at 500 °C for 3 min with a ramp rate of 1 °C/s.

The results of a preliminary test of NbTi/Ge contacts in the configuration of Fig. 4.9 are shown in Fig. 4.5. NbTi 15 nm/NbTiN 5 nm contacts are deposited on $p^{++}$-Ge 21-335 wafers after mesa etching. The sample is annealed in Ar at 500 °C for 3 min with a ramp rate of 1 °C/s. Our as-grown NbTi film has $T_c \approx 9\,\mathrm{K}$, and NbTiN film has $T_c \gtrsim 12\,\mathrm{K}$. The onset

temperature for the signature of induced superconductivity is $\sim 1.2\,\mathrm{K}$. At $T = 0.24\,\mathrm{K}$ and $B_\perp = 0$, the induced gap $\Delta^* \sim 2k_\mathrm{B}T_\mathrm{c} \sim 200\,\mu\mathrm{eV}$ is expected, until it vanishes at $B_\perp \sim 4\,\mathrm{T}$.

We can try to increase the critical temperature and field of the induced superconductivity by reducing the annealing temperature or time or growing slightly thicker Nb(Ti). The concern of growing thick Nb(Ti)/Nb(Ti)N contacts is still a risk of creating a physical gap between annealed Nb(Ti)Ge and unannealed Nb(Ti)/Nb(Ti)N films. We should also note that the high transparency of the superconducting contacts in Fig. 4.5 might come from the high carrier density in the $p^{++}$-Ge wafers. The same high transparency is not guaranteed when applying Nb(Ti) contacts to Ge/SiGe QWs.

## 4.3 Annealed Pd(Pt)SiGe Superconducting Contacts to Ge Quantum Well

Detailed results of the annealing condition tests for Pd or Pt on SiGe substrates are listed in Table. 4.2. Similar to annealed Pt(Pd)Ge samples, Pt(Pd)SiGe samples are also resistant to dipping in diluted HCl or HF.

Combining Tables. 4.1 and 4.2, the optimal annealing conditions that result in the highest $T_\mathrm{c}$ and sharpest superconducting transition are chosen to be: 10 min at 400 °C for Pd contacts and 5 min at 350 °C for Pt contacts.

PtSiGe or PdSiGe superconducting contacts to Ge QW are tested with JJs fabricated on one side of a straight mesa. Because Ge QWs have a large mean free path $l \sim 1\,\mu\mathrm{m}$, to stay near the ballistic regime, the gaps are designed to be 500, 700, 900, and 1200 nm. PMMA 495 C8 is used in e-beam lithography (EBL) for deep mesa and contact dry etching. 20 nm of Pd or Pt is e-beam evaporated at 45° from the side. 30 nm MoRe is sputtered on top from the side for Pd(Pt)/MoRe samples. 50 nm MoRe is side-deposited on two other samples to test MoRe contacts with or without 450 °C annealing.

**Table 4.2.** Critical temperatures of palladium or platinum silicide-germanides at different annealing conditions. 20 nm Pd or Pt/SiGe 22-212 is annealed in an Ar atmosphere using our home-built annealing station. Each condition states the highest annealing temperature $T_A$ with the time delay at this temperature $t_A$. Critical temperature $T_c$ denotes the temperature where resistance is half of the normal state resistance. $\Delta T_c$ is the width of the superconducting transition.

| Metal | Pd | | Pt | | | | | | | | |
|---|---|---|---|---|---|---|---|---|---|---|---|
| $T_A$ (°C) | 350 | 400 | 250 | | 300 | 350 | | | | 400 | |
| $t_A$ | 10′ | 10′ | 5′ | 10′ | 2′ | 0′* | 2′ | 5′ | 10′ | 5′ | 10′ |
| $T_c$ (K) | 0.28 | 0.30 | 0.38 | 0.40 | 0.35 | 0.53 | 0.57 | 0.59 | 0.56 | 0.56 | 0.54 |
| $\Delta T_c$ (K) | 0.06 | 0.02 | 0.06 | 0.04 | 0.12 | 0.06 | 0.09 | 0.04 | 0.06 | 0.05 | 0.04 |

*: Flash annealing with no time delay at 350 °C.

During fabrication of this test device, we did not account for proximity exposure of EBL, and narrow gaps are consumed after deep dry etching, causing shorting of narrow JJs. Even in wider JJs, since the contacts in these devices extend into the mesa for a few microns, the possibility of deposition on sidewalls makes the junction length $L$ not very well defined.

MoRe JJs with and without 10 min 450 °C annealing both show strong barriers without any sign of induced superconductivity. The most possible explanation is the high annealing temperature required for the interface reaction to happen between MoRe and Ge [178].

The survived JJ in the Pd sample with 1200 nm designed gap width shows a weak signature of induced superconductivity, as shown in Fig. 4.6(b). Similarly, the 900 nm designed gap in the Pd/MoRe sample shows an even weaker induced gap on top of a small barrier. The 1200 nm designed gap in the Pd/MoRe sample, however, shows the barrier only.

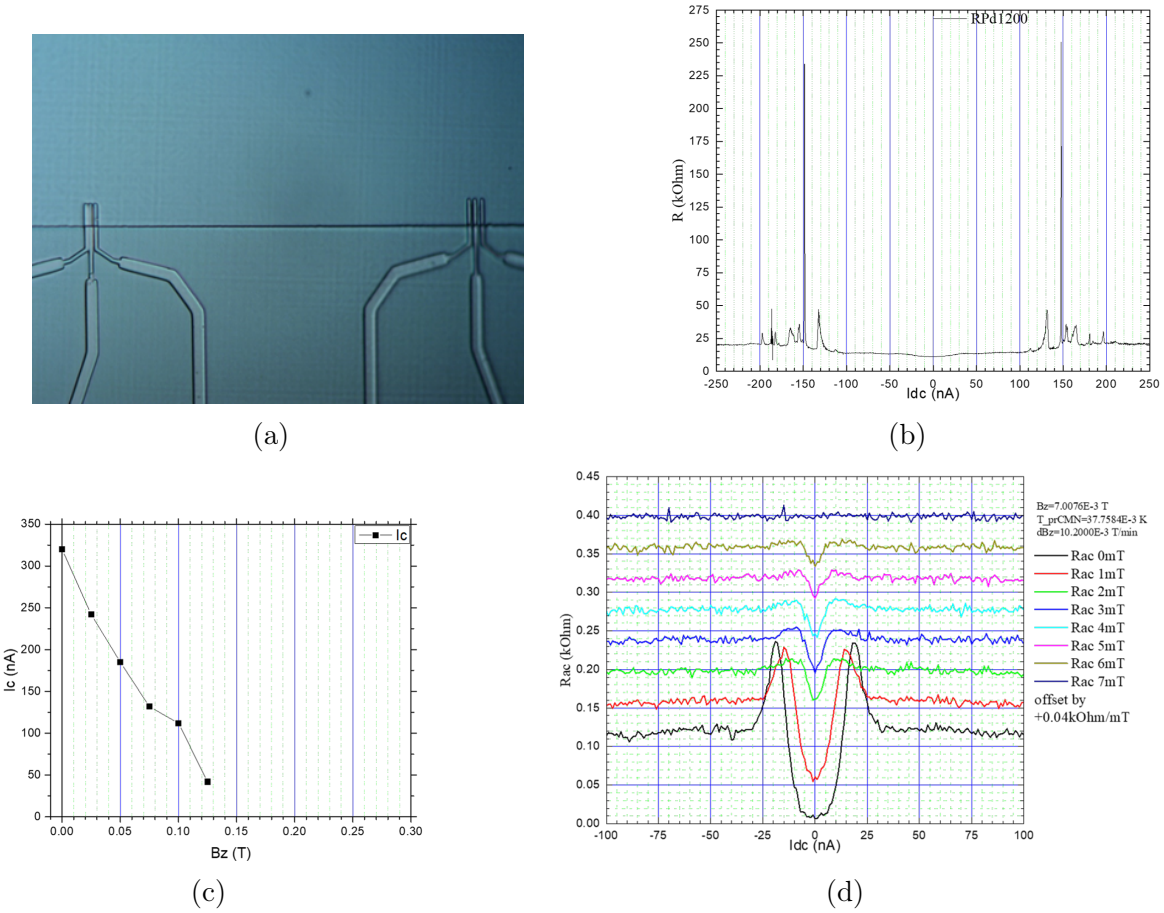


**Figure 4.6.** Characterization of Pt(/MoRe) Josephson junctions (JJs) with Ge/SiGe quantum well 22-213. (a) Example of JJ sample structures with mesa etching and contact etching on the same side of the straight mesa. The gaps are designed to be 500, 700, 900, and 1200 nm, from left to right. (b) Differential resistance $R_{\mathrm{ac}}$ vs. DC current $I_{\mathrm{dc}}$ for 1200 nm designed Pd JJ. (c) Critical current $I_{\mathrm{c}}$ vs. out-of-plane magnetic field $B_z$ of 700 nm designed Pt JJ. (d) $R_{\mathrm{ac}}$ vs. $I_{\mathrm{dc}}$ for 900 nm designed Pt/MoRe JJs.

In the Pt sample, the 900 nm and 1200 nm designed gaps exhibit wide, soft superconducting gaps. The 700 nm designed gap shows a hard superconducting gap, but further experiments are required to figure out whether there is any shorting due to Pt interdiffusion. The out-of-plane field $B_z$ dependence of the critical current $I_{\mathrm{c}}$ for the 700 nm gap is provided in Fig. 4.6(c). The critical field for the junction $B_{z,\mathrm{c}} \sim 0.13\,\mathrm{T}$ is about the same as the critical field measured with the shorted 500 nm gap. Although our measured $B_{z,\mathrm{c}}$ is slightly higher than $B_{z,\mathrm{c}} < 100\,\mathrm{mT}$ in Ref. [25], it is still way below the QHFM regime for Ge QW.

More importantly, we desire to induce superconductivity across a helical 1D channel wide enough ($\sim 1\,\mu$m) for the QH edge state to exist near the interface. Therefore, the induced superconductivity of PtSiGe itself across the 700 nm gap still does not satisfy the critical field requirement.

According to Fig. 4.6(d), the soft induced gap across the 900 nm designed gap in the Pt/MoRe sample completely vanishes at $B_z = 7\,\mathrm{mT}$. Neither the Pd/MoRe nor the Pt/MoRe sample exhibits significant improvement of induced superconductivity by proximitizing MoRe, and even an extra barrier seems to be introduced in the Pd/MoRe sample by MoRe, compared with the Pd sample. If we want to stay with Pt(Pd)SiGe as the interface with higher $T_\mathrm{c}$ superconductors in proximity, one possible solution is to use $AlO_x$ (or ZnO, etc.,) as a hard mask and sacrificial layer [216]. The hard mask allows high-temperature annealing and contact self-alignment between Pt(Pd) evaporation and NbTi (or MoRe) sputtering. After Pt(Pd) is annealed and fully reacts with SiGe, a layer of NbTi or MoRe can be deposited to ensure that there is no gap between Pt(Pd)Ge and a high-$B_\mathrm{c}$ superconductor layer.

## 4.4 High-$T_\mathrm{c}$, High-$B_\mathrm{c}$ Superconducting Contacts to Ge Quantum Well

### 4.4.1 Resistance of Ge Quantum Wells to High-Temperature Annealing

If IrSiGe or RhSiGe has a low Schottky barrier to $p$-Ge similar to PtSiGe, it may be an adequate candidate for high-$T_\mathrm{c}$ high-$B_\mathrm{c}$ superconducting contacts to Ge QWs. However, Ir and Rh require much longer high-temperature annealing than Pt to obtain high $T_\mathrm{c}$ and $B_\mathrm{c}$. In this case, interdiffusion in the Ge QWs after exceeding the thermal budget may be of great concern. To understand whether Ge QWs can withstand the harsh annealing conditions required to obtain optimal Ir(Rh)SiGe contacts, we anneal Ge QW wafer 22-213 at high temperatures and characterize the SdH oscillations to evaluate the change in quantum mobility.

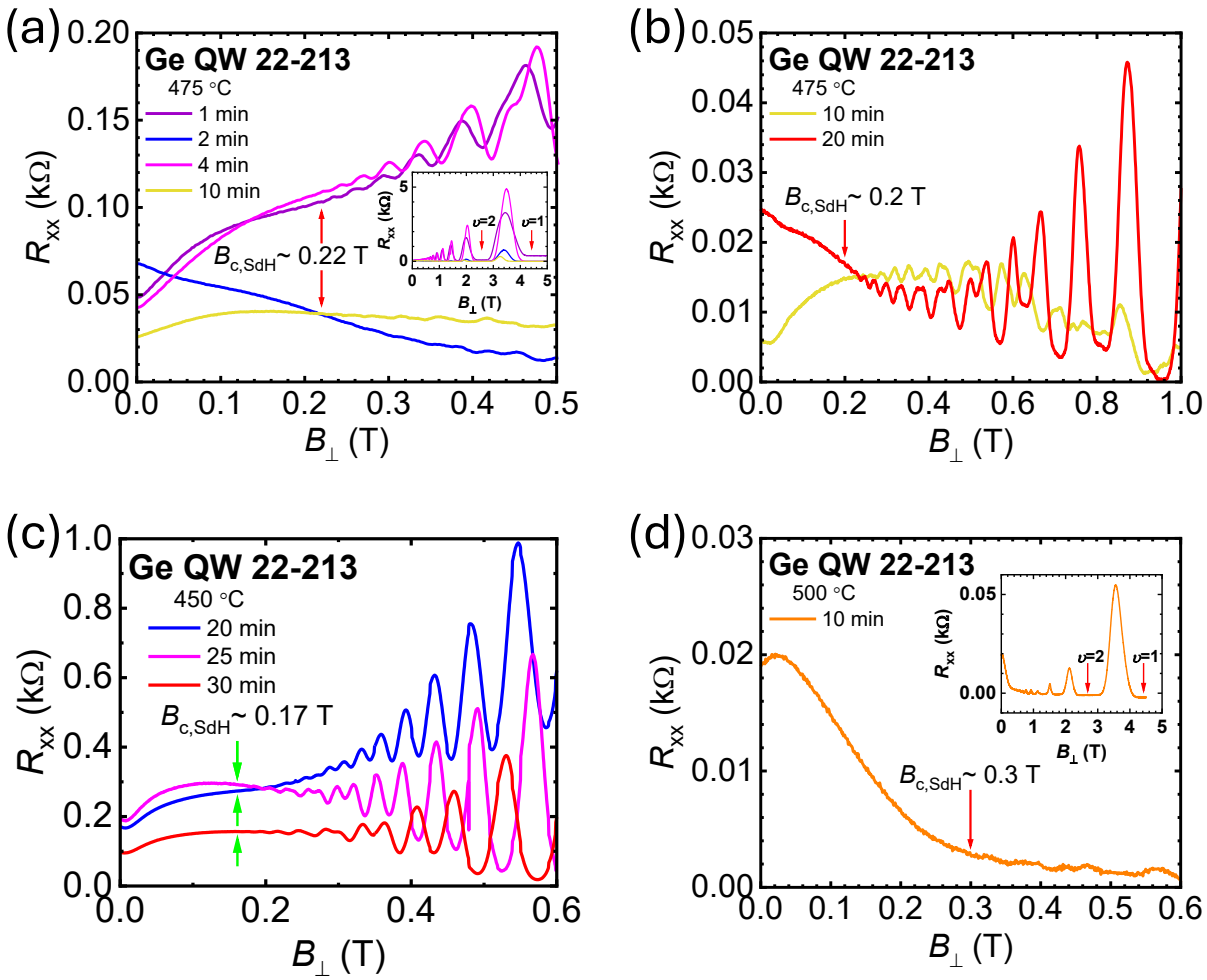


**Figure 4.7.** Shubnikov–de Haas oscillations of Ge quantum well wafer 22-213 after annealing in an Ar atmosphere at (a,b) 475 °C, (c) 450 °C, and (d) 500 °C, performed a year after the wafer was grown, without other treatment to the wafer.

Fig. 2.5 presents the SdH oscillations upon wafer arrival, and Fig. 4.7 shows the SdH oscillations after different high-temperature annealing performed about a year after the wafer arrives. Comparing Figs. 4.7(a,d) with Fig. 2.5, we see that the carrier density seems to increase from $\sim 8.8 \times 10^{10}\,\mathrm{cm}^2/(\mathrm{V}\cdot\mathrm{s})$ to $\sim 1.3 \times 10^{11}\,\mathrm{cm}^2/(\mathrm{V}\cdot\mathrm{s})$ after annealing, while it is about the same among all these annealing conditions. Therefore, Ge QWs should be able to survive after Ir(Rh)SiGe contact annealing. However, we have seen in Section 2.2.6 that RTA in Ar or forming gas can help reduce the interface trap density and increase the carrier density, so whether the enhancement in carrier density after Ar RTA requires comparison to

unannealed wafer 22-213 that is stored in the air for more than a year. The measurement of the unannealed aged 22-213 wafer shows that the wafer is not conducting due to natural surface oxidation when no further treatment is applied. After the native oxide is removed by acid, the carrier density $p \gtrsim 10^{11}\,\mathrm{cm}^2/(\mathrm{V}\cdot\mathrm{s})$ is restored. Thus, we can conclude that RTA in Ar can help reduce the surface trap density on the Ge cap and recover the carrier density towards saturation density.

From Figs. 2.5 and 4.7(a–c), a decrease in the onset point of the SdH oscillation is observed from $B_{\mathrm{c,SdH}} \sim 0.35\,\mathrm{T}$ before annealing to $B_{\mathrm{c,SdH}} \lesssim 0.2\,\mathrm{T}$ after various 450 °C or 475 °C annealing. Thus, we get $\mu_{\mathrm{q}} \sim 2.9{\times}10^4\mathrm{cm}^2/(\mathrm{V}\cdot\mathrm{s})$ before annealing and $\mu_{\mathrm{q}} \gtrsim 5{\times}10^4\mathrm{cm}^2/(\mathrm{V}\cdot\mathrm{s})$ after 450 °C or 475 °C annealing, neither of which are more than an order of magnitude smaller than the transport mobility. This indicates a relatively small Dingle ratio, suggesting a large angle scattering dominance, which is induced by background impurities [140]. This ratio is defined as the transport scattering time $\tau_{\mathrm{t}} = \mu m^*/\mathrm{e}$ divided by $\tau_{\mathrm{q}}$, which is roughly $\tau_{\mathrm{t}}/\tau_{\mathrm{q}} \sim \mu/\mu_{\mathrm{q}}$. In Fig. 4.7(d), after 10 min annealing at 500 °C, the onset seems to increase to $B_{\mathrm{c,SdH}} \sim 0.3\,\mathrm{T}$, which roughly sets an upper limit of the annealing conditions.

Fig. 4.7(b) also manifests a clear sign of Zeeman splitting, which is not obvious before annealing. This demonstrates a change in the ratio $r = E_{\mathrm{Z}}/E_{\mathrm{c}} = m^* g_\perp/2m_{\mathrm{e}}$, or, similarly, in the ratio of LL broadening $\Gamma$ and $E_{\mathrm{Z}}$ (or $E_{\mathrm{c}} - E_{\mathrm{Z}}$). The QHFM transition can survive if $r$ is further enhanced at low density, but it can possibly disappear otherwise. By plotting the data in Fig. 4.7(b) as $R$ vs. $B_0/B$ in Fig. 4.8, where $B_0 = e/nh$ is adjusted to assign integer filling factors to the minima of spin non-degenerate LLs, we see that odd-number LLs vanish first as $B$ decreases. Since $\Gamma$ does not increase after the annealing, it probably indicates that $E_{\mathrm{Z}}$ decreases compared to $E_{\mathrm{c}}$ at high density. Whether $r$ also worsens at low density after such annealing requires further measurements on gated devices that are annealed in these conditions before gate fabrication. However, in general, even though we have confirmed that the quantum oscillation of the QW does not clearly degrade after harsh high-temperature annealing, we may still want to reduce the thermal budget as much as possible.

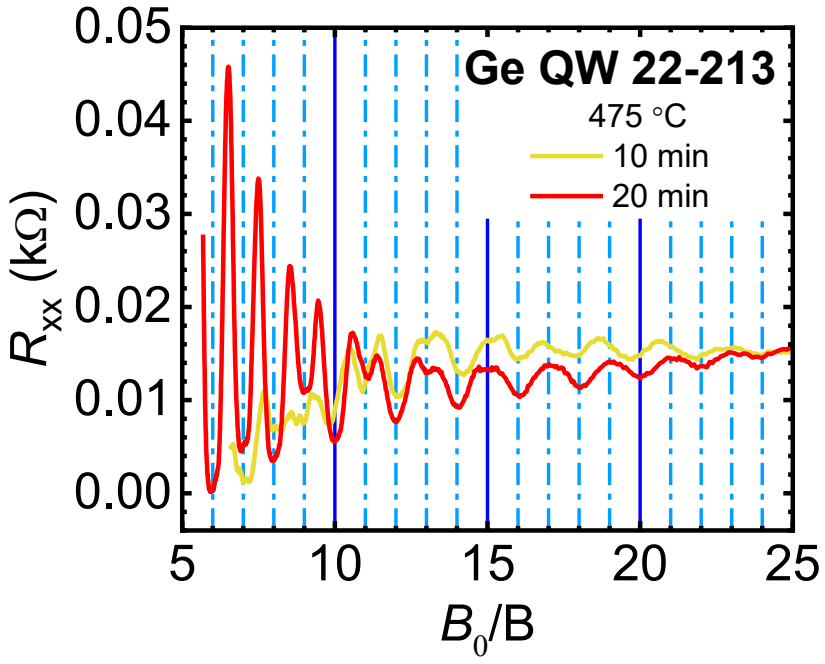


**Figure 4.8.** Filling factor numbering for the Shubnikov–de Haas oscillations of Ge quantum well wafer 22-213 after high-temperature annealing in Ar. $R_{xx}$ is plotted against $B_0/B$, where $B_0 = e/nh$ is adjusted to assign integer filling factors to the minima of spin non-degenerate LLs. The filling factor of an $R_{xx}$ minimum can be directly read from the corresponding $B_0/B$ value.

### 4.4.2 IrSiGe Superconducting Contacts to Ge Quantum Wells

We have prepared mesa-etched side contact samples for 3-terminal contact resistance tests, as well as JJ samples to characterize the induced superconductivity of IrSiGe to Ge QWs.

Both kinds of samples are fabricated with mesa etching below the B modulation doping layer and contact etching to the QW. From the test results of Ir/(Si)Ge annealing in Chap. 3, we choose to deposit 10 nm Ir for the contacts to balance the optimal annealing conditions for Ir/Ge and Ir/SiGe with the thermal budget of the strained Ge QWs. Due to the extremely thin contact $\sim 20$ nm compared to the height of the mesa $\gtrsim 270$ nm, the mesa etching recipe is chosen to create a relatively small sidewall angle to ensure contact continuity across the mesa edge. Since the sputtering equipment does not have substrate rotation flexibility, the contact etching recipe is chosen to create less steep sidewalls with no resist overhang to create reliable side contacts to the QW.

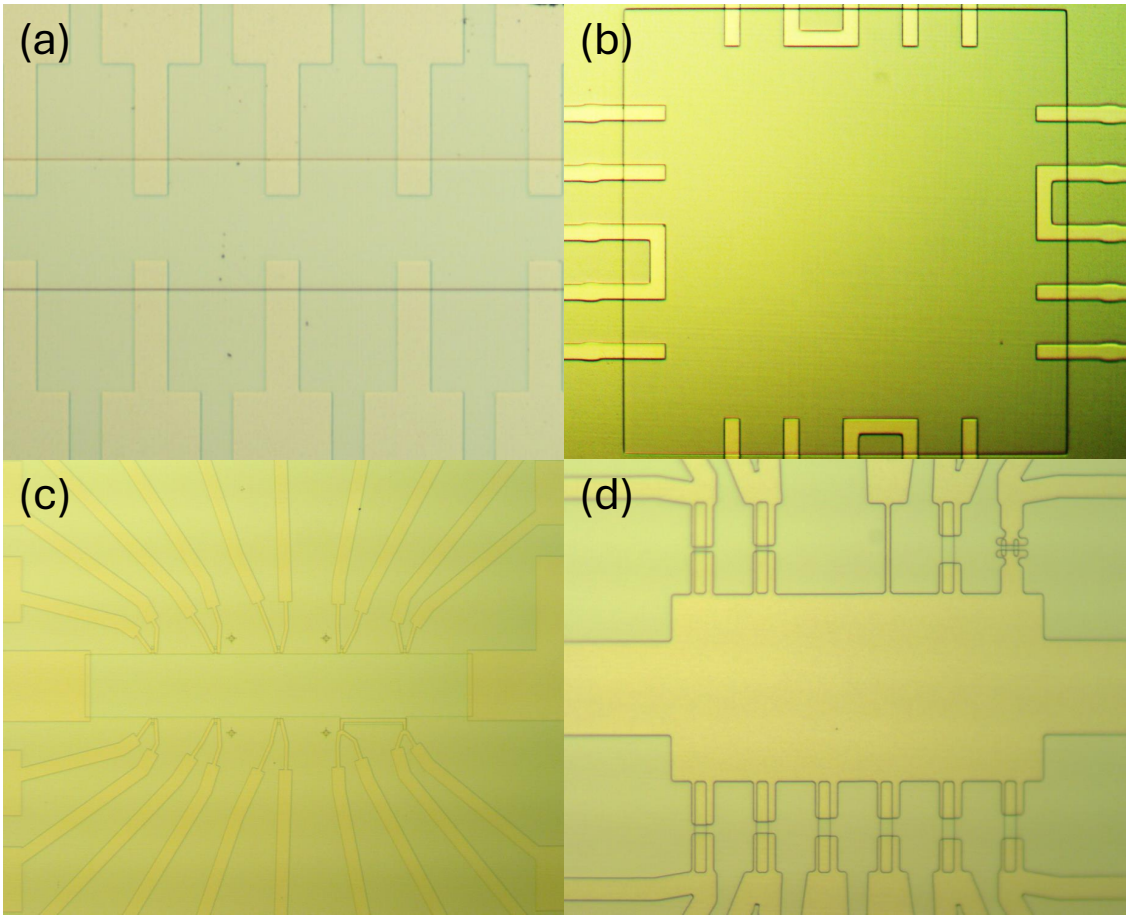


**Figure 4.9.** Optical images of IrSiGe (a–c) contact or (d) Josephson junction samples using Ge quantum well wafer 22-213. Yellow regions are annealed IrSiGe contacts. Green regions are mesas surrounded by the etched SiGe substrates. The width of the side contacts is 50 nm in (a), and $\approx 4\,\mu$m in (b–d).

Using samples 4.9(a–c), we can extract the transparency of the IrSiGe/Ge contact by measuring their 3-terminal contact resistance with DC bias. By measuring the JJ sample with the configuration of 4.9(d), we can learn about contact transparency, the induced superconducting gap, and the coherence length in Ge QWs.

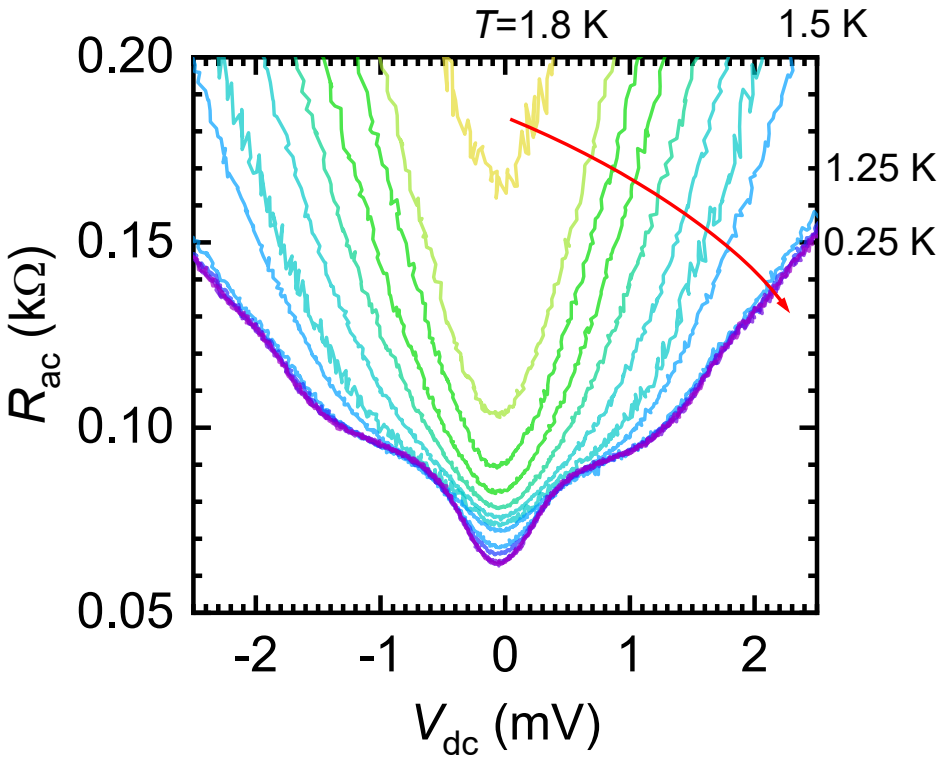


**Figure 4.10.** The differential resistance $R_{\rm ac}$ of the IrSiGe/Ge quantum well 22-213 contact as a function of the DC bias voltage $V_{\rm dc}$ by 3-terminal low-frequency lock-in measurement.

Due to the poor selectivity of the $SF_6/O_2$ dry etching recipe, earlier samples of deep Ge QW 22-213 using e-beam resist AR-P 6200.13 ($\approx$ 400–500 nm thick) all had thin metal strips along the edge of the mesa, which short all contacts. After removing the Ir shorts on the mesa by Ar ion milling or dry etching, we managed to measure some samples with the configurations of Fig. 4.9(b,c). The shorts on JJ samples (Fig. 4.9(d)) are difficult to align and remove completely.

Fig. 4.10 presents the differential resistance $R_{\rm ac}$ of a $\sim 25\,\mu$m-wide IrSiGe/Ge QW contact as a function of the DC bias voltage $V_{\rm dc}$ by 3-terminal measurement for a sample in Fig. 4.9(b). The IrSiGe wire has $T_{\rm c} \approx 2.25$ K, and the plot is measured when the carrier density of Ge QW is at saturation of $p \approx 1.3 \times 10^{11}/{\rm cm}^2$. Although the $R_{\rm ac}$–$V_{\rm dc}$ plot shows the feature of high transparency according to the BTK model, the induced gap $\Delta^*$ seems to be only about half of $\Delta \sim 2.3 k_{\rm B} T_{\rm c} \sim 400\,\mu$eV.

Samples are also made, as in Figs. 4.9(a,c,d), by optical lithography using AZ 1518 photoresist ($\approx 2\,\mu$m thick). Due to the resolution of optical lithography, we cannot fabricate JJs shorter than $\sim 1\,\mu$m. Even the shortest JJ we get remains in the normal state at $\sim 40\,$mK.

Samples as in Fig. 4.9(a) with large contacts have small contact resistances, comparable to the normal resistance of contact pads, so it is difficult to measure the contact resistance alone accurately and extract transparency from 3-terminal measurements. Signatures not as clean as but similar to Fig. 4.10 have been observed from most of such samples under multiple annealing conditions and remain up to $B_\perp \sim 1.3\,$T until IrSiGe wires/contact pads start getting to the normal state. Short IrSiGe JJ samples with gates on deep Ge QWs have to be fabricated to characterize the transparency of the contacts and the critical field of the induced superconductivity at low carrier density, which is required by the QHFM transition.

The fabrication and measurement of Rh (or Ir)/Ge QW JJs and Pt/Ge QW reference JJs with shorter junction lengths, using the 20 nm deep Ge QW wafer 22-211, is ongoing now. Similar JJs with Ir contact will be made using Ge QW wafer 19-219 or after characterizing the lowest carrier density and the corresponding mobility of 100 nm deep Ge QW wafer 22-212.

# 5. SUMMARY AND PERSPECTIVES

## 5.1 Summary

In conclusion, this thesis details a comparative study of the superconducting properties of Pt, Pd, Rh, and Ir germanides, along with an in-depth characterization of Ir(Si)Ge films formed by solid-phase epitaxy. For films fabricated under optimal epitaxy conditions, we report a critical temperature of 3.4 K (2.6 K) for IrGe (IrSiGe), a 4-fold increase in the superconducting gap size from that of PtSiGe. These films exhibit large out-of-plane critical magnetic fields $> 1$ T. The solid-phase epitaxy is performed within the thermal budget of strained Ge heterostructures. The high-resolution scanning transmission electron microscopy and energy-dispersive X-ray spectroscopy reveal that Ir reacts with Ge substrates to form a polycrystalline IrGe layer with a sharp IrGe/Ge interface. The demonstrated CMOS-compatible solid-phase epitaxy of polycrystalline IrGe films establishes a promising pathway for advanced Ge-based superconducting electronics, including the fabrication of high-performance Ge-based Josephson field-effect transistors.

We also present the test results of some different superconducting contacts to Ge. Signatures of induced superconductivity in IrSiGe/Ge quantum well field-effect transistors have been observed through 3-terminal contact resistance measurement with DC bias voltage. Fabrication of Ir(Rh)SiGe/Ge quantum well Josephson field-effect transistors to deep Ge quantum wells with more optimized processes is in progress to characterize the transparency and critical magnetic field of Ir(Rh)SiGe contacts.

Apart from Ir and Rh, the germanides of some other elements may also be tested to search for the superconducting contacts to Ge-based devices that can work in strong magnetic fields. While the annealing condition of tungsten germanide exceeds the thermal budget of Ge heterostructures [178], Nb [170], [171], Ta [170], [171], [177], V [170], Zr [170], [217], Hf [170], Sc [218], Y [218], [219], and Ru [159] may be worth trying, especially Nb and Ta, which can possibly achieve germanide films with high $B_c > 1$ T [177], [213] within the thermal budget of Ge heterostructures and be compatible with the fabrication of the well-developed Nb or Ta resonators. Mo [170], [220], [221] and MoRe [220] are also possible options. I have tested that the solid-state reaction between Mo and Si can happen at $\leqslant 500\,^{\circ}$C. Local annealing

by laser may also be considered for patterning, with selective etching of Mo(Re) from the resulting germanide/silicide by warm/hot water or dilute $H_2O_2$.

## 5.2 Combination of Superconducting Contacts and Helical 1D Channel in SiGe Quantum Well

After superconducting contact fabrication is optimized, we have to couple the contacts to the helical 1D channel in Ge QW using samples with structure like that shown in Fig. 1.8(b).

We first need to figure out how to create the helical 1D channel in Ge QW. According to Fig. 2.6, the $B^*(V_g)$ dependence is too weak so that we cannot control the QHFM transition between well-developed LLs by local electrostatic gate at a fixed $B$ in these wafers. Alternatively, we can keep the two sides of the device at the same $p(V_g)$ and introduce a $B$ field difference across the interface by a local ferromagnetic gate above the 2DHG. We see that the width $\Delta B^*$ of the QHFM transition in Ge QW is on the order of $\sim 10\,\mathrm{mT}$, so we need to enhance $B$ at the deep QW by $> \Delta B^*$ at external field $B \approx B^*$. The ferromagnetic gate can be fabricated by depositing a thin layer of common ferromagnetic materials like Co [222], [223] or Py (permalloy) [224], but generating $> 10\,\mathrm{mT}$ enhancement to the $> 200\,\mathrm{nm}$ deep QW might not be as trivial.

Subsequently, superconducting contacts will be placed at the two ends of the mesa at the gate interface. To search for signatures of non-Abelian excitations, new samples combining the coupled structure have to be designed. Moreover, as the ferromagnetic gate will inevitably cover the superconducting contacts at the interface, the field enhancement at these contacts that are much closer to the ferromagnetic layer may be much stronger than the enhancement at the QW. Therefore, a superconductor with $B_c$ just slightly above $B^*$ may not suffice in this kind of design.

## 5.3 Application to GaAs Quantum Wells and Other Systems

Although the fabrication of hybrid superconductor-helical Ge 1D channel systems is compatible with the mature CMOS technology [38], the Majorana fermions that can be hosted by this platform do not have a high enough order to perform universal topological

quantum computation. The helical 1D channel in GaAs/AlGaAs at $\nu = 2/3$ [103], on the other hand, can be utilized to create higher-order non-Abelian excitations.

In GaAs, $\varepsilon_{\mathrm{F}}$ at the surface is pinned in the middle of the band gap, resulting in a high Schottky barrier between the 2DEG and the superconductor, leading to non-ohmic contacts with low transparency. Several kinds of rhodium or palladium arsenides are found to be superconducting with $T_{\mathrm{c}} > 0.5\,\mathrm{K}$ [172], and, as we know, self-limited annealed contacts can have a cleaner contact interface. It might be worth testing if any of these annealed contacts to GaAs QW using platinum group metals can have a lower Schottky barrier. Pd/Ge has also been used for ohmic contacts to $n$-GaAs [225], where Ge forms an $n^+$ interface layer that may help reduce the barrier height [226]. This provides another possible direction to search for ohmic contacts to $n$-GaAs with higher $T_{\mathrm{c}}$ and $B_{\mathrm{c}}$ within platinum group metal/Ge annealed contacts. Furthermore, the self-aligned contact technique with a sacrificial hard mask can also be tried on GaAs QWs to enhance the induced gap if the technique is proved to work for Ge QWs. Alternatively, we may try the Nb/Ge(/Pd)/GaAs contact, where Ge diffuses to create a heavily doped region, and the remaining Ge reacts (partially) with Nb to form $\mathrm{NbGe}_x$ with a high $B_{\mathrm{c}}$ and a clean interface with GaAs. The annealing condition should not exceed the thermal budget of GaAs heterostructures [177].

# REFERENCES


[1] H. Li, Z. Shang, M. P. Lilly, M. Myronov, and L. P. Rokhinson, "Characterization of superconducting germanide and germanosilicide films of Pd, Pt, Rh, and Ir formed by solid-phase epitaxy," *APL Mater.*, vol. 14, no. 3, p. 031 101, Mar. 2026, ISSN: 2166-532X. DOI: 10.1063/5.0301077.

[2] A. Y. Kitaev, "Unpaired Majorana fermions in quantum wires," *Phys. Usp.*, vol. 44, no. 10S, pp. 131–136, 2001. DOI: 10.1070/1063-7869/44/10S/S29.

[3] N. Read and D. Green, "Paired states of fermions in two dimensions with breaking of parity and time-reversal symmetries and the fractional quantum Hall effect," *Phys. Rev. B*, vol. 61, pp. 10 267–10 297, 2000. DOI: 10.1103/PhysRevB.61.10267.

[4] A. Y. Kitaev, "Fault-tolerant quantum computation by anyons," *Ann. Phys.*, vol. 303, pp. 2–30, Jan. 2003. DOI: 10.1016/S0003-4916(02)00018-0.

[5] S. Das Sarma, M. Freedman, and C. Nayak, "Topologically protected qubits from a possible non-Abelian fractional quantum Hall state," *Phys. Rev. Lett.*, vol. 94, p. 166 802, 16 Apr. 2005. DOI: 10.1103/PhysRevLett.94.166802.

[6] C. Nayak, S. H. Simon, A. Stern, M. Freedman, and S. D. Sarma, "Non-Abelian anyons and topological quantum computation," *Rev. Mod. Phys.*, vol. 80, pp. 1083–1159, 2008. DOI: 10.1103/RevModPhys.80.1083.

[7] J. Preskill, "Quantum computing in the NISQ era and beyond," *Quantum*, vol. 2, p. 79, Aug. 2018, ISSN: 2521-327X. DOI: 10.22331/q-2018-08-06-79.

[8] Y. Kim, A. Eddins, S. Anand, *et al.*, "Evidence for the utility of quantum computing before fault tolerance," *Nature*, vol. 618, no. 7965, pp. 500–505, Jun. 2023, ISSN: 1476-4687. DOI: 10.1038/s41586-023-06096-3.

[9] R. M. Lutchyn, J. D. Sau, and S. D. Sarma, "Majorana fermions and a topological phase transition in semiconductor-superconductor heterostructures," *Phys. Rev. Lett.*, vol. 105, p. 077 001, 7 Aug. 2010. DOI: 10.1103/PhysRevLett.105.077001.

[10] Y. Oreg, G. Refael, and F. von Oppen, "Helical liquids and Majorana bound states in quantum wires," *Phys. Rev. Lett.*, vol. 105, p. 177 002, 17 Oct. 2010. DOI: 10.1103/PhysRevLett.105.177002.

[11] J. Alicea, Y. Oreg, G. Refael, F. von Oppen, and M. P. A. Fisher, "Non-Abelian statistics and topological quantum information processing in 1D wire networks," *Nat. Phys.*, vol. 7, no. 5, pp. 412–417, Mar. 2011, ISSN: 1745-2473. DOI: 10.1038/nphys1915.

[12] L. Fu and C. L. Kane, "Superconducting proximity effect and Majorana fermions at the surface of a topological insulator," *Phys. Rev. Lett.*, vol. 100, no. 9, p. 096 407, Mar. 2008, ISSN: 1079-7114. DOI: 10.1103/physrevlett.100.096407.

[13] L. Fu and C. L. Kane, "Josephson current and noise at a superconductor/quantum-spin-Hall-insulator/superconductor junction," *Phys. Rev. B*, vol. 79, p. 161 408, 16 Apr. 2009. DOI: 10.1103/PhysRevB.79.161408.

[14] A. Cook and M. Franz, "Majorana fermions in a topological-insulator nanowire proximity-coupled to an $s$-wave superconductor," *Phys. Rev. B*, vol. 84, no. 20, p. 201 105, Nov. 2011, ISSN: 1550-235X. DOI: 10.1103/physrevb.84.201105.

[15] A. M. Cook, M. M. Vazifeh, and M. Franz, "Stability of Majorana fermions in proximity-coupled topological insulator nanowires," *Phys. Rev. B*, vol. 86, no. 15, p. 155 431, Oct. 2012, ISSN: 1550-235X. DOI: 10.1103/physrevb.86.155431.

[16] J. Alicea, "Majorana fermions in a tunable semiconductor device," *Phys. Rev. B*, vol. 81, p. 125 318, 12 Mar. 2010. DOI: 10.1103/PhysRevB.81.125318.

[17] J. D. Sau, S. Tewari, and S. D. Sarma, "Probing non-abelian statistics with majorana fermion interferometry in spin-orbit-coupled semiconductors," *Phys. Rev. B*, vol. 84, no. 8, p. 085 109, Aug. 2011. DOI: 10.1103/PhysRevB.84.085109.

[18] J. D. Sau, R. M. Lutchyn, S. Tewari, and S. Das Sarma, "Generic new platform for topological quantum computation using semiconductor heterostructures," *Phys. Rev. Lett.*, vol. 104, no. 4, p. 040 502, Jan. 2010, ISSN: 1079-7114. DOI: 10.1103/PhysRevLett.104.040502.

[19] G. Scappucci, C. Kloeffel, F. A. Zwanenburg, *et al.*, "The germanium quantum information route," *Nat. Rev. Mater.*, vol. 6, no. 10, pp. 926–943, Oct. 2021. DOI: 10.1038/s41578-020-00262-z.

[20] A. Dimoulas, P. Tsipas, A. Sotiropoulos, and E. K. Evangelou, "Fermi-level pinning and charge neutrality level in germanium," *Appl. Phys. Lett.*, vol. 89, no. 25, p. 252 110, Dec. 2006, ISSN: 1077-3118. DOI: 10.1063/1.2410241.

[21] T. Nishimura, K. Kita, and A. Toriumi, "Evidence for strong Fermi-level pinning due to metal-induced gap states at metal/germanium interface," *Appl. Phys. Lett.*, vol. 91, no. 12, p. 123 123, Sep. 2007, ISSN: 1077-3118. DOI: 10.1063/1.2789701.

[22] N. W. Hendrickx, M. L. V. Tagliaferri, M. Kouwenhoven, *et al.*, "Ballistic supercurrent discretization and micrometer-long Josephson coupling in germanium," *Phys. Rev. B*, vol. 99, no. 7, p. 075 435, Feb. 2019, ISSN: 2469-9969. DOI: 10.1103/physrevb.99.075435.

[23] F. Vigneau, R. Mizokuchi, D. C. Zanuz, *et al.*, "Germanium quantum-well Josephson field-effect transistors and interferometers," *Nano Lett.*, vol. 19, no. 2, pp. 1023–1027, Jan. 2019, ISSN: 1530-6992. DOI: 10.1021/acs.nanolett.8b04275.

[24] K. Aggarwal, A. Hofmann, D. Jirovec, *et al.*, "Enhancement of proximity-induced superconductivity in a planar Ge hole gas," *Phys. Rev. Res.*, vol. 3, no. 2, p. l022005, Apr. 2021, ISSN: 2643-1564. DOI: 10.1103/physrevresearch.3.l022005.

[25] A. Tosato, V. Levajac, J.-Y. Wang, *et al.*, "Hard superconducting gap in germanium," *Commun. Mater.*, vol. 4, no. 1, p. 23, Apr. 2023, ISSN: 2662-4443. DOI: 10.1038/s43246-023-00351-w.

[26] M. Valentini, O. Sagi, L. Baghumyan, *et al.*, "Parity-conserving Cooper-pair transport and ideal superconducting diode in planar germanium," *Nat. Commun.*, vol. 15, no. 1, p. 169, Jan. 2024, ISSN: 2041-1723. DOI: 10.1038/s41467-023-44114-0.

[27] O. Sagi, A. Crippa, M. Valentini, *et al.*, "A gate tunable transmon qubit in planar Ge," *Nat. Commun.*, vol. 15, no. 1, p. 6400, Jul. 2024, ISSN: 2041-1723. DOI: 10.1038/s41467-024-50763-6.

[28] M. Hinderling, S. C. ten Kate, M. Coraiola, *et al.*, "Direct Microwave Spectroscopy of Andreev Bound States in Planar Ge Josephson Junctions," *PRX Quantum*, vol. 5, no. 3, p. 030 357, Sep. 2024, ISSN: 2691-3399. DOI: 10.1103/prxquantum.5.030357.

[29] E. Kiyooka, C. Tangchingchai, L. Noirot, *et al.*, "Gatemon qubit on a germanium quantum-well heterostructure," *Nano Lett.*, vol. 25, no. 1, pp. 562–568, Dec. 2024, ISSN: 1530-6992. DOI: 10.1021/acs.nanolett.4c05539.

[30] L. Lakic, W. I. L. Lawrie, D. van Driel, *et al.*, "A quantum dot in germanium proximitized by a superconductor," *Nat. Mater.*, vol. 24, no. 4, pp. 552–558, Feb. 2025, ISSN: 1476-4660. DOI: 10.1038/s41563-024-02095-5.

[31] C. Morrison and M. Myronov, "Electronic transport anisotropy of 2D carriers in biaxial compressive strained germanium," *Appl. Phys. Lett.*, vol. 111, no. 19, p. 192 103, Nov. 2017, ISSN: 1077-3118. DOI: 10.1063/1.5010933.

[32] M. Lodari, O. Kong, M. Rendell, *et al.*, "Lightly strained germanium quantum wells with hole mobility exceeding one million," *Appl. Phys. Lett.*, vol. 120, no. 12, p. 122 104, Mar. 2022, ISSN: 1077-3118. DOI: 10.1063/5.0083161.

[33] M. Myronov, J. Kycia, P. Waldron, *et al.*, "Holes Outperform Electrons in Group IV Semiconductor Materials," *Small Science*, vol. 3, no. 4, p. 2 200 094, Mar. 2023, ISSN: 2688-4046. DOI: 10.1002/smsc.202200094.

[34] M. Myronov, P. Waldron, P. Barrios, A. Bogan, and S. Studenikin, "Electric field-tuneable crossing of hole Zeeman splitting and orbital gaps in compressively strained germanium semiconductor on silicon," *Commun. Mater.*, vol. 4, no. 1, p. 104, Dec. 2023, ISSN: 2662-4443. DOI: 10.1038/s43246-023-00431-x.

[35] Y. Wang, B. Jazizadeh, Z. Yu, *et al.*, "Impact of quantum well thickness on hole mobility in strained germanium heterostructures," *Appl. Phys. Lett.*, vol. 126, no. 9, p. 092 105, Mar. 2025, ISSN: 1077-3118. DOI: 10.1063/5.0251851.

[36] T. M. Lu, L. A. Tracy, D. Laroche, *et al.*, "Density-controlled quantum Hall ferromagnetic transition in a two-dimensional hole system," *Sci. Rep.*, vol. 7, no. 1, p. 2468, 2017, ISSN: 2045-2322. DOI: 10.1038/s41598-017-02757-2.

[37] M. Failla, J. Keller, G. Scalari, *et al.*, "Terahertz quantum Hall effect for spin-split heavy-hole gases in strained Ge quantum wells," *New J. Phys.*, vol. 18, no. 11, p. 113 036, Nov. 2016, ISSN: 1367-2630. DOI: 10.1088/1367-2630/18/11/113036.

[38] R. Pillarisetty, "Academic and industry research progress in germanium nanodevices," *Nature*, vol. 479, no. 7373, pp. 324–328, Nov. 2011, ISSN: 1476-4687. DOI: 10.1038/nature10678.

[39] N. H. Lindner, E. Berg, G. Refael, and A. Stern, "Fractionalizing Majorana fermions: Non-Abelian statistics on the edges of Abelian quantum Hall states," *Phys. Rev. X*, vol. 2, p. 041 002, 4 Oct. 2012. DOI: 10.1103/PhysRevX.2.041002.

[40] F. Zhang and C. L. Kane, "Time-reversal-invariant $Z_4$ fractional Josephson effect," *Phys. Rev. Lett.*, vol. 113, p. 036 401, 3 Jul. 2014. DOI: 10.1103/PhysRevLett.113.036401.

[41] J. Klinovaja, A. Yacoby, and D. Loss, "Kramers pairs of Majorana fermions and parafermions in fractional topological insulators," *Phys. Rev. B*, vol. 90, no. 15, p. 155 447, Oct. 2014, ISSN: 1550-235X. DOI: 10.1103/physrevb.90.155447.

[42] P. San-Jose, J. L. Lado, R. Aguado, F. Guinea, and J. Fernández-Rossier, "Majorana zero modes in graphene," *Phys. Rev. X*, vol. 5, no. 4, p. 041 042, Dec. 2015, ISSN: 2160-3308. DOI: 10.1103/physrevx.5.041042.

[43] C. Fleckenstein, N. T. Ziani, and B. Trauzettel, "$\mathbb{Z}_4$ parafermions in weakly interacting superconducting constrictions at the helical edge of quantum spin Hall insulators," *Phys. Rev. Lett.*, vol. 122, no. 6, p. 066 801, Feb. 2019. DOI: 10.1103/physrevlett.122.066801.

[44] A. Sammak, D. Sabbagh, N. W. Hendrickx, *et al.*, "Shallow and Undoped Germanium Quantum Wells: A Playground for Spin and Hybrid Quantum Technology," *Adv. Funct. Mater.*, vol. 29, no. 14, p. 1 807 613, Jan. 2019, ISSN: 1616-3028. DOI: 10.1002/adfm.201807613.

[45] M. Baraban, N. E. Bonesteel, and S. H. Simon, "Resources required for topological quantum factoring," *Phys. Rev. A*, vol. 81, p. 062 317, 6 Jun. 2010. DOI: 10.1103/PhysRevA.81.062317.

[46] R. S. K. Mong, D. J. Clarke, J. Alicea, *et al.*, "Universal topological quantum computation from a superconductor-Abelian quantum Hall heterostructure," *Phys. Rev. X*, vol. 4, no. 1, p. 011 036, Mar. 2014, ISSN: 2160-3308. DOI: 10.1103/PhysRevX.4.011036.

[47] H. K. Onnes, "Further experiments with liquid helium. C. On the change of electric resistance of pure metals at very low temperatures etc. IV. The resistance of pure mercury at helium temperatures," *Commun. Phys. Lab. Univ. Leiden*, vol. 12, no. 120b, Apr. 1911.

[48] F. London and H. London, "The electromagnetic equations of the supraconductor," *Proc. R. Soc. London A*, vol. 149, no. 866, pp. 71–88, Mar. 1935, ISSN: 2053-9169. DOI: 10.1098/rspa.1935.0048.

[49] W. Meissner and R. Ochsenfeld, "Ein neuer Effekt bei Eintritt der Supraleitfähigkeit," *Naturwissenschaften*, vol. 21, no. 44, pp. 787–788, Nov. 1933, ISSN: 1432-1904. DOI: 10.1007/bf01504252.

[50] V. L. Ginzburg and L. D. Landau, "On the theory of superconductivity," *Zh. Eksp. Teor. Fiz. (USSR)*, vol. 20, p. 1064, 1950.

[51] E. Maxwell, "Isotope effect in the superconductivity of mercury," *Phys. Rev.*, vol. 78, no. 4, pp. 477–477, May 1950, ISSN: 0031-899X. DOI: 10.1103/physrev.78.477.

[52] C. A. Reynolds, B. Serin, W. H. Wright, and L. B. Nesbitt, "Superconductivity of isotopes of mercury," *Phys. Rev.*, vol. 78, no. 4, pp. 487–487, May 1950, ISSN: 0031-899X. DOI: 10.1103/physrev.78.487.

[53] J. Bardeen, L. N. Cooper, and J. R. Schrieffer, "Microscopic theory of superconductivity," *Phys. Rev.*, vol. 106, no. 1, pp. 162–164, Apr. 1957, ISSN: 0031-899X. DOI: 10.1103/physrev.106.162.

[54] J. Bardeen, L. N. Cooper, and J. R. Schrieffer, "Theory of Superconductivity," *Phys. Rev.*, vol. 108, pp. 1175–1204, 5 Dec. 1957. DOI: 10.1103/PhysRev.108.1175.

[55] N. N. Bogoliubov, "A new method in the theory of superconductivity. I," *Sov. Phys. JETP*, vol. 7, pp. 41–46, 1 Jul. 1958. [Online]. Available: http://jetp.ras.ru/cgi-bin/e/index/r/34/1/p58?a=list.

[56] L. P. Gor'kov, "Microscopic derivation of the Ginzburg–Landau equations in the theory of superconductivity," *Sov. Phys. JETP*, vol. 9, p. 1364, 1959. [Online]. Available: http://jetp.ras.ru/cgi-bin/e/index/e/9/6/p1364?a=list.

[57] A. J. Leggett, "A theoretical description of the new phases of liquid $^3$He," *Rev. Mod. Phys.*, vol. 47, no. 2, pp. 331–414, Apr. 1975, ISSN: 0034-6861. DOI: 10.1103/revmodphys.47.331.

[58] M. K. Wu, J. R. Ashburn, C. J. Torng, *et al.*, "Superconductivity at 93 K in a new mixed-phase Y-Ba-Cu-O compound system at ambient pressure," *Phys. Rev. Lett.*, vol. 58, no. 9, pp. 908–910, Mar. 1987, ISSN: 0031-9007. DOI: 10.1103/physrevlett.58.908.

[59] H. Takahashi, K. Igawa, K. Arii, Y. Kamihara, M. Hirano, and H. Hosono, "Superconductivity at 43 K in an iron-based layered compound $LaO_{1-x}F_xFeAs$," *Nature*, vol. 453, no. 7193, pp. 376–378, Apr. 2008, ISSN: 1476-4687. DOI: 10.1038/nature06972.

[60] W. L. McMillan, "Transition temperature of strong-coupled superconductors," *Phys. Rev.*, vol. 167, pp. 331–344, 2 Mar. 1968. DOI: 10.1103/PhysRev.167.331.

[61] K. Seeger, "Charge and energy transport in a nondegenerate electron gas," in *Semiconductor Physics: An Introduction*. Springer Berlin Heidelberg, 2004, ch. 4, pp. 47–117, ISBN: 9783662098554. DOI: 10.1007/978-3-662-09855-4_4.

[62] L. Landau, "Diamagnetismus der Metalle," *Z. Phys.*, vol. 64, no. 9, pp. 629–637, Sep. 1930, ISSN: 0044-3328. DOI: 10.1007/bf01397213.

[63] R. Landauer, "Spatial variation of currents and fields due to localized scatterers in metallic conduction," *IBM J. Res. Dev.*, vol. 1, no. 3, pp. 223–231, Jul. 1957, ISSN: 0018-8646. DOI: 10.1147/rd.13.0223.

[64] K. v. Klitzing, G. Dorda, and M. Pepper, "New method for high-accuracy determination of the fine-structure constant based on quantized Hall resistance," *Phys. Rev. Lett.*, vol. 45, pp. 494–497, 6 Aug. 1980. DOI: 10.1103/PhysRevLett.45.494.

[65] P. W. Anderson, "Absence of diffusion in certain random lattices," *Phys. Rev.*, vol. 109, no. 5, pp. 1492–1505, Mar. 1958, ISSN: 0031-899X. DOI: 10.1103/physrev.109.1492.

[66] I. M. Lifshitz, "Energy spectrum structure and quantum states of disordered condensed systems," *Sov. Phys. Usp.*, vol. 7, no. 4, pp. 549–573, Apr. 1965, ISSN: 0038-5670. DOI: 10.1070/pu1965v007n04abeh003634.

[67] H. Aoki and T. Ando, "Critical localization in two-dimensional Landau quantization," *Phys. Rev. Lett.*, vol. 54, no. 8, pp. 831–834, Feb. 1985, ISSN: 0031-9007. DOI: 10.1103/physrevlett.54.831.

[68] F. Wegner, "Exact density of states for lowest Landau level in white noise potential superfield representation for interacting systems," *Z. Phys. B Condens. Matter*, vol. 51, no. 4, pp. 279–285, Dec. 1983, ISSN: 1434-6036. DOI: 10.1007/bf01319209.

[69] E. Brézin, D. J. Gross, and C. Itzykson, "Density of states in the presence of a strong magnetic field and random impurities," *Nucl. Phys. B*, vol. 235, no. 1, pp. 24–44, May 1984, ISSN: 0550-3213. DOI: 10.1016/0550-3213(84)90146-9.

[70] W. Poirier, S. Djordjevic, F. Schopfer, and O. Thévenot, "The ampere and the electrical units in the quantum era," *C. R. Phys.*, vol. 20, no. 1–2, pp. 92–128, Jan. 2019, ISSN: 1631-0705. DOI: 10.1016/j.crhy.2019.02.003.

[71] R. B. Laughlin, "Quantized Hall conductivity in two dimensions," *Phys. Rev. B*, vol. 23, no. 10, pp. 5632–5633, May 1981, ISSN: 0163-1829. DOI: 10.1103/physrevb.23.5632.

[72] B. I. Halperin, "Quantized Hall conductance, current-carrying edge states, and the existence of extended states in a two-dimensional disordered potential," *Phys. Rev. B*, vol. 25, no. 4, pp. 2185–2190, Feb. 1982, ISSN: 0163-1829. DOI: 10.1103/physrevb.25.2185.

[73] K. Hashimoto, C. Sohrmann, J. Wiebe, *et al.*, "Quantum Hall transition in real space: From localized to extended states," *Phys. Rev. Lett.*, vol. 101, no. 25, p. 256 802, Dec. 2008, ISSN: 1079-7114. DOI: 10.1103/physrevlett.101.256802.

[74] K. Hashimoto, T. Champel, S. Florens, *et al.*, "Robust nodal structure of Landau level wave functions revealed by Fourier transform scanning tunneling spectroscopy," *Phys. Rev. Lett.*, vol. 109, no. 11, p. 116 805, Sep. 2012, ISSN: 1079-7114. DOI: 10.1103/physrevlett.109.116805.

[75] B. Huckestein, "Scaling theory of the integer quantum Hall effect," *Rev. Mod. Phys.*, vol. 67, no. 2, pp. 357–396, Apr. 1995, ISSN: 1539-0756. DOI: 10.1103/revmodphys.67.357.

[76] J. M. Kosterlitz and D. J. Thouless, "Ordering, metastability and phase transitions in two-dimensional systems," *J. Phys. C: Solid State Phys.*, vol. 6, no. 7, pp. 1181–1203, 1973. DOI: 10.1088/0022-3719/6/7/010.

[77] N. Leconte, F. Ortmann, A. Cresti, and S. Roche, "Unconventional features in the quantum Hall regime of disordered graphene: Percolating impurity states and Hall conductance quantization," *Phys. Rev. B*, vol. 93, no. 11, p. 115 404, Mar. 2016, ISSN: 2469-9969. DOI: 10.1103/physrevb.93.115404.

[78] F. D. M. Haldane, "Model for a quantum Hall effect without Landau levels: Condensed-matter realization of the "parity anomaly"," *Phys. Rev. Lett.*, vol. 61, no. 18, pp. 2015–2018, Oct. 1988, ISSN: 0031-9007. DOI: 10.1103/physrevlett.61.2015.

[79] D. J. Thouless, M. Kohmoto, M. P. Nightingale, and M. den Nijs, "Quantized Hall conductance in a two-dimensional periodic potential," *Phys. Rev. Lett.*, vol. 49, no. 6, pp. 405–408, Aug. 1982, ISSN: 0031-9007. DOI: 10.1103/physrevlett.49.405.

[80] D. C. Tsui, H. L. Stormer, and A. C. Gossard, "Two-dimensional magnetotransport in the extreme quantum limit," *Phys. Rev. Lett.*, vol. 48, no. 22, pp. 1559–1562, May 1982, ISSN: 0031-9007. DOI: 10.1103/physrevlett.48.1559.

[81] J. P. Eisenstein, G. S. Boebinger, L. N. Pfeiffer, K. W. West, and S. He, "New fractional quantum Hall state in double-layer two-dimensional electron systems," *Phys. Rev. Lett.*, vol. 68, no. 9, pp. 1383–1386, Mar. 1992, ISSN: 0031-9007. DOI: 10.1103/physrevlett.68.1383.

[82] J. Shabani, T. Gokmen, Y. T. Chiu, and M. Shayegan, "Evidence for developing fractional quantum hall states at even denominator 1/2 and 1/4 fillings in asymmetric wide quantum wells," *Phys. Rev. Lett.*, vol. 103, no. 25, p. 256 802, Dec. 2009, ISSN: 1079-7114. DOI: 10.1103/physrevlett.103.256802.

[83] W. Pan, H. L. Stormer, D. C. Tsui, L. N. Pfeiffer, K. W. Baldwin, and K. W. West, "Transition from an electron solid to the sequence of fractional quantum Hall states at very low Landau level filling factor," *Phys. Rev. Lett.*, vol. 88, no. 17, p. 176 802, Apr. 2002, ISSN: 1079-7114. DOI: 10.1103/physrevlett.88.176802.

[84] D. R. Hartree, "The wave mechanics of an atom with a non-Coulomb central field. Part I. theory and methods," *Math. Proc. Camb. Philos. Soc.*, vol. 24, no. 1, pp. 89–110, Jan. 1928, ISSN: 1469-8064. DOI: 10.1017/s0305004100011919.

[85] V. Fock, "Näherungsmethode zur Lösung des quantenmechanischen Mehrkörperproblems," *Z. Phys.*, vol. 61, no. 1, pp. 126–148, Jan. 1930, ISSN: 0044-3328. DOI: 10.1007/bf01340294.

[86] S. A. Trugman and S. Kivelson, "Exact results for the fractional quantum Hall effect with general interactions," *Phys. Rev. B*, vol. 31, no. 8, pp. 5280–5284, Apr. 1985, ISSN: 0163-1829. DOI: 10.1103/physrevb.31.5280.

[87] R. B. Laughlin, "Anomalous quantum Hall effect: An incompressible quantum fluid with fractionally charged excitations," *Phys. Rev. Lett.*, vol. 50, no. 18, pp. 1395–1398, May 1983, ISSN: 0031-9007. DOI: 10.1103/physrevlett.50.1395.

[88] G. Moore and N. Read, "Nonabelions in the fractional quantum Hall effect," *Nucl. Phys. B*, vol. 360, no. 2 - 3, pp. 362–396, 1991, ISSN: 0550-3213. DOI: 10.1016/0550-3213(91)90407-O.

[89] B. I. Halperin, P. A. Lee, and N. Read, "Theory of the half-filled Landau level," *Phys. Rev. B*, vol. 47, no. 12, pp. 7312–7343, Mar. 1993, ISSN: 1095-3795. DOI: 10.1103/physrevb.47.7312.

[90] J. K. Jain, "Composite Fermion approach for the fractional quantum Hall effect," *Phys. Rev. Lett.*, vol. 63, no. 2, pp. 199–202, Jul. 1989, ISSN: 0031-9007. DOI: 10.1103/physrevlett.63.199.

[91] B. I. Halperin, "Theory of the quantized Hall conductance," *Helv. Phys. Acta*, vol. 56, no. 1-3, pp. 75–102, Jan. 1983, ISSN: 0018-0238. DOI: 10.5169/seals-115362.

[92] M. Virgilio and G. Grosso, "Type-I alignment and direct fundamental gap in SiGe based heterostructures," *J. Phys.: Condens. Matter*, vol. 18, no. 3, pp. 1021–1031, Jan. 2006, ISSN: 1361-648X. DOI: 10.1088/0953-8984/18/3/018.

[93] M. Myronov, "Molecular Beam Epitaxy of High Mobility Silicon, Silicon Germanium and Germanium Quantum Well Heterostructures," in *Molecular Beam Epitaxy*, M. Henini, Ed., 2nd ed. Elsevier, 2018, ch. 3, pp. 37–54, ISBN: 9780128121368. DOI: 10.1016/b978-0-12-812136-8.00003-7.

[94] P. Zeeman, "The effect of magnetisation on the nature of light emitted by a substance," *Nature*, vol. 55, no. 1424, pp. 347–347, Feb. 1897, ISSN: 1476-4687. DOI: 10.1038/055347a0.

[95] R. J. Nicholas, M. A. Brummell, J. C. Portal, K. Y. Cheng, A. Y. Cho, and T. P. Pearsall, "An experimental determination of enhanced electron g-factors in GaInAs-AlInAs heterojunctions," *Solid State Commun.*, vol. 45, no. 10, pp. 911–914, Mar. 1983, ISSN: 0038-1098. DOI: 10.1016/0038-1098(83)90334-4.

[96] J. L. Smith and P. J. Stiles, "Electron-electron interactions continuously variable in the range $2.1 > r_s > 0.9$," *Phys. Rev. Lett.*, vol. 29, no. 2, pp. 102–104, Jul. 1972, ISSN: 0031-9007. DOI: 10.1103/physrevlett.29.102.

[97] T. Ando and Y. Uemura, "Theory of oscillatory $g$ factor in an MOS inversion layer under strong magnetic fields," *J. Phys. Soc. Jpn.*, vol. 37, no. 4, pp. 1044–1052, Oct. 1974, ISSN: 1347-4073. DOI: 10.1143/jpsj.37.1044.

[98] T. Englert, D. Tsui, A. Gossard, and C. Uihlein, "$g$-Factor enhancement in the 2D electron gas in GaAs/AlGaAs heterojunctions," *Surf. Sci.*, vol. 113, no. 1–3, pp. 295–300, Jan. 1982, ISSN: 0039-6028. DOI: 10.1016/0039-6028(82)90604-5.

[99] T. Jungwirth and A. H. MacDonald, "Resistance spikes and domain wall loops in Ising quantum Hall ferromagnets," *Phys. Rev. Lett.*, vol. 87, no. 21, p. 216 801, Oct. 2001, ISSN: 1079-7114. DOI: 10.1103/physrevlett.87.216801.

[100] J. Jaroszyński, T. Andrearczyk, G. Karczewski, *et al.*, "Ising quantum Hall ferromagnet in magnetically doped quantum wells," *Phys. Rev. Lett.*, vol. 89, p. 266 802, 26 Dec. 2002. DOI: 10.1103/PhysRevLett.89.266802.

[101] A. Kazakov, G. Simion, Y. Lyanda-Geller, *et al.*, "Electrostatic control of quantum Hall ferromagnetic transition: A step toward reconfigurable network of helical channels," *Phys. Rev. B*, vol. 94, p. 075 309, 7 2016. DOI: 10.1103/PhysRevB.94.075309.

[102] A. Kazakov, G. Simion, Y. Lyanda-Geller, *et al.*, "Mesoscopic transport in electrostatically defined spin-full channels in quantum Hall ferromagnets," *Phys. Rev. Lett.*, vol. 119, no. 4, p. 046 803, 4 Jul. 2017, ISSN: 0031-9007. DOI: 10.1103/PhysRevLett.119.046803.

[103] Y. Wang, V. Ponomarenko, Z. Wan, *et al.*, "Transport in helical Luttinger liquids in the fractional quantum Hall regime," *Nat. Commun.*, vol. 12, no. 1, p. 5312, Sep. 2021. DOI: 10.1038/s41467-021-25631-2.

[104] D. J. Clarke, J. Alicea, and K. Shtengel, "Exotic non-Abelian anyons from conventional fractional quantum Hall states," *Nat. Commun.*, vol. 4, no. 1, p. 1348, Jan. 2013, ISSN: 2041-1723. DOI: 10.1038/ncomms2340.

[105] Z. Wan, A. Kazakov, M. J. Manfra, L. N. Pfeiffer, K. W. West, and L. P. Rokhinson, "Induced superconductivity in high-mobility two-dimensional electron gas in gallium arsenide heterostructures," *Nat. Commun.*, vol. 6, no. 1, p. 7426, Jun. 2015, ISSN: 2041-1723. DOI: 10.1038/ncomms8426.

[106] J. M. Luttinger, "Quantum theory of cyclotron resonance in semiconductors: General theory," *Phys. Rev.*, vol. 102, no. 4, pp. 1030–1041, May 1956, ISSN: 0031-899X. DOI: 10.1103/physrev.102.1030.

[107] T. Irisawa, M. Myronov, O. A. Mironov, *et al.*, "Hole density dependence of effective mass, mobility and transport time in strained Ge channel modulation-doped heterostructures," *Appl. Phys. Lett.*, vol. 82, no. 9, pp. 1425–1427, Feb. 2003, ISSN: 1077-3118. DOI: 10.1063/1.1558895.

[108] B. Rößner, G. Isella, and H. v. Känel, "Effective mass in remotely doped Ge quantum wells," *Appl. Phys. Lett.*, vol. 82, no. 5, pp. 754–756, Jan. 2003, ISSN: 1077-3118. DOI: 10.1063/1.1541101.

[109] K. Sawano, Y. Kunishi, Y. Satoh, *et al.*, "On effects of gate bias on hole effective mass and mobility in strained-Ge channel structures," *Appl. Phys. Express*, vol. 1, no. 1, p. 011 401, Jan. 2008, ISSN: 1882-0786. DOI: 10.1143/apex.1.011401.

[110] I. L. Drichko, A. A. Dmitriev, V. A. Malysh, *et al.*, "Effective g factor of 2D holes in strained Ge quantum wells," *J. Appl. Phys.*, vol. 123, no. 16, Apr. 2018, ISSN: 1089-7550. DOI: 10.1063/1.5025413.

[111] A. Tsukazaki, A. Ohtomo, M. Kawasaki, *et al.*, "Spin susceptibility and effective mass of two-dimensional electrons in $Mg_xZn_{1-x}O$/ZnO heterostructures," *Phys. Rev. B*, vol. 78, no. 23, p. 233 308, Dec. 2008, ISSN: 1550-235X. DOI: 10.1103/physrevb.78.233308.

[112] D. Maryenko, M. Kawamura, A. Ernst, *et al.*, "Interplay of spin–orbit coupling and Coulomb interaction in ZnO-based electron system," *Nat. Commun.*, vol. 12, no. 1, p. 3180, May 2021, ISSN: 2041-1723. DOI: 10.1038/s41467-021-23483-4.

[113] K. Sawano, Y. Kunishi, Y. Shiraki, *et al.*, "Magnetotransport properties of Ge channels with extremely high compressive strain," *Appl. Phys. Lett.*, vol. 89, no. 16, p. 162 103, Oct. 2006, ISSN: 1077-3118. DOI: 10.1063/1.2354467.

[114] K. Sawano, K. Toyama, R. Masutomi, *et al.*, "Strain dependence of hole effective mass and scattering mechanism in strained Ge channel structures," *Appl. Phys. Lett.*, vol. 95, no. 12, p. 122 109, Sep. 2009, ISSN: 1077-3118. DOI: 10.1063/1.3229998.

[115] A. Andreev, "The thermal conductivity of the intermediate state in superconductors," *Sov. Phys. JETP*, vol. 19, no. 5, p. 1228, Nov. 1964. [Online]. Available: http://jetp.ras.ru/cgi-bin/e/index/e/19/5/p1228?a=list.

[116] G. Deutscher and D. Feinberg, "Coupling superconducting-ferromagnetic point contacts by Andreev reflections," *Appl. Phys. Lett.*, vol. 76, no. 4, pp. 487–489, Jan. 2000, ISSN: 1077-3118. DOI: 10.1063/1.125796.

[117] R. Holm and W. Meissner, "Messungen mit Hilfe von flüssigem Helium. XIII: Kontaktwiderstand zwischen Supraleitern und Nichtsupraleitern," *Z. Phys.*, vol. 74, no. 11–12, pp. 715–735, Nov. 1932, ISSN: 1434-601X. DOI: 10.1007/bf01340420.

[118] H. Meissner, "Superconductivity of contacts with interposed barriers," *Phys. Rev.*, vol. 117, no. 3, pp. 672–680, Feb. 1960, ISSN: 0031-899X. DOI: 10.1103/physrev.117.672.

[119] G. E. Blonder, M. Tinkham, and T. M. Klapwijk, "Transition from metallic to tunneling regimes in superconducting microconstrictions: Excess current, charge imbalance, and supercurrent conversion," *Phys. Rev. B*, vol. 25, pp. 4515–4532, 7 Apr. 1982. DOI: 10.1103/PhysRevB.25.4515.

[120] R. C. Dynes, V. Narayanamurti, and J. P. Garno, "Direct measurement of quasiparticle-lifetime broadening in a strong-coupled superconductor," *Phys. Rev. Lett.*, vol. 41, no. 21, pp. 1509–1512, Nov. 1978, ISSN: 0031-9007. DOI: 10.1103/physrevlett.41.1509.

[121] H. Hoppe, U. Zülicke, and G. Schön, "Andreev reflection in strong magnetic fields," *Phys. Rev. Lett.*, vol. 84, no. 8, pp. 1804–1807, Feb. 2000, ISSN: 0031-9007. DOI: 10.1103/PhysRevLett.84.1804.

[122] T. W. Nee and R. E. Prange, "Quantum spectroscopy of the low field oscillations of the surface impedance," *Phys. Lett. A*, vol. 25, no. 8, pp. 582–583, Oct. 1967, ISSN: 0375-9601. DOI: 10.1016/0375-9601(67)90270-8.

[123] R. E. Prange and T.-W. Nee, "Quantum spectroscopy of the low-field oscillations in the surface impedance," *Phys. Rev.*, vol. 168, no. 3, pp. 779–786, Apr. 1968, ISSN: 0031-899X. DOI: 10.1103/physrev.168.779.

[124] A. G. Aronov and A. S. loselevich, "Absorption of obliquely incident sound in the intermediate state," *Sov. Phys. JETP*, vol. 47, no. 2, pp. 305–311, Feb. 1978. [Online]. Available: http://www.jetp.ras.ru/cgi-bin/e/index/e/47/2/p305?a=list.

[125] I. O. Kulik, "Macroscopic quantization and the proximity effect in S-N-S junctions," *Sov. Phys. JETP*, vol. 30, no. 5, pp. 944–950, May 1970. [Online]. Available: http://www.jetp.ras.ru/cgi-bin/e/index/e/30/5/p944?a=list.

[126] M. Büttiker, "Absence of backscattering in the quantum Hall effect in multiprobe conductors," *Phys. Rev. B*, vol. 38, no. 14, pp. 9375–9389, Nov. 1988, ISSN: 0163-1829. DOI: 10.1103/physrevb.38.9375.

[127] H. Takayanagi and T. Akazaki, "Semiconductor-coupled superconducting junctions using NbN electrodes with high $H_{c2}$ and $T_c$," *Physica B*, vol. 249–251, pp. 462–466, Jun. 1998, ISSN: 0921-4526. DOI: 10.1016/s0921-4526(98)00164-1.

[128] T. D. Moore and D. A. Williams, "Andreev reflection at high magnetic fields," *Phys. Rev. B*, vol. 59, pp. 7308–7311, 11 Mar. 1999. DOI: 10.1103/PhysRevB.59.7308.

[129] P. Rickhaus, M. Weiss, L. Marot, and C. Schönenberger, "Quantum Hall effect in graphene with superconducting electrodes," *Nano Lett.*, vol. 12, no. 4, pp. 1942–1945, Mar. 2012, ISSN: 1530-6992. DOI: 10.1021/nl204415s.

[130] K. Komatsu, C. Li, S. Autier-Laurent, H. Bouchiat, and S. Guéron, "Superconducting proximity effect in long superconductor/graphene/superconductor junctions: From specular Andreev reflection at zero field to the quantum Hall regime," *Phys. Rev. B*, vol. 86, no. 11, p. 115 412, Sep. 2012, ISSN: 1550-235X. DOI: 10.1103/physrevb.86.115412.

[131] F. Amet, C. T. Ke, I. V. Borzenets, *et al.*, "Supercurrent in the quantum Hall regime," *Science*, vol. 352, no. 6288, pp. 966–969, May 2016, ISSN: 1095-9203. DOI: 10.1126/science.aad6203.

[132] G.-H. Park, M. Kim, K. Watanabe, T. Taniguchi, and H.-J. Lee, "Propagation of superconducting coherence via chiral quantum-Hall edge channels," *Sci. Rep.*, vol. 7, no. 1, p. 10 953, Sep. 2017, ISSN: 2045-2322. DOI: 10.1038/s41598-017-11209-w.

[133] L. Zhao, E. G. Arnault, A. Bondarev, *et al.*, "Interference of chiral Andreev edge states," *Nat. Phys.*, vol. 16, no. 8, pp. 862–867, May 2020, ISSN: 1745-2481. DOI: 10.1038/s41567-020-0898-5.

[134] D. Wang, E. J. Telford, A. Benyamini, *et al.*, "Andreev reflections in NbN/graphene junctions under large magnetic fields," *Nano Lett.*, vol. 21, no. 19, pp. 8229–8235, Sep. 2021, ISSN: 1530-6992. DOI: 10.1021/acs.nanolett.1c02020.

[135] M. Hatefipour, J. J. Cuozzo, J. Kanter, *et al.*, "Induced superconducting pairing in integer quantum Hall edge states," *Nano Lett.*, vol. 22, no. 15, pp. 6173–6178, Jul. 2022, ISSN: 1530-6992. DOI: 10.1021/acs.nanolett.2c01413.

[136] Y. Kozuka, A. Sakaguchi, J. Falson, A. Tsukazaki, and M. Kawasaki, "Andreev reflection at the interface with an oxide in the quantum Hall regime," *J. Phys. Soc. Jpn.*, vol. 87, no. 12, p. 124 712, Dec. 2018, ISSN: 1347-4073. DOI: 10.7566/jpsj.87.124712.

[137] D. J. Clarke, J. Alicea, and K. Shtengel, "Exotic circuit elements from zero-modes in hybrid superconductor-quantum-Hall systems," *Nat. Phys.*, vol. 10, no. 11, pp. 877–882, Nov. 2014, ISSN: 1745-2473. DOI: 10.1038/nphys3114.

[138] G.-H. Lee, K.-F. Huang, D. K. Efetov, *et al.*, "Inducing superconducting correlation in quantum Hall edge states," *Nat. Phys.*, vol. 13, no. 7, pp. 693–698, Apr. 2017, ISSN: 1745-2481. DOI: 10.1038/nphys4084.

[139] Ö. Gül, Y. Ronen, S. Y. Lee, *et al.*, "Andreev reflection in the fractional quantum Hall state," *Phys. Rev. X*, vol. 12, no. 2, p. 021 057, Jun. 2022, ISSN: 2160-3308. DOI: 10.1103/physrevx.12.021057.

[140] D. Laroche, S.-H. Huang, Y. Chuang, J.-Y. Li, C. W. Liu, and T. M. Lu, "Magneto-transport analysis of an ultra-low-density two-dimensional hole gas in an undoped strained Ge/SiGe heterostructure," *Appl. Phys. Lett.*, vol. 108, no. 23, p. 233 504, Jun. 2016, ISSN: 1077-3118. DOI: 10.1063/1.4953399.

[141] D. Monroe, Y. H. Xie, E. A. Fitzgerald, P. J. Silverman, and G. P. Watson, "Comparison of mobility-limiting mechanisms in high-mobility $Si_{1-x}Ge_x$ heterostructures," *J. Vac. Sci. Technol. B*, vol. 11, no. 4, pp. 1731–1737, Jul. 1993, ISSN: 1520-8567. DOI: 10.1116/1.586471.

[142] F. Schäffler, "High-mobility Si and Ge structures," *Semicond. Sci. Tech.*, vol. 12, no. 12, pp. 1515–1549, Dec. 1997, ISSN: 1361-6641. DOI: 10.1088/0268-1242/12/12/001.

[143] X. Lefèvre, O. Segut, P. Jégou, S. Palacin, and B. Jousselme, "Towards organic film passivation of germanium wafers using diazonium salts: Mechanism and ambient stability," *Chem. Sci.*, vol. 3, no. 5, pp. 1662–1671, Apr. 2012, ISSN: 2041-6539. DOI: 10.1039/c2sc01034h.

[144] M. Mann, J. Nakamura, S. Liang, T. Maiti, R. Diaz, and M. J. Manfra, "Optimization of submicron Ni/Au/Ge contacts to an AlGaAs/GaAs two-dimensional electron gas," *Appl. Phys. Lett.*, vol. 125, no. 7, p. 073 503, Aug. 2024, ISSN: 1077-3118. DOI: 10.1063/5.0222647.

[145] J. Kim, J. McVittie, K. Saraswat, Y. Nishi, S. Liu, and S. Tan, "Germanium surface cleaning with hydrochloric acid," *ECS Trans.*, vol. 3, no. 7, pp. 1191–1196, Oct. 2006, ISSN: 1938-6737. DOI: 10.1149/1.2355913.

[146] S. Sioncke, Y. J. Chabal, and M. M. Frank, "Germanium surface conditioning and passivation," in R. F. R. Karen A. Reinhardt, Ed. Wiley, Dec. 2010, ch. 12, pp. 429–472, ISBN: 9781118071748. DOI: 10.1002/9781118071748.ch12.

[147] P. Ponath, A. B. Posadas, and A. A. Demkov, "Ge(001) surface cleaning methods for device integration," *Appl. Phys. Rev.*, vol. 4, no. 2, p. 021 308, Jun. 2017, ISSN: 1931-9401. DOI: 10.1063/1.4984975.

[148] G. K. Chang, T. K. Carns, S. S. Rhee, and K. L. Wang, "Selective etching of SiGe on SiGe/Si heterostructures," *J. Electrochem. Soc.*, vol. 138, no. 1, pp. 202–204, Jan. 1991, ISSN: 1945-7111. DOI: 10.1149/1.2085539.

[149] T. K. Cams, M. O. Tanner, and K. L. Wang, "Chemical etching of $Si_{1-x}Ge_x$ in $HF:H_2O_2:CH_3COOH$," *J. Electrochem. Soc.*, vol. 142, no. 4, pp. 1260–1266, Apr. 1995, ISSN: 1945-7111. DOI: 10.1149/1.2044161.

[150] B. Holländer, D. Buca, S. Mantl, and J. M. Hartmann, "Wet chemical etching of Si, $Si_{1-x}Ge_x$, and Ge in $HF:H_2O_2:CH_3COOH$," *J. Electrochem. Soc.*, vol. 157, no. 6, H643, 2010, ISSN: 0013-4651. DOI: 10.1149/1.3382944.

[151] Z. Baraissov, A. Pacco, S. Koneti, *et al.*, "Selective wet etching of silicon germanium in composite vertical nanowires," *ACS Appl. Mater. Interfaces*, vol. 11, no. 40, pp. 36 839–36 846, Sep. 2019, ISSN: 1944-8252. DOI: 10.1021/acsami.9b11934.

[152] K. Saidov, Z. Aabdin, H. Yan, A. Pacco, F. Holsteyns, and U. Mirsaidov, "Controlling etch anisotropy of crystalline germanium nanostructures," *Small*, vol. 21, no. 40, Aug. 2025, ISSN: 1613-6829. DOI: 10.1002/smll.202504357.

[153] G. H. A. Abrenica, M. Fingerle, M. V. Lebedev, *et al.*, "Wet chemical processing of Ge in acidic $H_2O_2$ solution: Nanoscale etching and surface chemistry," *ECS J. Solid State Sci. Technol.*, vol. 9, no. 8, p. 084 002, Jan. 2020, ISSN: 2162-8777. DOI: 10.1149/2162-8777/abb1c5.

[154] Marvell NanoLab at CITRIS. (n.d.), *Miscellaneous Etchants.* Retieved November 7, 2025 from https://nanolab.berkeley.edu/labmanual/chap1/1.10miscetch.pdf.

[155] N. Cerniglia and P. Wang, "Dissolution of germanium in aqueous hydrogen peroxide solution," *J. Electrochem. Soc.*, vol. 109, no. 6, p. 508, 1962, ISSN: 0013-4651. DOI: 10.1149/1.2425457.

[156] I. M. Huygens, W. P. Gomes, and K. Strubbe, "Etching of germanium in hydrogenperoxide solutions," *ECS Trans.*, vol. 6, no. 2, pp. 375–386, Apr. 2007, ISSN: 1938-6737. DOI: 10.1149/1.2731205.

[157] A. Chawanda, K. T. Roro, F. D. Auret, *et al.*, "Determination of the laterally homogeneous barrier height of palladium Schottky barrier diodes on n-Ge (1 1 1)," *Mat. Sci. Semicon. Proc.*, vol. 13, no. 5–6, pp. 371–375, Dec. 2010, ISSN: 1369-8001. DOI: 10.1016/j.mssp.2011.05.001.

[158] A. Chawanda, S. M. M. Coelho, F. D. Auret, *et al.*, "Effect of thermal treatment on the characteristics of iridium Schottky barrier diodes on n-Ge (100)," *J. Alloy. Compd.*, vol. 513, pp. 44–49, Feb. 2012, ISSN: 0925-8388. DOI: 10.1016/j.jallcom.2011.09.053.

[159] A. Chawanda, C. Nyamhere, F. D. Auret, J. M. Nel, W. Mtangi, and M. Diale, "Electrical characterisation of ruthenium Schottky contacts on n-Ge (100)," *Physica B*, vol. 407, no. 10, pp. 1570–1573, May 2012, ISSN: 0921-4526. DOI: 10.1016/j.physb.2011.09.088.

[160] A. K. Rumaiz, C. Weiland, I. Harding, *et al.*, "Interface formation and Schottky barrier height for Y, Nb, Au, and Pt on Ge as determined by hard x-ray photoelectron spectroscopy," *AIP Adv.*, vol. 13, no. 1, Jan. 2023, ISSN: 2158-3226. DOI: 10.1063/5.0101688.

[161] C. Wongwanitwattana, V. A. Shah, M. Myronov, E. H. C. Parker, T. Whall, and D. R. Leadley, "Precision plasma etching of Si, Ge, and Ge:P by $SF_6$ with added $O_2$," *J. Vac. Sci. Technol. A*, vol. 32, no. 3, Mar. 2014, ISSN: 1520-8559. DOI: 10.1116/1.4868615.

[162] K.-H. Shim, Y.-H. Kil, H. D. Yang, *et al.*, "Characteristics of germanium dry etching using inductively coupled $SF_6$ plasma," *Mat. Sci. Semicon. Proc.*, vol. 15, no. 4, pp. 364–370, Aug. 2012, ISSN: 1369-8001. DOI: 10.1016/j.mssp.2011.12.002.

[163] L. J. van der Pauw, "A method of measuring the resistivity and Hall coefficient on lamellae of arbitrary shape," *Philips Tech. Rev.*, vol. 20, no. 8, pp. 220–224, 1958.

[164] L. Massai, B. Hetényi, M. Mergenthaler, *et al.*, "Impact of interface traps on charge noise and low-density transport properties in Ge/SiGe heterostructures," *Commun. Mater.*, vol. 5, no. 1, p. 151, Aug. 2024, ISSN: 2662-4443. DOI: 10.1038/s43246-024-00563-8.

[165] H. Wu, W. Wu, M. Si, and P. D. Ye, "Demonstration of Ge nanowire CMOS devices and circuits for ultimate scaling," *IEEE Trans. Electron Devices*, vol. 63, no. 8, pp. 3049–3057, Aug. 2016, ISSN: 1557-9646. DOI: 10.1109/ted.2016.2581862.

[166] C. Lavoie, P. Adusumilli, A. V. Carr, *et al.*, "(Invited) Contacts in Advanced CMOS: History and Emerging Challenges," *ECS Trans.*, vol. 77, no. 5, pp. 59–79, Apr. 2017, ISSN: 1938-5862. DOI: 10.1149/07705.0059ecst.

[167] B. T. Matthias, T. H. Geballe, and V. B. Compton, "Superconductivity," *Rev. Mod. Phys.*, vol. 35, no. 1, pp. 1–22, Jan. 1963, ISSN: 0034-6861. DOI: 10.1103/revmodphys.35.1.

[168] C. J. Raub, W. H. Zachariasen, T. H. Geballe, and B. T. Matthias, "Superconductivity of some new Pt-metal compounds," *J. Phys. Chem. Solids*, vol. 24, no. 9, pp. 1093–1100, Sep. 1963, ISSN: 0022-3697. DOI: 10.1016/0022-3697(63)90022-2.

[169] B. W. Roberts, "Survey of superconductive materials and critical evaluation of selected properties," *J. Phys. Chem. Ref. Data*, vol. 5, no. 3, pp. 581–822, Jul. 1976, ISSN: 1529-7845. DOI: 10.1063/1.555540.

[170] A. K. Ghosh and D. H. Douglass, "Superconductivity in transition metal-germanium systems," *J. Low Temp. Phys.*, vol. 27, no. 3–4, pp. 487–512, May 1977, ISSN: 1573-7357. DOI: 10.1007/bf00655283.

[171] C. M. Knoedler and D. H. Douglass, "Superconductivity in $NbGe_2$ and isostructural C-40 compounds," *J. Low Temp. Phys.*, vol. 37, no. 1–2, pp. 189–218, Oct. 1979, ISSN: 1573-7357. DOI: 10.1007/bf00114067.

[172] C. J. Raub, "Superconductivity of the platinum metals and their alloys," *Mater. Des.*, vol. 5, no. 3, pp. 129–136, Jun. 1984, ISSN: 0261-3069. DOI: 10.1016/0261-3069(84)90081-5.

[173] D. Hirai, M. N. Ali, and R. J. Cava, "Strong Electron-Phonon Coupling Superconductivity Induced by a Low-Lying Phonon in IrGe," *J. Phys. Soc. Jpn.*, vol. 82, no. 12, p. 124 701, Dec. 2013, ISSN: 1347-4073. DOI: 10.7566/jpsj.82.124701.

[174] D. Zhang, T. Le, B. Lv, *et al.*, "Full superconducting gap and type-I to type-II superconductivity transition in single crystalline $NbGe_2$," *Phys. Rev. B*, vol. 103, no. 21, p. 214 508, Jun. 2021, ISSN: 2469-9969. DOI: 10.1103/physrevb.103.214508.

[175] Arushi, K. Motla, P. K. Meena, *et al.*, "Microscopic investigation of the superconducting properties of the strongly coupled superconductor IrGe via $\mu$SR," *Phys. Rev. B*, vol. 105, no. 5, p. 054 517, Feb. 2022, ISSN: 2469-9969. DOI: 10.1103/physrevb.105.054517.

[176] N. Nakamura, A. Yanuma, Y. Chiba, *et al.*, "Fermi Surface and Superconducting Properties of $\alpha$-$IrSn_4$, $\alpha$-$RhSn_4$, $IrGe_4$, and $RhGe_4$ with Trigonal Chiral Structure," *J. Phys. Soc. Jpn.*, vol. 92, no. 3, p. 034 701, Mar. 2023, ISSN: 1347-4073. DOI: 10.7566/jpsj.92.034701.

[177] P. J. Strohbeen, T. Banerjee, A. M. Brook, *et al.*, "Molecular beam epitaxy growth of superconducting tantalum germanide," *Appl. Phys. Lett.*, vol. 124, no. 9, p. 092 102, Feb. 2024, ISSN: 1077-3118. DOI: 10.1063/5.0189597.

[178] S. Gaudet, C. Detavernier, A. J. Kellock, P. Desjardins, and C. Lavoie, "Thin film reaction of transition metals with germanium," *J. Vac. Sci. Technol. A*, vol. 24, no. 3, pp. 474–485, Apr. 2006, ISSN: 1520-8559. DOI: 10.1116/1.2191861.

[179] Z. Li, W.-W. Yang, J.-J. Feng, *et al.*, "Type-I superconductivity in the Weyl semimetal $TaGe_2$ with chiral structure," *Phys. Rev. B*, vol. 110, no. 17, p. 174 506, Nov. 2024, ISSN: 2469-9969. DOI: 10.1103/physrevb.110.174506.

[180] A. Habanyama and C. M. Comrie, "Inter-Diffusion of Iridium, Platinum, Palladium and Rhodium with Germanium: Improved materials for the next generation of electronic devices," *Johnson Matthey Technol. Rev.*, vol. 62, no. 2, pp. 211–230, Apr. 2018, ISSN: 2056-5135. DOI: 10.1595/205651318x696639.

[181] M. Wittmer, M.-A. Nicolet, and J. W. Mayer, "The first phase to nucleate in planar transition metal-germanium interfaces," *Thin Solid Films*, vol. 42, no. 1, pp. 51–59, Apr. 1977, ISSN: 0040-6090. DOI: 10.1016/0040-6090(77)90077-3.

[182] G. Ottaviani, C. Canali, G. Ferrari, *et al.*, "Growth kinetics of $Pd_2Ge$ and PdGe on single-crystal and evaporated germanium," *Thin Solid Films*, vol. 47, no. 2, pp. 187–194, Dec. 1977, ISSN: 0040-6090. DOI: 10.1016/0040-6090(77)90359-5.

[183] G. Majni, G. Ferrari, R. Ferrari, *et al.*, "The solid phase epitaxial growth of germanium through palladium germanide layers," *Thin Solid Films*, vol. 44, no. 2, pp. 193–199, Jul. 1977, ISSN: 0040-6090. DOI: 10.1016/0040-6090(77)90454-0.

[184] G. Majni, G. Ottaviani, and A. Zani, "On the growth kinetics and structure of $Pd_2Ge$ and PdGe," *J. Non-Cryst. Solids*, vol. 29, no. 3, pp. 301–309, Sep. 1978, ISSN: 0022-3093. DOI: 10.1016/0022-3093(78)90151-5.

[185] G. Ottaviani, G. Majni, and C. Canali, "Dissociation of PtSi, NiSi and PdGe in presence of Pt, Ni and Pd films, respectively," *Appl. Phys.*, vol. 18, no. 3, pp. 285–289, Mar. 1979, ISSN: 1432-0630. DOI: 10.1007/bf00885516.

[186] Y. F. Hsieh and L. J. Chen, "Interfacial reactions of palladium thin films on Ge(111) and Ge(001)," *Thin Solid Films*, vol. 162, pp. 295–303, Aug. 1988, ISSN: 0040-6090. DOI: 10.1016/0040-6090(88)90218-0.

[187] Z. Chen, S. Zhang, S. Tan, and Z. Wu, "Annealing behavior and solid-state reactions of Pd–Ge alloy thin films," *Mater. Sci. Eng. A*, vol. 373, no. 1–2, pp. 21–25, May 2004, ISSN: 0921-5093. DOI: 10.1016/j.msea.2003.11.032.

[188] F. A. Geenen, W. Knaepen, K. De Keyser, *et al.*, "Formation and texture of palladium germanides studied by in situ X-ray diffraction and pole figure measurements," *Thin Solid Films*, vol. 551, pp. 86–91, Jan. 2014, ISSN: 0040-6090. DOI: 10.1016/j.tsf.2013.11.007.

[189] J. Perrin Toinin, K. Hoummada, M. Bertoglio, and A. Portavoce, "Origin of the first-phase selection during thin film reactive diffusion: Experimental and theoretical insights into the Pd-Ge system," *Scripta Mater.*, vol. 122, pp. 22–25, Sep. 2016, ISSN: 1359-6462. DOI: 10.1016/j.scriptamat.2016.05.008.

[190] A. Habanyama and C. M. Comrie, "Inter-Diffusion of Nickel and Palladium with Germanium," in *Intermetallic Compounds - Formation and Applications*. InTech, May 2018, ch. 7, p. 141, ISBN: 9781789231793. DOI: 10.5772/intechopen.73190.

[191] B. Krause, G. Abadias, D. Babonneau, *et al.*, "In Situ Study of the Interface-Mediated Solid-State Reactions during Growth and Postgrowth Annealing of Pd/a-Ge Bilayers," *ACS Appl. Mater. Interfaces*, vol. 15, no. 8, pp. 11 268–11 280, Mar. 2023, ISSN: 1944-8244. DOI: 10.1021/acsami.2c20600.

[192] A. Jain, S. P. Ong, G. Hautier, *et al.*, "Commentary: The Materials Project: A materials genome approach to accelerating materials innovation," *APL Mater.*, vol. 1, no. 1, p. 011 002, Jul. 2013, ISSN: 2166-532X. DOI: 10.1063/1.4812323.

[193] J. E. Saal, S. Kirklin, M. Aykol, B. Meredig, and C. Wolverton, "Materials design and discovery with high-throughput density functional theory: The Open Quantum Materials Database (OQMD)," *JOM*, vol. 65, no. 11, pp. 1501–1509, Sep. 2013, ISSN: 1543-1851. DOI: 10.1007/s11837-013-0755-4.

[194] S. Kirklin, J. E. Saal, B. Meredig, *et al.*, "The Open Quantum Materials Database (OQMD): Assessing the accuracy of DFT formation energies," *npj Comput. Mater.*, vol. 1, no. 1, p. 15 010, Dec. 2015, ISSN: 2057-3960. DOI: 10.1038/npjcompumats.2015.10.

[195] M. Tinkham, *Introduction to superconductivity*, 2nd ed. New York: McGraw-Hill, 1996, ISBN: 9780070648784.

[196] R. C. Bruno and B. B. Schwartz, "Magnetic field splitting of the density of states of thin superconductors," *Phys. Rev. B*, vol. 8, no. 7, pp. 3161–3178, Oct. 1973, ISSN: 0556-2805. DOI: 10.1103/physrevb.8.3161.

[197] D. P. Hampshire and H. Jones, "Flux flow in high-temperature type II superconductors governed by the activation of Frank-Read sources and the resultant motion of core dislocations," *J. Phys. C: Solid State Phys.*, vol. 21, no. 2, pp. 419–427, Jan. 1988, ISSN: 0022-3719. DOI: 10.1088/0022-3719/21/2/024.

[198] Q. Xie, S. Deng, M. Schaekers, *et al.*, "Germanium surface passivation and atomic layer deposition of high-k dielectrics - a tutorial review on Ge-based MOS capacitors," *Semicond. Sci. Tech.*, vol. 27, no. 7, p. 074 012, Jun. 2012, ISSN: 1361-6641. DOI: 10.1088/0268-1242/27/7/074012.

[199] C. A. Schneider, W. S. Rasband, and K. W. Eliceiri, "NIH image to ImageJ: 25 years of image analysis," *Nat. Methods*, vol. 9, no. 7, pp. 671–675, Jun. 2012, ISSN: 1548-7105. DOI: 10.1038/nmeth.2089.

[200] D. Nečas and P. Klapetek, "Gwyddion: An open-source software for SPM data analysis," *Open Phys.*, vol. 10, no. 1, pp. 181–188, Dec. 2011, ISSN: 2391-5471. DOI: 10.2478/s11534-011-0096-2. [Online]. Available: https://gwyddion.net/.

[201] M. Endres, A. Kononov, M. Stiefel, *et al.*, "Transparent Josephson junctions in higher-order topological insulator $WTe_2$ via Pd diffusion," *Phys. Rev. Mater.*, vol. 6, no. 8, p. l081201, Aug. 2022, ISSN: 2475-9953. DOI: 10.1103/physrevmaterials.6.l081201.

[202] K. D. Usadel, "Generalized diffusion equation for superconducting alloys," *Phys. Rev. Lett.*, vol. 25, no. 8, pp. 507–509, Aug. 1970, ISSN: 0031-9007. DOI: 10.1103/physrevlett.25.507.

[203] I. O. Kulik and A. N. Omel'yanchuk, "Contribution to the microscopic theory of the Josephson effect in superconducting bridges," *JETP Lett.*, vol. 21, no. 4, pp. 96–97, Feb. 1975, ISSN: 0021-3640. [Online]. Available: http://jetpletters.ru/ps/0/article_22289.shtml.

[204] I. O. Kulik and A. N. Omel'yanchuk, "Josephson effect in superconducting bridges: Microscopic theory," *Sov. J. Low Temp. Phys.*, vol. 4, no. 3, pp. 142–149, Mar. 1978, ISSN: 0360-0335. DOI: 10.1063/10.0029644.

[205] K. K. Likharev, "Superconducting weak links," *Rev. Mod. Phys.*, vol. 51, pp. 101–159, 1 Jan. 1979. DOI: 10.1103/RevModPhys.51.101.

[206] D. A. Ivanov, R. von Roten, and G. Blatter, "Minigap in a long disordered SNS junction: Analytical results," *Phys. Rev. B*, vol. 66, no. 5, p. 052 507, Aug. 2002, ISSN: 1095-3795. DOI: 10.1103/physrevb.66.052507.

[207] P. Dubos, H. Courtois, B. Pannetier, F. K. Wilhelm, A. D. Zaikin, and G. Schön, "Josephson critical current in a long mesoscopic S-N-S junction," *Phys. Rev. B*, vol. 63, no. 6, p. 064 502, Jan. 2001, ISSN: 1095-3795. DOI: 10.1103/physrevb.63.064502.

[208] P. Dubos, H. Courtois, O. Buisson, and B. Pannetier, "Coherent low-energy charge transport in a diffusive S-N-S junction," *Phys. Rev. Lett.*, vol. 87, no. 20, p. 206 801, Oct. 2001, ISSN: 1079-7114. DOI: 10.1103/physrevlett.87.206801.

[209] C. Li, S. Guéron, A. Chepelianskii, and H. Bouchiat, "Full range of proximity effect probed with superconductor/graphene/superconductor junctions," *Phys. Rev. B*, vol. 94, no. 11, p. 115 405, Sep. 2016, ISSN: 2469-9969. DOI: 10.1103/physrevb.94.115405.

[210] C. T. Ke, I. V. Borzenets, A. W. Draelos, *et al.*, "Critical current scaling in long diffusive graphene-based Josephson junctions," *Nano Lett.*, vol. 16, no. 8, pp. 4788–4791, Jul. 2016, ISSN: 1530-6992. DOI: 10.1021/acs.nanolett.6b00738.

[211] T. Claeson, J. Ivarsson, and S. E. Rasmussen, "Superconductivity of $Nb_5Ge_3$," *J. Appl. Phys.*, vol. 48, no. 9, pp. 3998–3999, Sep. 1977, ISSN: 1089-7550. DOI: 10.1063/1.324239.

[212] C. Kopas, S. Zhang, J. Gonzales, *et al.*, *Ge thin-films with tantalum diffusion-barriers for use in Nb-based superconductor technology*, 2021. arXiv: 2104.12580 [cond-mat.supr-con].

[213] B. Langa, D. Sapkota, I. Lainez, *et al.*, "Solid-state reactions at niobium–germanium interfaces in hybrid quantum electronics," *AIP Adv.*, vol. 14, no. 9, p. 095 311, Sep. 2024, ISSN: 2158-3226. DOI: 10.1063/5.0221366.

[214] M. Zhang, W. Yu, W. H. Wang, and W. K. Wang, "Interdiffusion in compositionally modulated amorphous Nb/Si multilayers," *Thin Solid Films*, vol. 287, no. 1–2, pp. 293–296, Oct. 1996, ISSN: 0040-6090. DOI: 10.1016/s0040-6090(96)08765-2.

[215] J. O. Willis and R. M. Waterstrat, "Superconductivity in $Nb_5Si_3$," *J. Appl. Phys.*, vol. 50, no. 4, pp. 2863–2866, Apr. 1979, ISSN: 1089-7550. DOI: 10.1063/1.326202.

[216] S. Lee, T. N. Walter, S. E. Mohney, and T. N. Jackson, "High-temperature-capable ALD-based inorganic lift-off process," *Mat. Sci. Semicon. Proc.*, vol. 130, p. 105 809, Aug. 2021, ISSN: 1369-8001. DOI: 10.1016/j.mssp.2021.105809.

[217] S. Li, X. Liu, V. Anand, and B. Lv, "Superconductivity and phase diagram in a transition metal doped $Zr_5Ge_3$ compound," *Supercond. Sci. Technol.*, vol. 31, no. 8, p. 085 001, Jun. 2018, ISSN: 1361-6668. DOI: 10.1088/1361-6668/aac6a1.

[218] B. T. Matthias, E. Corenzwit, and W. H. Zachariasen, "Superconductivity and ferromagnetism in isomorphous compounds," *Phys. Rev.*, vol. 112, no. 1, pp. 89–89, Oct. 1958, ISSN: 0031-899X. DOI: 10.1103/physrev.112.89.

[219] M. S. Wei, H. H. Sung, and W. H. Lee, "Superconductivity in $YGe_3$," *Physica C*, vol. 424, no. 1-2, pp. 25–28, Aug. 2005, ISSN: 0921-4534. DOI: 10.1016/j.physc.2005.04.021.

[220] J. Wu, C. Hua, B. Liu, *et al.*, "Doping-induced superconductivity in the topological semimetal $Mo_5Si_3$," *Chem. Mater.*, vol. 32, no. 20, pp. 8930–8937, Sep. 2020, ISSN: 1520-5002. DOI: 10.1021/acs.chemmater.0c02831.

[221] B.-B. Ruan, J.-N. Sun, M.-H. Zhou, *et al.*, "Superconductivity induced by site-selective arsenic doping in $Mo_5Si_3$," *Inorg. Chem.*, vol. 61, no. 27, pp. 10 267–10 271, Jun. 2022, ISSN: 1520-510X. DOI: 10.1021/acs.inorgchem.2c01647.

[222] J.-U. Bae, T.-Y. Lin, Y. Yoon, *et al.*, "Characterization of nanomagnet fringing fields in hybrid semiconductor/ferromagnetic devices," *IEEE Trans. Magn.*, vol. 44, no. 12, pp. 4706–4710, Dec. 2008, ISSN: 0018-9464. DOI: 10.1109/tmag.2008.2002924.

[223] T.-Y. Lin, K.-M. Lim, A. M. Andrews, G. Strasser, and J. P. Bird, "Nonspin related giant magnetoresistance $\leq 600\%$ in hybrid field-effect transistors with ferromagnetic gates," *Appl. Phys. Lett.*, vol. 97, no. 6, p. 063 108, Aug. 2010, ISSN: 1077-3118. DOI: 10.1063/1.3477962.

[224] A. Bordoloi, V. Zannier, L. Sorba, C. Schönenberger, and A. Baumgartner, "A double quantum dot spin valve," *Commun. Phys.*, vol. 3, no. 1, p. 135, Aug. 2020, ISSN: 2399-3650. DOI: 10.1038/s42005-020-00405-2.

[225] W. D. Chen, X. L. Xie, Y. D. Cui, C. H. Chen, and C. C. Hsu, "Microstructure studies of PdGe/Ge ohmic contacts to n-type GaAs formed by rapid thermal annealing," *Appl. Surf. Sci.*, vol. 100-101, pp. 530–533, Jul. 1996, ISSN: 0169-4332. DOI: 10.1016/0169-4332(96)00334-0.

[226] E. D. Marshall, B. Zhang, L. C. Wang, *et al.*, "Nonalloyed ohmic contacts to n-GaAs by solid-phase epitaxy of Ge," *J. Appl. Phys.*, vol. 62, no. 3, pp. 942–947, Aug. 1987, ISSN: 1089-7550. DOI: 10.1063/1.339705.

# A. LIST OF WAFERS

Table A.1 shows the list of all strained Ge QW wafers grown on $p$-Si substrates. The wafer structure is as shown in Fig. 2.1. Table A.2 shows the list of all undoped strained Ge QW wafers grown on $i$-Si substrates.

**Table A.1.** List of Ge/SiGe quantum well (QW) wafers grown on $p$-Si.

| Wafer | SiGe content | Buffer | B doping | | Spacer | QW | Cap | |
|---|---|---|---|---|---|---|---|---|
| | | nm | $10^{17}$cm$^{-3}$ | nm | nm | nm | SiGe (nm) | Ge (nm) |
| 19-218 | $Si_{0.20}Ge_{0.80}$ | 4500 | - | - | 100 | 15 | 200 | 2 |
| 19-219 | $Si_{0.20}Ge_{0.80}$ | 4500 | 5 | 5 | 100 | 15 | 200 | 2 |
| 19-220 | $Si_{0.20}Ge_{0.80}$ | 4500 | 10 | 5 | 100 | 15 | 200 | 2 |
| 22-159 | $Si_{0.15}Ge_{0.85}$ | 2850 | 5 | 5 | 100 | 15 | 200 | 2 |
| 22-160 | $Si_{0.15}Ge_{0.85}$ | 2850 | 5 | 5 | 100 | 15 | 100 | 2 |
| 22-211 | $Si_{0.15}Ge_{0.85}$ | 2850 | 5 | 5 | 50 | 15 | 20 | 2 |
| 22-212 | $Si_{0.15}Ge_{0.85}$ | 2850 | 5 | 5 | 50 | 15 | 100 | 2 |
| 22-213 | $Si_{0.15}Ge_{0.85}$ | 2850 | 5 | 5 | 50 | 15 | 200 | 2 |
| 22-244 | $Si_{0.15}Ge_{0.85}$ | 2850 | 5 | 5 | 100 | 15 | 200 | 2 |
| 22-246 | $Si_{0.15}Ge_{0.85}$ | 2850 | 5 | 5 | 100 | 15 | 200 | 2 |
| 24-141 | $Si_{0.15}Ge_{0.85}$ | 3000 | 10 | 5 | 50 | 15 | 7 | - |
| 24-142 | $Si_{0.15}Ge_{0.85}$ | 3000 | 10 | 5 | 50 | 15 | 5 | - |

**Table A.2.** List of Ge/SiGe quantum well (QW) wafers grown on $i$-Si.

| Wafer | SiGe content | Ge buffer | SiGe buffer | Ge QW | SiGe cap |
|---|---|---|---|---|---|
| | | nm | nm | nm | nm |
| 24-231 | $Si_{0.17}Ge_{0.83}$ | 1000 | 2500 | 15 | 7 |
| 24-232 | $Si_{0.17}Ge_{0.83}$ | 1000 | 2500 | 15 | 10 |
| 24-233 | $Si_{0.17}Ge_{0.83}$ | 1000 | 2500 | 15 | 5 |

# B. FABRICATION PROCESS

In this appendix, we introduce the techniques for sample fabrication and provide an example of the fabrication recipe for gated Ge samples.

## B.1 Lithography

The fabrication starts with cutting the wafer into small pieces, usually ranging from 3 mm × 3 mm to 1 cm × 1 cm, depending on the lithography method and pattern design. It is followed by the standard organic cleaning procedure. The sample is immersed in toluene, acetone, and isopropyl alcohol (IPA) each for 5 min in a sequence, together with ultrasonication at the same time. Thereafter, the sample is rinsed with IPA and blown dry with a $N_2$ gun. The sample is then ready for spin coating and lithography to define sample patterns. Usually, several patterns are defined on each piece of sample, which is cut into individuals at the end of the fabrication process.

### B.1.1 Optical Lithography

Optical lithography is used for patterns with feature sizes of more than 1 $\mu$m. We usually use AZ1518 optical resist for optical lithography at BNC, Purdue University. The sample is spin coated with AZ1518 at 3500 rpm for 60 s, followed by 120 s soft bake at 110 °C.

The optical exposure is done using 405 nm UV light with a Suss MJB3 UV400 mask aligner for patterns that we do have their masks, or a Heidelberg MLA150 maskless aligner for other patterns. For the MJB3 mask aligner, the sample is usually exposed for 15 s at 14 mW/cm$^2$ UV power. For small features $\sim 1\,\mu$m, an exposure for $\approx 5.2$ s at 20 mW/cm$^2$ UV power has been tested to work reproducibly. For the Heidelberg maskless aligner, the dosage depends on substrate material and pattern feature size.

After exposure, the sample is developed with MF-26A developer for 20 s + 20 s in two beakers, followed by a 120 s DI water rinse and $N_2$ blow dry. The development is done in two steps for less resist residue. The sample should always be covered with liquid when

transferring between two beakers and until properly rinsed with DI water. Otherwise, some unremovable residue might be left on the sample.

### B.1.2 E-beam Lithography

E-beam lithography is used to write patterns with feature sizes less than 1 nm. Due to the following dry etching procedure, we use relatively thick e-beam resists, including PMMA 950 C4 and AR-P 6200.13. Both resists are about 400 nm thick after $\geqslant 400$ rpm spin coating and soft baking. AR-P 6200.13 resist is chosen for deeper dry etching because of its higher dry etching resistance. PMMA 950 C4 is spin coated at 6000 rpm for 60 s and soft baked at 180 °C for 90 s. AR-P 6200.13 is spin coated at 4000 rpm, or 2500 rpm to get slightly thicker resist ($\sim 500$ nm) against etching, for 60 s and soft baked at 180 °C for 180 s, or 150 °C for 60 s as suggested by the manufacturer. No significant difference in dosage is found between these two soft baking temperatures. An optional 90 °C overnight oven baking can be done for better adhesion and slightly better resolution.

The e-beam writing is performed with 25 kV acceleration voltage using a Zeiss EVO 40 scanning electron microscope (SEM) in our lab or a Raith eLine e-beam writer at BNC. The Zeiss EVO 40 system is used to write patterns with feature sizes down to 150 nm. Finer features have to be defined by the Raith eLine system. The exact dosage for each resist depends on the spin speed and developer, etc. We usually use MIBK : IPA = 1 : 3 or DI : IPA = 1 : 3 as the developer. If we spin coat as described above, the typical dose for PMMA 950 C4 is $\sim 240\,\mu\text{C/cm}^2$ with MIBK : IPA = 1 : 3 developer and $\sim 110\,\mu\text{C/cm}^2$ with DI : IPA = 1 : 3. The typical dose for AR-P 6200.13 is $\sim 270\,\mu\text{C/cm}^2$ with MIBK : IPA = 1 : 3 developer.

The sample is usually developed for 60 s + 30 s in two beakers of chosen developer, followed by 30 s IPA rinse and $N_2$ blow-dry. An optional post-development hard bake can be done by 1 min < 125 °C hot plate baking, which can provide slightly enhanced dry etching resistance.

## B.2 Dry Etching

Before ICP-RIE dry etching, the sample is treated with $O_2$ plasma ashing using the Branson Asher or Tergeo plasma cleaner at BNC to remove resist residue in the exposed area.

The plasma ashing is done at $1 \sim 2$ mTorr with 100 W RF power for 1 min, which typically removes a few nanometers of resist. This ensures precise etch depth and less rough etched surface in the next ICP-RIE dry etching step.

We use the Panasonic E620 or Plasma Therm Apex ICP-RIE etcher at BNC for dry etching. Originally, two recipes were used for mesa and contact etching separately. The old mesa etching recipe is: gas flow $CF_4/Ar = 70/10$ sccm, pressure $P = 6$ Pa, RF power ICP/bias = 100/20 W, and contact etching is done with $SF_6/O_2 = 15/15$ sccm, 1.35 Pa, ICP/bias = 100/20 W in early experiments. However, as we see in Fig. 2.10, ICP/bias = 100/20 W power setting results in a large overhang for both gas combinations, which can result in disconnection between channel and contact. Moreover, $CF_4/Ar$ etching is isotropic and creates a nearly vertical top edge of the mesa. For thin contact $\sim 10$ nm, this may probably cause disconnection of contact over the mesa edge. Therefore, we later move to $SF_6/O_2$ etching with higher RF bias power ICP/bias = 50/50 W at 1.35 Pa that results in no overhang for contact etching, and we control the edge profile with $SF_6/O_2$ ratio. We use $SF_6/O_2 = 20/10$ sccm for small sidewall angles and $SF_6/O_2 = 15/15$ sccm for steep edges.

However, the high RF bias power also results in a much higher etching rate of the resist. $\sim 400$ nm PMMA 950 C4 already barely survives after $\sim 230$ nm SiGe dry etching in the old $SF_6/O_2$ recipe, making it not very suitable for fine contact features with dry etching. AR-P 6200.13 is about twice as resistant as PMMA 950 C4 in the same recipe, but as RF power is changed to ICP/bias = 50/50 W, AR-P 6200.13 is almost consumed after $\sim 215$ nm $SF_6/O_2$ dry etching to the Ge QW. This means higher bias power deteriorates the selective ratio of AR-P 6200.13 to SiGe by about half.

Therefore, we now choose $SF_6/O_2 = 20/10$ sccm, 1.35 Pa, ICP/bias = 100/20 W for $> 330$ nm deep mesa etching with shallow edge profile, and $SF_6/O_2 = 15/15$ sccm, 1.35 Pa, ICP/bias = 50/50 W for $\sim 230$ nm steep contact etching. $SF_6/O_2 = 20/10$ sccm can also be used for contact etching if the metal deposition system is not equipped with a substrate rotation function. To get slightly more resist left for easier contact lift-off without creating overhang, a short etching with ICP/bias = 100/20 W can be done before ICP/bias = 50/50 W. An intermediate power setting can be tuned to balance the overhang and selective ratio, which requires more work.

A gentle wet etching with $(HF : H_2O_2 : CH_3COOH = 1 : 2 : 3) : DI = 1 : 3$ [150] is optional to reduce damage on the surface after dry etching. Slower and more controllable wet etching with warm DI water or dilute $H_2O_2$ is also a viable option.

Some preliminary calibration has been done on $AlO_x$, as a hard mask of SiGe. Using $BCl_3$ etching, the selective ratio is about 1:1. And the selective ratio in the $SF_6/O_2$ recipe is on the order of 1:100. It is suggested to over-etch $AlO_x$ with $BCl_3$ by $10 \sim 20\%$ to ensure removal of the hard mask in the exposed area. The remaining resist after hard mask etch can be kept during the following dry etching process as an extra mask.

### B.3 Contact Deposition and Annealing

Removal of oxides on the surface of SiGe is crucial to reduce the contact barrier. To thoroughly remove all the thin native oxides or oxides after $SF_6/O_2$ dry etching on the surface of (Si)Ge, we clean the sample with $HCl : DI = 1 : 6$ dipping for 15 s, followed by $HF : DI = 1 : 10$ dipping for 10 s, DI water rinse for 10 s, and $N_2$ blow dry. The sample should be quickly loaded to the contact growth chamber or load lock, and pumping should start within 10 min after acid cleaning.

In some early experiments by Dr. Ying Wang, Al contacts are thermally evaporated in a sputtering chamber in our lab at 45° tilt angle, followed by Nb/NbN sputtering for superconducting contacts. Later, Al, Pd, Pt, and Rh contacts are e-beam evaporated at high vacuum using our AJA hybrid sputtering and e-beam evaporation system, which is equipped with substrate tilting and rotation functions. Nb(N), NbTi(N), and MoRe are sputtered also in our AJA system. Ir is sputtered by Dr. Michael Lilly using the Kurt J. Lesker PVD-75 system at the Center for Integrated Nanotechnologies (CINT), Sandia National Laboratories.

When using our AJA system for contact deposition, we do a gentle Ar ion milling before deposition. This step is used to remove a few Å of oxides or contamination that can possibly form after acid cleaning or reloading of the sample after some treatment in the atmosphere. The Ar ion milling is done in an $< 0.5$ mTorr Ar atmosphere at an acceleration voltage slightly above the threshold for certain materials, preferably at a $20 \sim 30°$ tilt angle with proper substrate rotation to avoid redeposition of etched material.

For Al diffusion contact to Ge, the annealing can be done in a following $\sim$ 3h 300 °C ALD growth at the same time. A shorter annealing in $N_2/H_2$ or $Ar/H_2$ at 350 °C with our home-built annealing station can be used for more controllable diffusion in (Si)Ge. Generally, to diffuse Al to the 200 nm deep Ge QW, $\sim$ 30 min annealing is sufficient to create good ohmic contact without too much lateral diffusion.

For Pd and Pt, 10 nm or even slightly thinner contact with side deposition is preferred, in preparation for the Nb(N), NbTi(N), or MoRe layer on top after annealing, to better proximitize larger gaps from the top layer through the Pd(/Pt)Ge layer to Ge QW. Self-aligned double-layer contact can be fabricated with the help of a $AlO_x$ hard mask sputtered by a PVD sputtering system at BNC, which can handle the high annealing temperature. The top metal layer can be lifted off in diluted HCl after evaporation. If the top layer is MoRe, soaking time in HCl should be limited due to the solubility of MoRe in water. But to test whether a second deposition after annealing can improve the induced gap, a second e-beam lithography with alignment can be used first. For Ir, 10 nm thick contact by itself is probably good enough, considering annealing time, $T_c$, and $B_c$. But thinner Ir can be tried to further reduce annealing time, as Ir film continuity is confirmed with $\sim$ 3 nm film. If the thin contact becomes disconnected at the mesa edge after annealing, patching with thick metal (e.g., Al or Nb) can be done across the mesa edge to ensure contact continuity. Annealing of Pd, Pt, Ir, and also Nb(N), NbTi(N), and MoRe is performed in an Ar atmosphere without hydrogen, due to potential hydrogen absorption in these metals. However, we confirmed that annealing of Ir/SiGe in $N_2/H_2$ does not have a significant effect on the $T_c$ of IrSiGe.

Samples patterned with PMMA 950 C4 or AR-P 6200.13 can be lifted off by soaking the sample in 60 °C acetone for a few hours after evaporation. If the metal flakes do not remove easily, some gentle ultrasonication or gently scrubbing with a cleanroom swab can help perform a cleaner lift-off. 80 °C remover PG is another better choice to leave less resist residue. In addition, AR-P 6200.13 can be removed much faster in remover PG than in acetone.

## B.4 Gate Fabrication

Before ALD growth on (Si)Ge, it is important to properly remove the native oxide on the surface to reduce interface trapped charge density between Ge and the ALD oxide layer. The acid cleaning is the same as the process before contact deposition, i.e., $HCl : DI = 1 : 6$ dipping for 15 s, followed by $HF : DI = 1 : 10$ dipping for 10 s, DI water rinse for 10 s, and $N_2$ blow dry. The sample should be quickly loaded to the ALD chamber or load lock, and pumping should start within 10 min after acid cleaning. Since MoRe can be slowly dissolved in water or some aqueous solutions, treatment of samples with MoRe contacts has to be carefully controlled.

Our oxide for the electrostatic gate is grown with the Cambridge Nanotech Fiji ALD system at BNC. $AlO_x$ is the most common oxide used for our samples. $HfO_x$ with a higher dielectric constant is also available if we want to reduce the oxide thickness for the same gate capacitance. Low growth temperature down to 110 °C is available, but the resulting interface trapped charge density is high, and the growth time is long. From our experiments, oxides grown on conducting Ge QW wafers below 300 °C result in an insulating channel at zero gate voltage. Therefore, $\sim 30$ nm of $AlO_x$ is usually grown at 300 °C in our gated devices. For oxides grown at 200 °C, 10 min 350 °C post-annealing in Ar or forming gas can also help reduce the interface trapped charge density.

After ALD oxide growth, the metal gate pattern is defined using optical or e-beam lithography as described above. If optical lithography is used, we can soak the sample in chlorobenzene for 10 min before development to create an undercut, which can make lift-off easier. The sample is directly loaded for metal deposition after development. Unlike contact deposition, there is no acid cleaning or $O_2$ cleaning before deposition, but we can still do a very gentle Ar ion milling to clean the surface. Normally, we deposit thick ($100 \sim 200$ nm) Al as the gate. In practice, we can also use Ti/Au or Pd as the gate, but they are pricier. The lift-off process for the gate is the same as described in contact deposition.

## B.5 Sample Packaging

After all the fabrication processes, a sample with multiple patterns is cut into individual pieces for separate measurements if needed. Then the sample is glued on chip carriers with GE varnish. Since our experiments involve strong magnetic fields, a chip carrier is better chosen without magnetic metals right beneath the sample mounting area. Otherwise, the magnetic metals can heat the sample significantly when sweeping a strong magnetic field across zero in dilution refrigerator measurements. This can kill many physical effects we are interested in.

The sample glued onto the chip carrier is then wire bonded with fine Al wire, using a West Bond 7476D wire bonder in Prof. Yong Chen's lab. An ultrasonic power of about $\sim 220\,\mathrm{mW}$ is typical for Al bonding pads, 250 mW for Pd/Pt, and $\sim 300\,\mathrm{mW}$ for MoRe/NbTi(N)/Ir. With these high powers, the contact pads below the thin gate dielectric can be easily contacted by physically punching through the oxide. When wiring a gated sample, we should first carefully ground ourselves and all pins on the sample carrier, then connect all pins with wire, finish bonding all the electric contacts, and at last bond the gate pad. The shorting wires can be removed after the sample is loaded and properly grounded for measurement. These procedures avoid high-voltage shock on the gate and ensure a high yield of working gates without burning. Typically, the leakage current of our gated devices is below 1 pA up to $\gtrsim 30\,\mathrm{V}$.

## B.6 Example of Fabrication Recipe

We provide an example of the fabrication recipe for a Ge QW 22-213 gated device using Pt/Nb(N) superconducting contacts with two-step e-beam lithography to show the general procedures of sample making.

1. Mesa lithography

   (a) Sample cleaning: Cut sample to desired size, ultrasonicate in toluene 5 min, acetone 5 min, IPA 5 min, rinse with IPA, and blow dry with a $N_2$ gun.

   (b) Spin coating: AR-P 6200.13 2500 rpm 60 s, soft bake 180 s at 180 °C.

(c) E-beam lithography: 25 kV acceleration, $\sim 270\,\mu C/cm^2$ dose, and larger beam current to reduce writing time.

(d) Developing: MIBK : IPA = 1 : 3 60 s + 30 s, IPA rinse 30 s, $N_2$ blow-dry.

2. Mesa dry etching

(a) Resist residue removal: $O_2$ plasma ashing in Ar and $O_2$ 1 $\sim$ 2 Torr 100 W 60 s.

(b) Dry etching: Bond sample to carrier wafer with Crystalbond 555 on hotplate at 70 $\sim$ 90 °C for $>$ 2 min for uniform adhesion; (Panasonic etcher) $SF_6/O_2$ = 20/10 sccm, 1.35 Pa, ICP/bias = 100/20 W, 9 min for $\sim$ 300 nm etch depth.

(c) Sample de-bonding: De-bond sample from carrier wafer at 70 $\sim$ 90 °C and scrub on hot wafer to remove most of the Crystalbond, rinse with DI water to remove the Crystalbond residue.

(d) Resist removal: Remover PG 80 °C $\sim$ 30 min.

3. Contact lithography, layer 1

(a) Sample cleaning: Acetone 5 min, IPA 5 min, IPA rinse, $N_2$ blow dry.

(b) Spin coating: AR-P 6200.13 2500 rpm 60 s, soft bake 180 °C 180 s.

(c) E-beam lithography: 25 kV acceleration, $\sim 270\,\mu C/cm^2$ dose, smaller beam current for fine features.

(d) Developing: MIBK : IPA = 1 : 3 60 s + 30 s, IPA rinse 30 s, $N_2$ blow dry.

4. Contact dry etching, layer 1

(a) Resist residue removal: $O_2$ plasma ashing 100 W 60 s.

(b) Dry etching: Bond with Crystalbond 555 70 $\sim$ 90 °C $>$ 2 min; (Panasonic) $SF_6/O_2$ = 15/15 sccm, 1.35 Pa, ICP/bias = 50/50 W, 6 min for $\sim$ 215 nm depth.

(c) Sample de-bonding: De-bond at 70 $\sim$ 90 °C, rinse with DI water.

5. Contact deposition and annealing, layer 1

(a) Acid cleaning: HCl : DI = 1 : 6 dip 15 s, HF : DI = 1 : 10 dip 10 s, DI water rinse 10 s, $N_2$ blow dry, load sample, and start pumping within 10 min.

(b) Ion milling: (AJA system) Ar 4 sccm $\sim$ 0.2 mTorr, 200 V beam voltage, 200 V acceleration voltage, 25° tilt, 20 rpm substrate rotation, 15 s.

(c) Metal deposition: Pt e-beam evaporation with $< 1.0 \times 10^{-8}$ Torr base pressure, 45° tilt, 1.5 Å/s growth rate, 10 nm on each side of the contact.

(d) Lift-off: Remover PG 80 °C $\sim$ 60 min, gentle ultrasonication or swab scrub if lift-off is incomplete, acetone rinse, $N_2$ blow dry.

(e) Contact annealing: Ar atmosphere, 350 °C 5 min with 1°C/s ramping.

6. Contact lithography, layer 2

(a) Sample cleaning: Acetone 5 min, IPA 5 min, IPA rinse, $N_2$ blow dry.

(b) Spin coating: AR-P 6200.13 2500 rpm 60 s, soft bake 180 °C 180 s (or PMMA).

(c) E-beam lithography: 25 kV acceleration, $\sim 270\,\mu C/cm^2$ dose, with alignment.

(d) Developing: MIBK : IPA = 1 : 3 60 s + 30 s, IPA rinse 30 s, $N_2$ blow-dry.

7. Contact deposition, layer 2

(a) Ion milling: (AJA) Ar 4 sccm $\sim$ 0.2 mTorr, 200 V beam, 200 V acceleration, 25° tilt, 20 rpm rotation, 15 s.

(b) Metal deposition: Nb DC sputtering 3" target distance, Ar 10 sccm, 2 mTorr, 200 W ($\sim$ 4.2 Å/s), 45° tilt, 5 nm each side; NbN sputtering 3" distance, Ar 10 sccm, $N_2$ 2 sccm, 3 mTorr, 200 W, 45° tilt, 10 nm each side.

(c) Lift-off: Remover PG 80 °C $\sim$ 60 min, acetone rinse, $N_2$ blow-dry.

8. ALD oxide growth

(a) Acid cleaning: HCl : DI = 1 : 6 dip 15 s, HF : DI = 1 : 10 dip 10 s, DI water rinse 10 s, $N_2$ blow dry, load sample, and start pumping within 10 min.

(b) ALD growth: $AlO_x$ (precursor: trimethylaluminum and water) 300 °C $\sim$ 30 nm (300 cycles).

9. Gate lithography

   (a) Spin coating: AR-P 6200.13 2500 rpm 60 s, soft bake 180 °C 180 s (or PMMA).

   (b) E-beam lithography: 25 kV acceleration, $\sim 270\,\mu C/cm^2$ dose, with alignment.

   (c) Developing: MIBK : IPA = 1 : 3 60 s + 30 s, IPA rinse 30 s, $N_2$ blow-dry.

10. Gate deposition

    (a) Ion milling: (AJA) Ar 4 sccm $\sim$ 0.2 mTorr, 200 V beam voltage, 200 V acceleration voltage, 25° tilt, 20 rpm substrate rotation, 15 s.

    (b) Metal deposition: Al e-beam evaporation, 2 Å/s, 100 nm vertical deposition.

    (c) Lift-off: Remover PG 80 °C $\sim$ 60 min, acetone rinse, $N_2$ blow-dry.

11. Sample Packaging

    (a) Sample mounting: Cut sample into individual patterns, glue on chip carrier with GE varnish, and let dry for $\sim$ 1 h.

    (b) Wire bonding: Bond with Al wire, short all pins together for protection, $\sim$ 300 mW for PtSiGe/Nb(N) contact pad, $\sim$ 220 mW for Al gate pad.

# C. LIST OF PUBLICATIONS

## C.1 Publications Related to This Thesis

1. **Hao Li**, Zhongxia Shang, Michael P. Lilly, Maksym Myronov, and Leonid P. Rokhinson, "Characterization of superconducting germanide and germanosilicide films of Pd, Pt, Rh, and Ir formed by solid-phase epitaxy," *APL Mater.*, vol. 14, no. 3, p. 031101, Mar. 2026, ISSN: 2166-532X. DOI: 10.1063/5.0301077, preprint available at arXiv: 2509.14173.

2. Leonid Rokhinson and **Hao Li**. "Iridium-germanium superconducting electrodes." U.S. Provisional Patent Application No. 64/008,556, filed March 17, 2026.

## C.2 Presentations

1. **Hao Li**, Zhongxia Shang, Michael P. Lilly, Maksym Myronov, and Leonid P. Rokhinson. "Development of high-$T_c$ high-$B_c$ contacts to Ge quantum wells." Oral presentation at the *Joint March Meeting and April Meeting: APS Global Physics Summit 2025*, Anaheim, CA, USA, Mar 2025. Abstract MAR-L24.05.